POLITECNICO DI MILANO

School of Industrial and Information Engineering

Master of Science in Materials Engineering and Nanotechnology

SCANNING TUNNELING MICROSCOPY AND RAMAN SPECTROSCOPY OF CARBON ATOM WIRES SYNTHESIZED ON AU (111)

Supervisor: Prof. Carlo S. Casari
Co-supervisor: Dr. Francesco Tumino

Candidate:
Riccardo Improta
Mat. 880564

Academic Year 2017-2018

Sommario

Negli ultimi trent'anni, le nanostrutture a base di carbonio hanno ricoperto un ruolo fondamentale nella ricerca e sviluppo di nuovi materiali per applicazioni in campo ingegneristico, a tal punto che A. Hirsh ha definito il periodo corrente come "l'era degli allotropi del carbonio". A partire dalla scoperta del fullerene, avvenuta nel 1985, molte altre nanostrutture in carbonio, quali i nanotubi e il grafene, hanno attirato l'attenzione degli scienziati a causa delle loro proprietà eccezionali. In tal contesto, la forma allotropica del carbonio, composta da catene lineari a ibridazione sp, è emersa come un potenziale leader, mostrando caratteristiche meccaniche, ottiche e di conduzione elettrica e termica superiori alla norma. Tuttavia, diversi problemi sono stati riscontrati nella fase di sintesi e stabilizzazione di tali catene, le quali hanno mostrato una tendenza alla riorganizzazione in forme più stabili, a ibridazione sp^2, attraverso reazioni di reticolazione molecolare. Il presente elaborato di tesi si colloca in questo preciso ambito e riporta un'analisi sperimentale di nanofili a base di carbonio su Au (111) tramite microscopia a effetto tunnel (STM, Scanning Tunneling Microscopy), spettroscopia a effetto tunnel (STS, Scanning Tunneling Spectroscopy) e spettroscopia Raman. I fili sono stati sintetizzati mediante reazioni di accoppiamento su Au (111) di bromo-precursori, evaporati termicamente in condizioni di ultra alto vuoto (UHV, Ultra-High Vacuum). Diversi cicli di ricottura sono stati eseguiti sul campione, per consentire un'indagine, tramite l'analisi di immagini STM a larga e piccola scala, degli effetti dell'incremento termico sulle proprietà morfologiche e strutturali dei nanofili. Inoltre, uno studio degli spettri STS e delle mappe di conduttività differenziale ha permesso una caratterizzazione delle proprietà elettroniche dei nanofili e ha messo in luce variazioni peculiari nella conduttività superficiale. L'analisi di spettri Raman acquisiti sui campioni ricotti e il confronto di questi con modelli computazionali hanno fornito poi informazioni rilevanti circa la struttura vibrazionale di tali strutture. Infine, misure preliminari sulla composizione chimica del campione sono state condotte mediante spettroscopia Auger. Il ruolo attivo svolto dal substrato di Au (111) nel processo di formazione delle catene è emerso come caratteristica comune nella maggior parte delle indagini condotte sul campione. I risultati ottenuti in questo elaborato di tesi hanno portato a una conoscenza più dettagliata delle proprietà morfologiche, strutturali, elettroniche e vibrazionali dei sistemi di carbonio lineari e vengono intese come misurazioni preliminari a supporto di futuri studi di caratterizzazione sperimentale.

Contents

Introduction

In the last decades, nanostructures have attracted the attention of science for their excellent performances and have thus been considered as possible novel materials in engineering fields like electronics, mechanics and energy. Indeed, nano-sized objects have exhibited properties far superior then their bulk counterpart, due to effects related to extremely low dimensionalities. In this context, carbon-based nanomaterials have emerged in a wide variety of forms, which derive from the different ways that carbon can arrange its valence electrons. Among the others, it is worth mentioning carbon nanotubes and graphene, whose recently-predicted outstanding properties have nurtured the interest of researchers over new carbon nanostructures.

In particular, the existence of a third allotropic form of carbon, based on sp-hybridized species, have been the subject of a debate by the chemical and physic community, which is still open. In fact, besides graphite and diamond, which represent the solid-state systems of the sp^2- and sp^3-carbon hybrid states, a crystalline structure formed by sp-carbon chains, the carbyne, has not been observed yet. However, a large number of articles, concerning the production, the characterization and computational simulations of linear chains formed by sp-hybridized carbon atoms, can be found nowadays in literature. These linear structures are considered the ultimate one-dimensional carbon systems and they will be the central topic of this thesis work.

By means of computer calculations, it has been possible to predict some brilliant properties of these sp-carbon systems, which have turned out to be very competitive for a leading role in material science and in nanotechnology. For instance, they have displayed an exceptional mechanical strength and very high electron and thermal conductivity. Moreover, the tunability of functional properties, such as the band gap, by controlling the termination and the length of the wire, have opened new opportunities towards the development of 'all-carbon' structures for future applications [1,2,3].

As far as the fabrication of sp-carbon chains is concerned, different synthesis techniques, based on both physical and chemical processes, have been developed and a bottom-up approach has been generally preferred. Furthermore, strategies have been proposed for the stabilization of these structures, which have shown to be very reactive when exposed in air, rearranging in a sp^2-form through crosslinking reactions.

With the rise of the nanomaterials, new tools were needed for the observation and the measurement of properties at the nanoscale level. In this context, the scanning tunneling microscopy (STM) has emerged among the other microscope technologies as a powerful technique for the analysis of nanostructures with extremely high spatial resolution, even down to the atomic level. It is based on a quantum phenomenon called "the tunneling effect", which allows the transfer of electrons from the tip to the sample through a potential barrier. The high sensitivity of the instrument derives from the sharpness of the tip, which ideally contributes with a single atom to the tunneling current. By means of the

STM one can image the nano-sized features of the scanned surface, and obtain information about the morphology, structure and electronic properties. In addition, spectroscopy measurements can be performed with the aim of providing useful information on the local density of states (LDOS) of the surface. This technique is called scanning tunneling spectroscopy (STS).

This thesis work has been entirely dedicated to the investigation of sp-carbon chains deposited via on-surface synthesis on an Au (111) substrate in ultra-high vacuum conditions. The deposition procedure has been conducted inside a vacuum apparatus by the thermal evaporation of specific precursors. The STM has been employed for the in-situ characterization of the morphological and structural properties of the sample, while insights into the electronic structure have been provided by the interpretation of differential conductivity maps and STS spectra, acquired on different sites over the sample surface. The vibrational structure has been studied through the analysis of Raman spectra, which have been acquired ex-situ. Annealing cycles have been carried out on the deposited sample, in order to investigate the effects of the increasing temperature on molecular chains. Furthermore, preliminary experiments on the chemical characterization have been conducted by means of Auger spectroscopy measurements and the results have been reported in the appendix at the end of this work.

The structure of this thesis has been divided in 5 chapters, whose content has been summarized in the following:

Chapter 1: A general overview on the world of carbon allotropes, with a particular attention on one-dimensional systems. At first, theoretical models of the ideal infinite wire and finite length systems are introduced. Then, Raman spectroscopy and few fabrication techniques of linear carbon structures, reported from literature, are treated in detail. Concluding, potential applications of both pure and hybrid sp-carbon systems are illustrated.

Chapter 2: In the first part, theoretical works, which have contributed to the formulation of the STM and STS theory, are discussed. Whereas, in the second part, few recent experimental works on the STM/STS characterization of sp-carbon chains are reported from literature. At the end of the chapter, goals and objectives of this work are stated.

Chapter 3: The ultra-high vacuum apparatus is described. Moreover, materials and methods employed in the fabrication of the sample are introduced.

Chapter 4: A large discussion over the experimental results. A particular effort is dedicated to the study of morphological and structural properties of the deposited molecular chains through the analysis of STM images and line profiles. Differential conductivity (dI/dV) maps and STS spectra are then investigated, in order to provide some relevant information on electronic properties. In conclusion, experimental and DFT-calculated Raman spectra are compared, with the aim of giving some hints over the vibrational properties of the deposited structures.

Chapter 5: Experimental results are summarized and important conclusions, concerning interactions between deposited molecules and the substrate, are drawn. In addition, possible future works, as natural continuation of the experiments described in this thesis, are proposed.

Appendix: Preliminary chemical characterization of the sample surface by means of Auger spectroscopy.

The thesis activity has been conducted in the Micro and Nanostructured Materials Laboratory (Nanolab) of Politecnico di Milano. I personally worked on STM/STS measurements and Auger spectroscopy analyses of the sp-carbon wires/Au (111) sample. I contributed to the acquisition of Raman spectra. DFT-simulations have been provided by A. Milani, who collaborated with me at the Nanolab.

Chapter 1

Carbon atom wires

Carbon is a chemically versatile element that is present in nature in a variety of allotropic forms. Its polymorphism depends on the different hybridization states which it can adopt. sp-, sp^2- and sp^3- hybridized atomic orbitals give rise to linear, planar and three-dimensional carbon systems, which can be represented by molecules of alkynes, alkenes and alkanes, respectively. As far as condensed matter is concerned, instead, graphite and diamond are the crystalline solid sp^2- and sp^3- hybridized-carbon species. The possible existence of third crystalline solid allotrope based on sp-carbon linear chain, the carbyne, is still under investigation by both the chemistry and physics communities.

Furthermore, in the last 30 years, many other carbon-based structures have been discovered or, in certain cases, just predicted. These are, for example, the fullerenes, the carbon nanotubes and the graphene. The wide variety of carbon allotropes can be represented in the ternary diagram of carbon nanostructures, which is shown in figure 1.1.

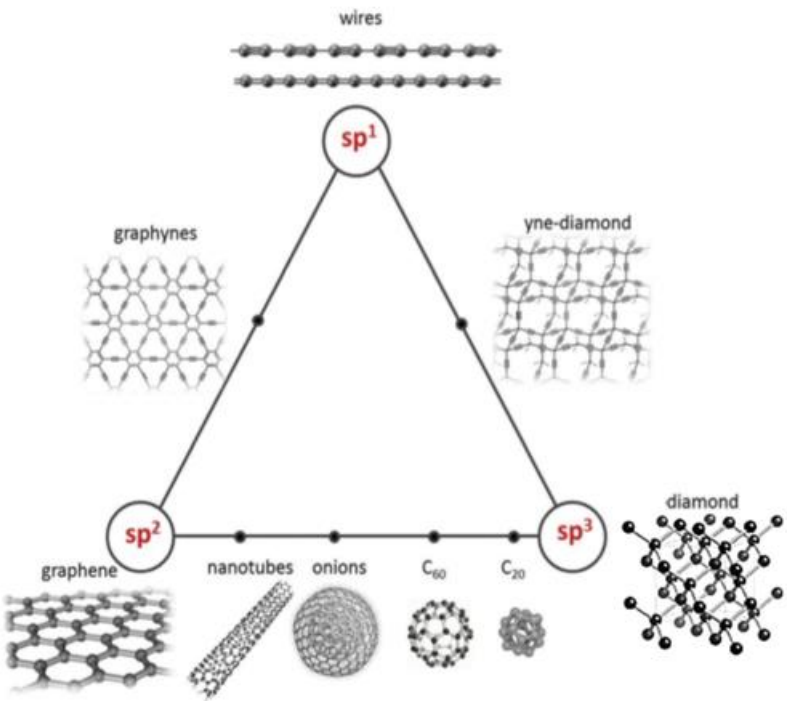

Figure 1.1 Ternary diagram of carbon nanostructures. [1]

As one can observe the vertexes of the triangle are occupied by carbon wires, graphene and diamond, which are the simplest carbon structures, based on the three carbon hybridization states. Along the edges of the triangle, instead, all the other possible combinations are placed, such as fullerenes, nanotubes, graphynes and yne-diamonds.

These last two carbon structures are hybrid species, based on sp-sp^2 and sp-sp^3 carbons, respectively.

The recent discoveries in the field of carbon allotropes has opened new opportunities and pushed the researchers to investigate over the existence of new allotropic forms. Indeed, some of them have displayed unusual excellent properties, making these materials interesting from the industrial and scientific point of view [2]. Among the most promising novel materials, sp-carbon chains have emerged as potential candidates for applications in nanotechnology and material science. We will focus our attention on them, reviewing, in the following, firstly their structural, electronic and vibrational properties and secondly their synthesis processes. Concluding the chapter, some potential applications of sp-carbon-based materials will be reported.

1.1. Linear sp-hybridized carbon

Despite a new sp-carbon allotrope, the carbyne, started to attract the attention of the scientific community towards the end of the XIX century, it has been considered as a possible nanostructure only recently. The discoveries on the amazing properties and applications of graphene have raised a renewed interest in novel sp-carbon species. At the beginning, preliminary investigations were conducted by different authors, aimed to provide an in-depth understanding of the structure, stability and the evolution in time of sp-hybridized carbon systems. Results revealed properties far superior than other carbon nanostructures, such as graphene and carbon nanotubes. Due to the difficulties encountered in the synthesis of these structures, they were usually observed in combination with other forms of carbon [4,5]. Lately, more advanced synthesis techniques have been developed, by which it has been made possible to produce samples composed by only sp-carbon systems. Furthermore, experimental results have been supported and confirmed by theoretical and computational analyses, which have allowed a more accurate characterization of these sp-carbon structures. By means of different analysis tools, such as high-resolution microscopy combined with spectroscopic measurement, structural, vibrational and electronic properties have been largely investigated [1,3].

In the last years, CAWs have been proposed as possible alternatives to graphene, nanotubes or other polyconjugated materials in the field of molecular electronics, due to their interesting conducting features. The linear structure is characterized by the π-conjugation effect, similarly to other sp^2-hybridized carbon systems, which implies the delocalization of π-electrons over the whole structure and the formation of a conduction band, where they preferentially travel. Electronic properties and, in particular, the width of the band gap, can be widely tuned, as in other polyconjugated systems, with the wire length and structure. Moreover, by a proper choice of the end groups, a metallic rather than a semiconducting behavior can be favored. However, CAWs are affected by the Peierls distortion, which leads to an alternate structure and a consequent semiconducting behavior.

Some important problems were found in the high reactivity of the sp-carbon atoms, which tend to react and crosslink to from the sp^2- and sp^3- carbon systems. This led to difficulties in the synthesis of very long chains and it is one of the main challenges in the production of sp-carbon systems. Nevertheless, by a proper choice of the end groups it is possible to significantly stabilize the system. For example, by capping the linear sp-carbon chains with sp^2-carbon end groups the possibility of crosslinking is significantly reduced, since these groups act as spacers between chains, and in general the system becomes more stable [6]. In addition to the stabilization of the chain, many other potentialities were revealed by the employment of a proper end group and the control of the wire length, like the tunability of the electronic, optical and structural properties of the sp-carbon linear chain. It was demonstrated that the influence of the terminal groups is increasingly larger in shorter wires [7].

In the recent years, also the integration of these structures with other carbon system was considered, in order to tune to a large extent, the properties of interest for different applications. There have been reported in literature example of sp-hybridized carbon in carbon-metal moieties [8], embedded in matrices [9,10], connecting graphene sheets [11], inside carbon nanotube [12] and forming hybrid $sp/sp^2/sp^3$ systems such as graphynes (GYs), graphdiynes (GDYs) [13], yne-diamonds, or extended three-dimensional structures based on CAWs [1].

1.2. Theoretical models of carbon atom wires

Before illustrating the structural, vibrational and electronic properties of linear carbon chains, it is better to clarify the existing nomenclature of sp-carbon. In literature there exist many controversies about the definition of sp-hybridized carbon systems. Here, with the term *carbyne* we indicate the ideal infinite wires formed by covalently bonded sp-carbon atoms. If more carbynes are packed together forming a crystalline solid, the resulting structure is called *bulk carbyne*. Real finite sp-carbon systems instead are indicated as *carbon atom wires* (CAWs), which include also the moieties comprising sp-carbon in amorphous systems.

1.2.1. Ideal infinite wires: the carbynes

As graphene is the ultimate planar carbon system obtained by isolating a single layer out of graphite, the carbyne represents the ultimate linear system, since it is a one-atom thick wire. However, unlike the infinite 2D and 3D crystals, in the case of CAWs, it is not so simple to obtain a system extended enough to be reliably approximated by an infinite one, due to high reactivity of the sp-carbon. The longest carbon wire ever synthetized in isolated form was obtained by Tykwinski and Chalifoux and it was just 44-atoms long [6]. It has been calculated by means of the density functional theory (DFT) that the transition from a finite-length system, ruled by the chain end effects, to an ideal infinite linear system occurs for chains having more than 50 atoms [14]. This means that we are not very far to synthetize systems which can be truly considered as a carbyne.

A first distinction for carbynes is based on the two possible arrangements of the carbon atoms within the unit cell (figure 1.2).

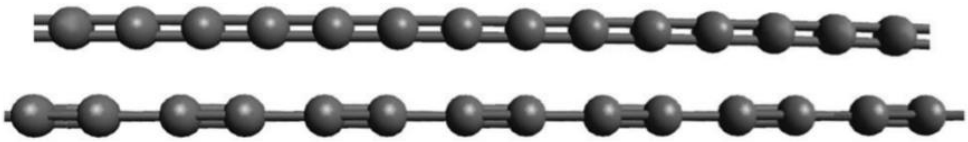

Figure 1.2 The two possible configurations of the carbyne: cumulene (top) and polyyne (bottom). [1]

One structure is composed by equivalent double bonds between carbon atoms and can be represented by a monoatomic unit cell. This is referred to as polycumulene, or just cumulene. The other structure is an alternated sequence of single and triple covalent bonds, which are respectively slightly shorter than that in ethane (ca. 1.5 Å) and slightly longer than that in the acetylene (ca. 1.2 Å). This distortion effect is due to the π-electron delocalization. This system is called polyyne. The unit cell of this type of structure contains two carbon atoms, since they are no longer equivalent, as in the cumulene. As a consequence, the periodicity of the polyyne is double the one of cumulene. This results in a half Brillouin zone in the case of the polyyne, since its edges are inversely proportional to the periodicity of the structure.

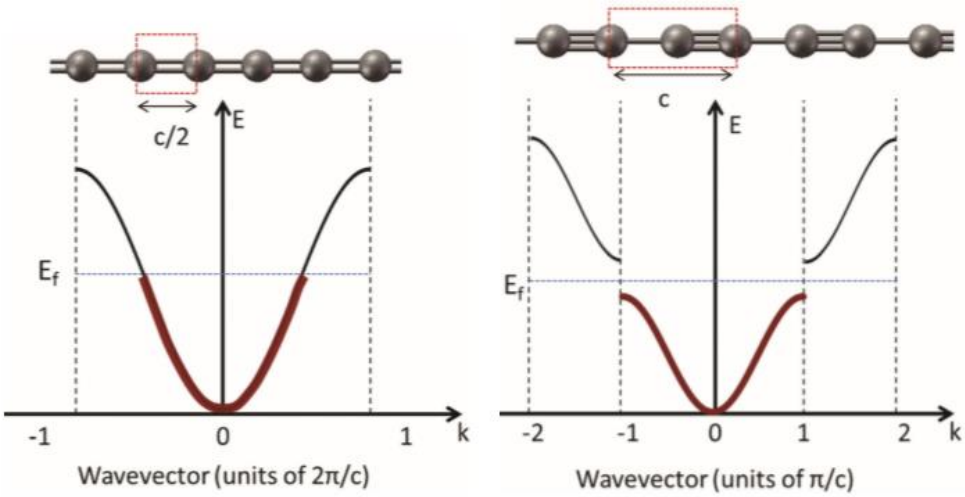

Figure 1.3 Band structures of the two carbyne configurations according to the nearly-free electron model: cumulene (left) and polyyne (right). The opening of the band gap is observed in the polyynic configuration. [1]

The nearly-free electron model for the two chain configurations is illustrated in the figure 1.3. As one can observe the cumulene is a metal since the conduction band is half filled. In polyynes instead the empty conduction band is separated from the completely filled valence band by an energy gap opened at the edges of the Brillouin zone, leading to the semiconductor behavior of this configuration. It becomes clear, hence, how the electronic behavior of the carbyne strictly depends on the conjugation properties of the carbon atoms in the chain. With the aim of simplifying the treatment of the dependence of the carbyne properties on the chain configuration, a useful parameter is defined: the bond

length alternation (BLA). It is defined as the difference in bond lengths for adjacent bonds, as shown in figure 1.4.

Figure 1.4 Definition of the bond length alternation (BLA) parameter. [3]

Hence, BLA is zero for cumulene structures and is different from zero in polyynes. The cumulene and polyyne configurations do not have however the same probability of occurrence, since CAWs are, as happens for other polyconjugated materials, affected by Peierls distortion. This states that the cumulene structure is unstable upon changes in BLA and undergoes a transition to a more stable alternated configuration when BLA is moved from the ideal value of zero. Conditions for the stability of the CAW configuration are well illustrated in the figure 1.5, where the plot of the potential energy over the BLA value, obtained by quantum chemical calculations, is reported. One can soon notice that cumulene configuration is a condition of unstable equilibrium, while the less energetic, and thus the more probable configuration, is a polyyne with a well-defined value of BLA.

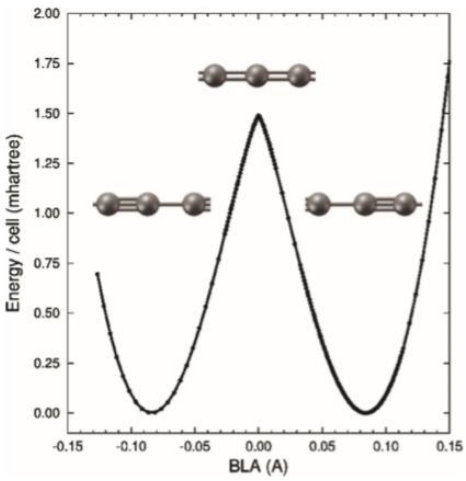

Figure 1.5 Potential energy of an isolated carbyne as a function of BLA. Cumulenic structure (BLA=0) is unstable due to the Peierls distortion and a more stable polyynic form is favored. [1]

So, it is evident how the transition from a metallic to a semiconducting carbyne is significantly affected by the BLA, which consequently has a large influence also on both optical and vibrational properties. Besides the cumulenic and polyyne-like configuration with the minimum energy, other geometries of an ideal infinite wire are not allowed, since they would be unstable. However, in real systems the BLA can be tuned by means of chemical or physical processes and different configurations are obtained. For example, the end group effect is an effective way of modulating the BLA. Hence, a finite-length linear system can be investigated by considering an appropriate infinite chain model with the same value of BLA. The possibility of modulating the properties of a CAW by changing the BLA makes them a very appealing material for potential applications in technology.

Pseudopotential DFT calculations [15] confirmed the trend in the wire conductivity by varying BLA values. In figure 1.6 the evolution of the band structure and the linear dependence of the band gap with the increasing BLA are reported. For the ideal cumulenic configuration (BLA=0) the band gap tends to zero, i.e. the structure behaves like a metal.

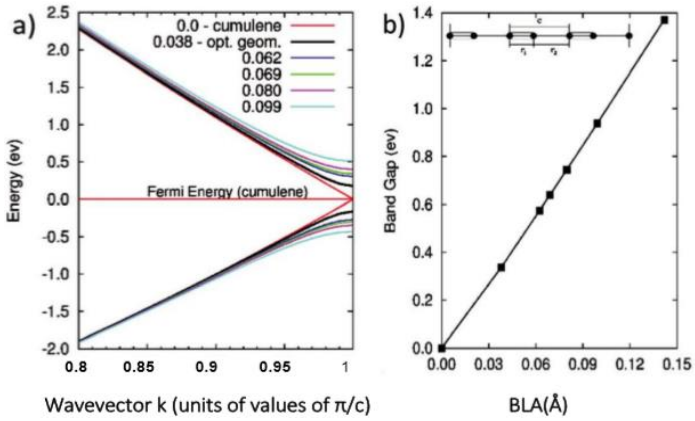

Figure 1.6 (a) Calculated band structures of carbyne with different values of BLA (in Å). (b) Band gap values as a function of BLA. [1]

We now look at the vibrational properties of carbynes, that are expected to change with the BLA, due to electron-phonon coupling, like in all the other π-conjugated systems. The phonon dispersion relationship differs from cumulenic to polyynic configuration and this arises from the different number of carbon atoms in the respective unit cells. As far as cumulene is concerned, only the three acoustic phonon branches (one longitudinal and two transversal) are displayed, since only one atom composes the unit cell. The polyynic structure, instead, presents two atoms in the unit cell and this leads to the appearance of three optical phonon branches. Phonon dispersion relationships for both cumulene and polyyne are illustrated in the figure 1.7.

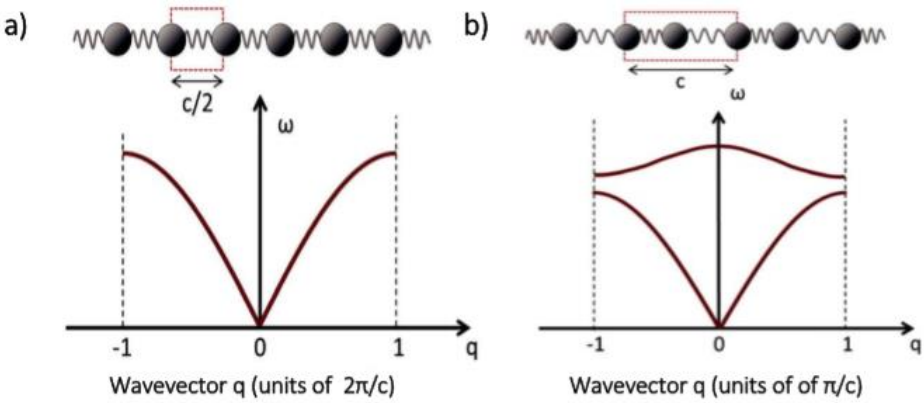

Figure 1.7 Phonon dispersion branches of the two possible configurations of the carbyne: cumulene (left) and polyyne (right). No optical phonon branches are observed for the cumulenic structure. [1]

Hence, we expect cumulenes, unlike polyynes, not to show any optical activity. However, this is valid only for ideal infinite cumulenic structures. In fact, in finite-length cumulenes,

the BLA is affected by terminal endcapping groups and the spectroscopic behavior will deviate from the infinite chain model.

By means of the tight-binding model, which couples the vibrational dynamics to the changes in the electronic structure, it was possible to compute the longitudinal optical branch of the polyyne with varying BLA (figure 1.8).

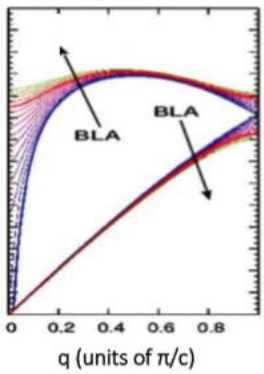

Figure 1.8 Sketch of optical and acoustic phonon dispersion relationships for carbynes as a function of BLA. [1]

As one can observe the phonon wavenumber at q=0 changes from 1200 cm^{-1} to more than 2000 cm^{-1} for increasing BLA. Furthermore, an overbending of the phonon dispersion results in the proximity of the center of the Brillouin zone. This effect is related to the inclusion in the harmonic potential of long-range interactions beyond the nearest neighbor approximation. The strength of these vibrational interactions increases for decreasing BLA.

Concluding this section, it is worth mentioning some of the outstanding properties of carbynes, which have been measured, or, in some cases, just predicted. These have been summarized by C.S. Casari and A. Milani in a recent review article [3].

Property	Value (cumulene/polyyne)
Effective surface	13,000 m^2/g
Young Modulus	32 TPa
Thermal conduction	200–80 kW/m K
Electron mobility	$>10^5$ cm^2/V s
Electronic behavior	Metal/semiconductor
Optical absorption	7.5×10^5 L/mol/cm

Table 1.1 Some predicted or measured outstanding properties of carbynes. [3]

If we compare the values reported in the table 1.1 with those of other nanostructured materials, we can soon notice the superiority of carbynes. The effective surface was estimated to be around 13000 m^2/g, which is four times larger than the theoretical value of graphene. CAWs appear also to be the strongest material ever considered, with a Young

modulus up to 32 TPa and a specific stiffness of about 10^9 N m/kg, which are much higher than all other materials, including carbon nanotubes, diamond and graphene. Carbynes overcomes carbon nanotubes and graphene also in thermal conduction, with a thermal conductivity which ranges from 200 to 80 kW/m K. This excellent thermal conductivity comes from the fact that phonons with high frequencies can travel for long distances before being scattered, i.e. they are characterized by a high free path parameter. Thermal transport occurs thus in a ballistic regime, which holds up to the micron-scale [16]. Electronic properties are relevant as well in carbynes. As previously explained, cumulenes are expected to behave like a metal, while polyynes like a semiconductor, with very high electron mobilities and significant conductance behavior. The optical absorptivity has shown an increase with the number of atoms in the chain**,** reaching a value of 7.5 x 10^5 L/mol/cm.

1.2.2. Finite-length systems

Only in very long chains (more than 50 carbon atoms) the Peierls distortion becomes effective on atom disposition along the chain, that is when it can overcome the BLA decrease given by π-electron delocalization [14]. As far as short finite chains are concerned (i.e. real systems), instead, the BLA and consequently structural, electronic, vibrational and optical properties are affected by the chemical nature of end groups, which terminate the linear structure. Hydrogen-capped polyynes, for example, present an alternated structure, which comes from the single bond of the -CH terminal group. This in fact requires the presence of a triple bond on the adjacent CC linkage, which in turn leads to a formation of a single bond on the next CC and so on, like a domino effect. On the contrary, the vinylidene group (i.e. $-CH_2$) induces a CC double bond at the end of the chain, resulting in a more equalized cumulene-like structure. Both the above discussed structures are illustrated in the right side of figure 1.9. It should be stressed that in finite-length systems the cumulene structure is different from the ideal case of BLA=0 and instead it corresponds to a structure with a small BLA, which is markedly different from that found in polyynes. Hence, for real cumulenic chains we expect a not-negligible Raman activity. In figure 1.9, bond lengths in quite long wires (i.e. 30 carbon atoms), with different terminations are shown.

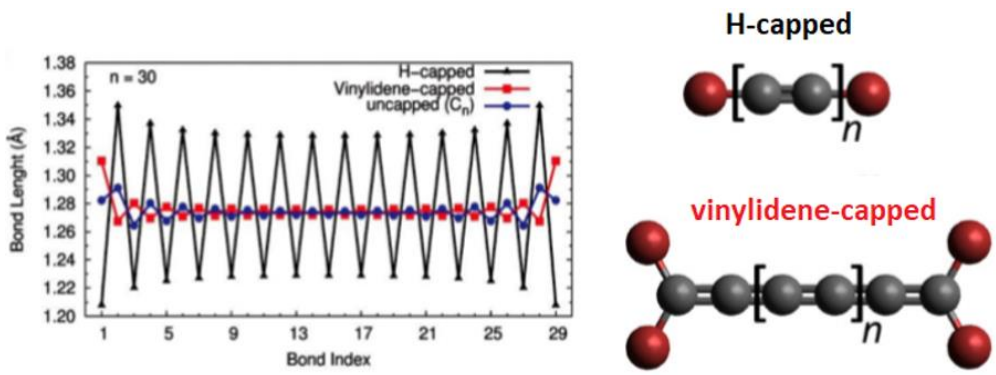

Figure 1.9 (left) DFT calculations of bond lenghts in 30-atoms-long carbynes with different end groups. (right) Molecular models of H-capped and vinylidene-capped carbon atom wires [1]

For these CAWs the chemical nature of end-caps has a larger influence on the structure than the length of the chain. However, as one can observe in figure 1.10, BLA decreases with the increasing chain length, until it reaches an asymptotic lower limit, as ruled by the increasing π-conjugation.

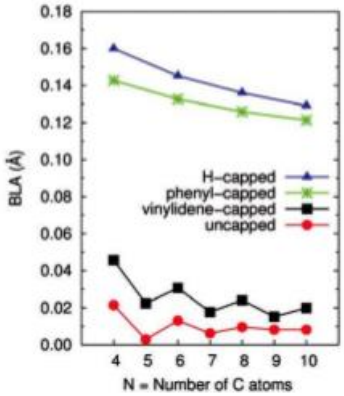

Figure 1.10 BLA as a function of the number of carbon atoms in wires with different terminations. [1]

It also should be noted the polyyne-like structure of the H-capped chains and the cumulene-like structure of the vinylidene-capped chains, as previously described. In Ref. 17 it was clearly demonstrated, by means of the DFT modeling of uncapped cumulene chains and vinylidene-capped chains, that the structural trend in CC bond lengths is a consequence of the termination in short chains.

As we see from the calculations presented above, we cannot establish a strict one to one relation between finite CAWs and ideal infinite wires possessing the same BLA, as proposed in the previous section. However, due to the variance in BLA observed in CAWs as a function of length and end groups, finite CAWs should be related to different models with the same BLA, as their finite counterpart.

It is clear thus how by designing the chain structure, in particular the length and the end groups, we can tune the electronic and vibrational properties of CAWs and this could be the key point for future technological applications, paving the way to a true molecular engineering of CAWs.

1.3. Raman spectroscopy of sp-carbon

The Raman spectroscopy is a powerful technique for the characterization of carbon nanostructures, which allows us to know the vibrational modes in a carbon system and consequently gives us information on the atomic arrangement inside the structure, stability behavior and electronic structure changes induced by charge transfer effects. This is possible thanks to the high sensitivity of this technique to the nature of the CC bonds. Furthermore, the Raman spectrum can provide peculiar structural information, such as the tube diameter in carbon nanotubes or the thickness of few-layers graphite.

As happens in the case of the electronic properties, where a finite-length sp-carbon chain can be placed in correspondence to an ideal infinite model possessing the same BLA, even for vibrational properties an analogous correlation should be worked out.

Like other one-dimensional poly-conjugated carbon systems, such as polyacetylene and polyenes, CAWs show a peculiar behavior which is originated by the BLA oscillation, consisting in an out-of-phase CC stretching. This mode is called "effective conjugation coordinate mode" (ECC mode). A very intense line appears on the Raman spectrum in correspondence of the frequency of this mode, which has been named "α-line". A second minor band ("β-line") has often been observed too, especially in short H-endcapped polyynes. These Raman signals fall in the range 1800-2300 cm^{-1}, depending on the length of the chain. This region becomes specific for sp-carbon, since no other carbon system shows Raman activity within it. In fact, the Raman spectra of sp^2-carbon systems show a maximum frequency of 1620 cm^{-1}, which is the maximum in the phonon dispersion of graphite. Above 2400 cm^{-1} second order Raman peaks appear. Similarly, the peak of diamond at 1332 cm^{-1} represents the maximum frequency in the phonon density of states. In figure 1.11 Raman spectra of different carbon system are shown, highlighting the high sensitivity on hybridization state, electronic structure and local order.

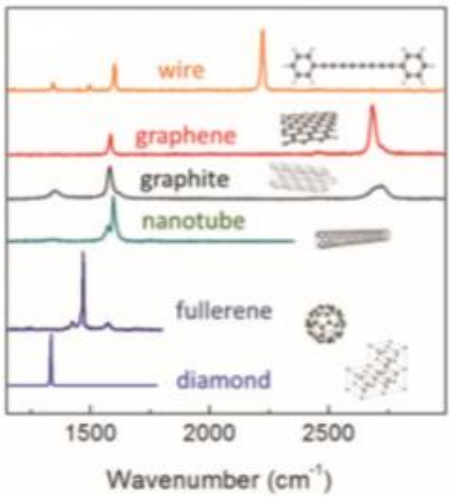

Figure 1.11 Experimental Raman spectra of some carbon allotropes. [1]

In some Raman spectra can be required the enhancement of the signal intensity, since, even if they are present, peaks can be hardly distinguished. In these cases, "surface enhanced Raman spectroscopy "(SERS) is employed, which consists in the amplification of the Raman scattering by means of plasmonic nanoparticles dispersed on the analyzed surface, sometimes reaching the single molecule level. It is based on the local enhancement of the electromagnetic field due to a resonance with surface plasmons present in metal nanoparticles. The enhancement factor can reach values of 10^{10} – 10^{11}. In figure 1.12 an example of SERS of carbon wires, with an enhancement factor of 10^6, is reported.

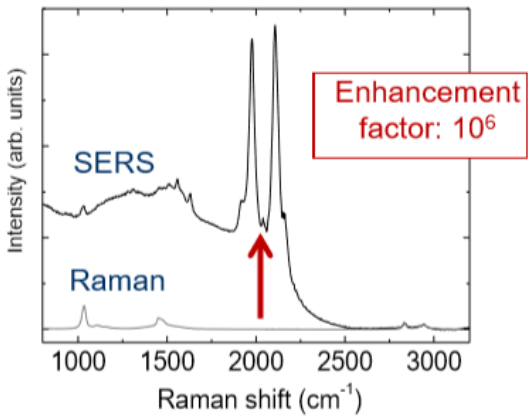

Figure 1.12 Experimental SERS of carbon wires. The enhancement of the Raman signal can be observed. [37]

Furthermore, it can happen that the investigated sample forms a complex with the metal nanoparticles due to charge transfer, leading to an additional enhancement, which is called chemical SERS. Also, a shift in the position of main Raman peaks and the appearance of new spectral features can be observed upon a charge transfer effect. This can be explained since the altered electronic properties affect on structural properties, due to the strong electron-phonon coupling that exists in π-conjugated systems.

Here we report some results found in literature [4], for one of the most Raman-investigated polyynes: the phenyl-endcapped. For comparison, also some properties of the H-endcapped polyynes are introduced.

Phenyl-terminated polyynes are chemically synthesized and are stable even at ambient temperature, thanks to the bulky phenylic endcaps. Hydrogen termination, instead, results in a lower stability and the sp-carbon chain gives rise to crosslinking reactions, showing a transition towards a sp^2-carbon structure.

The Raman spectrum of the phenyl-terminated polyynes is characterized by well-defined peaks in the wavenumber range from 2050 cm^{-1} to 2250 cm^{-1}, as shown in figure 1.13a. Different peaks correspond to the strong characteristic Raman mode (BLA oscillation) of CAWs with different lengths. The wavenumber of the characteristic Raman modes slightly decreases with the chain length, consistent with the increase of π-conjugation. It is evident thus how the length of CAWs influences the vibrational structure of the wire. The experimental result (figure 1.13a) is also supported by the DFT calculations [17] of Raman spectra of phenyl-endcapped polyynes with selected length, which contribute to the final band, as it is shown in figure 1.13b. Furthermore, DFT models showed an increase in the intensity of the ECC modes with the sp-chain length. However, this is not observed in the Raman spectrum in figure 1.13a. The reason is that real poly-disperse samples contain wires of different length in a different amount. As a consequence, in experimental Raman spectra the height of a peak, corresponding to a precise chain length, depends on the abundance of that species in the sample. Hence, DFT methods must take into account the distribution of the chain lengths, to better fit experimental spectra.

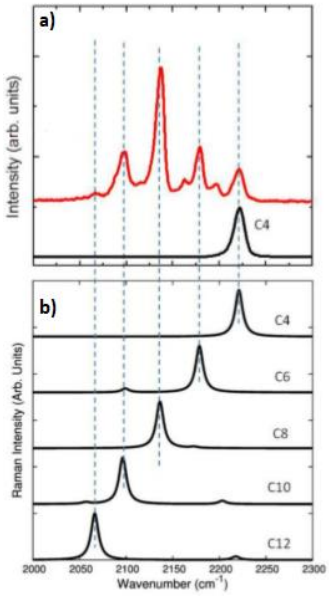

Figure 1.13 (a) Asymmetrical sp-carbon band (red) and the DFT-calculated spectrum of a 4 atoms polyyne (black). (b) DFT calculation of Raman peaks of wires with different length (4, 6, 8, 10, 12). [17]

Changes in the Raman spectrum of phenyl-endcapped polyynes due to the charge transfer effect are illustrated in figure 1.14a, where it is possible to observe the relevant softening of the Raman modes and the increase of the intensity for charged wires, i.e. after the charge transfer effect in SERS. In figure 1.14b, instead, DFT calculations of BLA values are plotted for both H-endcapped and phenyl-endcapped polyynes, showing the evolution from the polyyne-like configuration of neutral wires to cumulene-like configuration of charged wires. This demonstrates that, as previously explained, also structural properties can be affected by the charge transfer effect. In the plot, 'neutral' and 'charged' indicate the wires before and after the charge transfer effect, respectively.

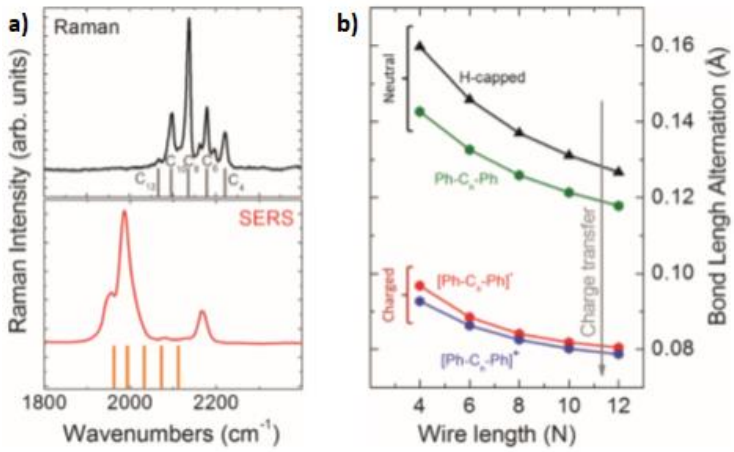

Figure 1.14 (a) Experimental Raman and SERS of phenyl-endcapped polyynes. Lines correspond to the DFT-predicted positions of peaks as a function of the wire length. (b) BLA values for neutral and charged phenyl-endcapped polyynes as a function of the wire length. BLA values of H-endcapped polyynes are reported for comparison. [1]

1.4. Synthesis of sp-carbon systems

In previous sections, we explored the wide tunability of physical properties of CAWs through several chain parameters, such as the BLA and the end groups effect. This makes them an exciting material to be considered for future applications. Problems arise, however, when it comes to the fabrication of these sp-carbon systems. The key issue in the synthesis process turned out to be the stability of the chains. As anticipated in section 1.1, the formed sp-wires undergo crosslinking reactions, leading to an amorphous sp^2-carbon system (figure 1.15).

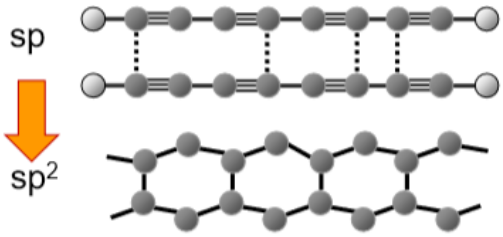

Figure 1.15 Crosslinking reactions between sp-carbon chains.

Several methods for the stabilization of the formed CAWs have been proposed in literature so far. A typical strategy is that of terminating the linear chains with sterically bulky groups, such as, for instance, sp^2-carbon end groups. This solution hinders the arise of interactions between neighbor chains, preventing possible crosslinking reactions, thanks to capping groups, which behave like spacers. Following this approach, Chalifoux and Tykwinski were able to synthetize a polyyne formed by 44 atoms [6]. Furthermore, as far as H-terminated polyynes are concerned, a prolonged stability was achieved by mixing the solution of the formed CAWs with silver colloids [18]. Difficulties not only in the stabilization, but also in the production step have been encountered since the discover of polyynes. Trying to find the optimal procedure for the production of sp-carbon chains, techniques based on different chemical and physical processes have been developed.

In this chapter I present some important techniques for the fabrication of sp-carbon system, illustrating the main mechanism and specifying the operating parameters, such as the temperature and the pressure. These processes are based on both chemical and physical synthesis, and a bottom-up approach is generally preferred.

Physical vapor deposition techniques require the production of a plasma or carbon vapor that is rapidly quenched, by means of inert gases or liquids, forming carbon cluster on the substrate. The vapor can be produced by laser ablation or arc discharge. Several examples of both the techniques can be found in literature. For instance, I mention the method developed by F. Cataldo, that consists in the synthesis of polyynes by arc discharge in liquids [19]. This procedure allows one to control the chain termination by selecting suitable solvents. Concerning techniques based on laser ablation, instead, it is worth quoting a method developed by C.S. Casari et al. [20], based on the nanosecond pulsed laser deposition (PLD) of graphite in a vaccum regime. The obtained thin solid films are

composed by a sp^2-amophous carbon matrix in which sp-carbon wires are dispersed. Here below I explain more in detail how this technique works.

The laser ablation is performed in the presence of an inert gas, such as Argon, with a pressure ranging from 10 to 500 Pa. On the substrate plasmonic metallic nanoparticles are previously deposited, with the aim of enhancing the Raman signal, for further SERS investigations. By varying the Argon background pressure and the target to substrate distance (d_{ts}), one can obtain deposited films with different properties. This emerges in figure 1.16, where one can soon notice the dependence of the Raman signal intensity on the Ar pressure. The sp-carbon peak at 1800-2200 cm^{-1} is significantly maximized for a pressure of 500 Pa.

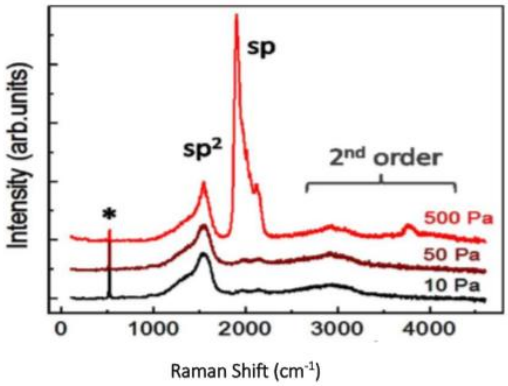

Figure 1.16 SERS spectra of sp-sp^2-carbon films deposited by PLD at different Ar pressures. d_{ts} is fixed at 50 nm. The star indicates the Raman signal of the SERS-active silicon substrate. Spectra are normalized with respect to the intensity of the G band. [20]

Also, a second band is present in the Raman spectrum in the wavenumber range of 1200-1600 cm^{-1} and it corresponds to the G and D modes of the sp^2-carbons of the amorphous matrix. These spectra are acquired on samples deposited with a fixed d_{ts}. The increase in the intensity of the sp-carbon Raman signal is also manifested for progressively higher target-substrate distances, as shown in figure 1.17, where SERS spectra of samples deposited at increasing d_{ts} are reported for both 50 Pa and 500 Pa cases.

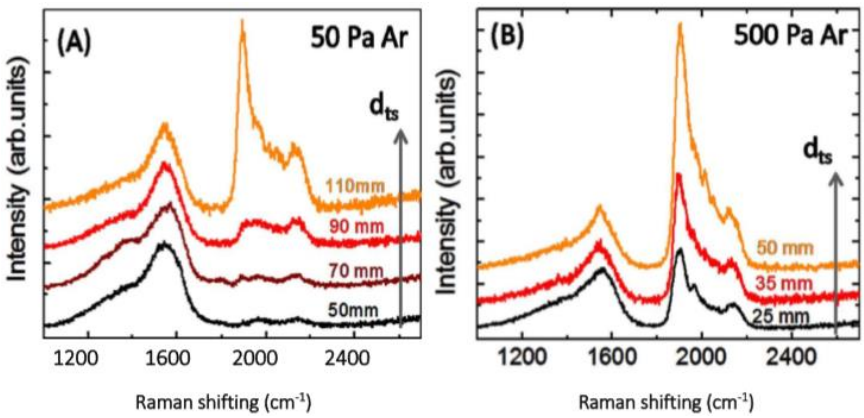

Figure 1.17 SERS spectra for increasing d_{ts} at fixed Ar pressure: (a) 50 Pa and (b) 500 Pa. [20]

As expected, the sp-carbon peak is more intense in the case of 500 Pa than in the case of 50 Pa. Hence, it is evident, how the final product of the deposition is influenced by both the Ar pressure and the d_{ts}. The interplay between these two parameters is well described by the ratio L between d_{ts} and the length of the plasma plume (l_p).

$$L = \frac{d_{ts}}{l_p}$$

The length of the plume, i.e. the distance of the shock front from the target, is influenced by the Ar pressure, which acts as a cooling and confining agent on the plasma, enhancing its visible emission. Value of L lower than one, thus, lead to compact films, where the atoms are deposited one by one, due to the absence of collisions in the travel from the target to the substrate. Value of L higher than one instead favor the deposition of nanoporous layers, since the atoms ejected from the target form clusters before reaching the substrate with a decreased energy. It has been proven that the formation of sp-carbon wires is favored by out-of-equilibrium conditions. Therefore, it is possible to increase the fraction of sp-carbon phase in the whole sample, by selecting a proper value of the L parameter.

As far as chemical synthesis is concerned, instead, two different approaches have been developed so far. The first employs a polymerization strategy and leads to the production of sp-carbon wires in a single step, but polydisperse in size, due to the nature of the process. Examples of this technique are the dehydropolycondensation of acetylene and the polycondensation reactions of halides, which have been reviewed by Kudryavtsev in ref. 21. The second approach is the so-called Glaser reaction [22] and consists in the dimerization reaction of ethynyl groups, forming molecules with a defined length and specific end groups.

Despite a more practical bottom-up approach is generally preferred, synthesis techniques based on a top-down approach have been proposed too. For instance, the electron beam in TEM has been used to selectively remove carbon atoms from a graphene sheet so as to obtain sp-carbon wires suspended between two separated graphene edges [11] (figure 1.18). Another idea was that of pulling carbon nanotubes or graphene in order to produce a wire, as theoretically predicted [1].

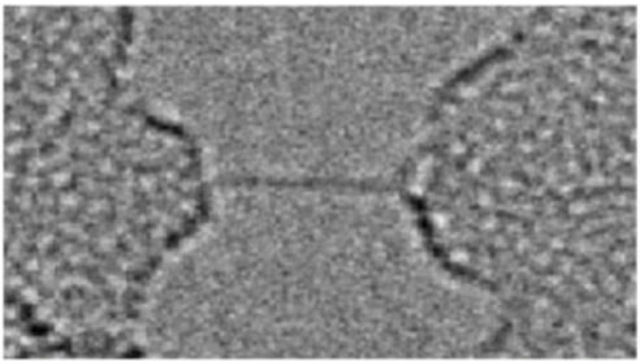

Figure 1.18 TEM image of the sp-carbon wire suspended between two graphene edges. [11]

More recently, a new method for the deposition of sp-carbon chains has emerged, in which the substrate is directly involved in the synthesis process. It is more generally called "on-surface synthesis" and in literature it is possible to find several mechanisms of chain formation, based on different chemical processes.

One of the most relevant works, concerning this technique, is that done by Q. Sun et al. [23] in 2016, which is also the main reference for the experiments conducted in this thesis work. In particular, they successfully achieve the formation of linear sp-carbon chains by dehalogenative homocoupling reactions of the molecule 4,4'-di(bromoethynyl)-1,1'biphenyl (bBEBP) on Au (111) substrate at room temperature. As result of the deposition and a slight annealing at 320 K a formation of an organometallic chain, containing Au atoms between the phenylic groups, was unexpectedly observed. In figure 1.19, the structure of the precursor bBEBP and the organometallic chain are illustrated.

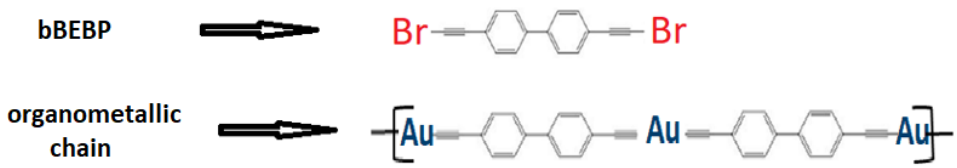

Figure 1.19 Structures of the precursor bBEBP (top) and the organometallic chain (bottom). Br atoms are eliminated during the coupling reaction and Au atoms coming from the substrate are incorporated in the sp-carbon chain.

It was also reported that a further annealing of the sample at 425 K caused the release of Au atoms from the chain, with a consequent formation of acetylenic linkages between phenylic groups. Furthermore, DFT calculations were performed to simulate the model of the C-Au-C species on Au (111), consolidating the hypothesis on the formation of the organometallic intermediates.

The same research group proposed in the same year another method of on-surface synthesis of metalated carbynes [8]. It is based on the dehydrogenative coupling reaction of ethyne molecules on a Cu (110) surface under ultra-high vacuum conditions. In this case, unlike the previous work, where the organometallic chain was observed at low temperature, a relatively high temperature, around 450 K, is required to provide sufficient energy to ethyne molecules to undergo the dehydrogenation reaction. Surface participates actively in the chain formation, since the incorporation of Cu atom in the linear structure. It was also proved that an increase in temperature can lead to the release of Cu atoms from the C-Cu-C organometallic structure.

In both the two above described strategies of on-surface synthesis the presence of alkyne groups in the precursors is required, in order to obtain, following the coupling reactions, the sp-carbon chains. This limitation has been overcome by the method developed by Chen-Hui Shu et al. [24], in which they obtained the in-situ formation of CC triple bonds on Cu (111) via the coupling of specific precursors, terminating with $-CCl_3$ groups, under ultra-high vacuum conditions at room temperature. The final products were poly (p-

phenylene ethynylene) (PPE) molecular wires. In figure 1.20a the precursor and the structure of the obtained nanowire are illustrated.

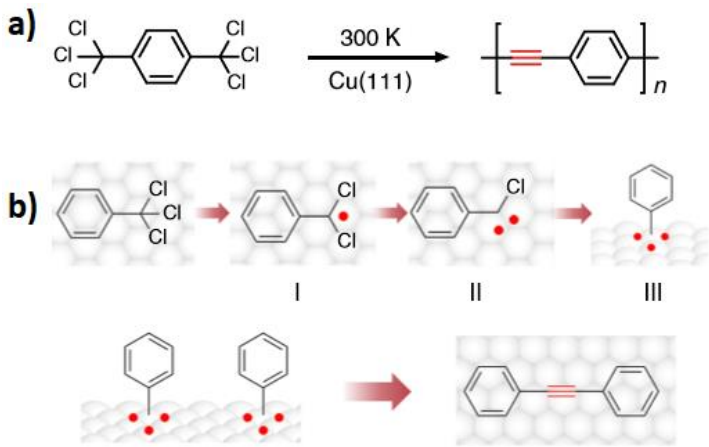

Figure 1.20 (a) Coupling of the precursors to form the PPE molecular wire. (b) Overview of the reaction pathway for the formation of the 1,2-diphenylethyne (DPE). [24]

To better understand the reaction mechanism, they used a monofunctional precursor, possessing only one -CCl_3 group. Their experiments demonstrated that the Cu (111) surface played a significant role in the coupling reaction, not only catalyzing the reaction, but also stabilizing the radical intermediates and constraining the nanostructure into two dimensions. In figure 1.20b, it is possible to observe the surface-mediated dechlorination process from the monofunctional monomer to the carbyne radical (III) and the following coupling reaction between the formed radicals.

Methods of photoinduced on-surface synthesis have been proposed too. This is the case of the work done by Colazzo et al. [25], where the light was employed to induce the homocoupling reaction of terminal alkynes on a highly oriented pyrolytic graphite (HOPG) surface. The role covered by the substrate was mainly that of a supporting platform, orientating the molecules in the proper direction, rather than that of catalyzing agent. Furthermore, no high temperature was required, since the energy necessary for the reaction was entirely given by the absorbed light.

One of the last innovative works about on-surface synthesis of sp-carbon wires is that done by Pavliček and his group, where they succeeded in the generation of tri-, tetra-, hexa- and octaynes (5-8) by atomic manipulation on bilayer NaCl island on Cu (111) [26]. This was achieved by means of pulsed voltages applied at the STM tip, with the aim of rearranging the atoms in the desired geometry.

Concluding this section, it is important to remark that the majority of reports and studies about the synthesis of carbynes in literature concerns the formation of polyynic chains rather than cumulenes. This is related to the difficulties encountered in the fabrication of cumulenic structures, since they are less stable and so harder to obtain. However, their synthesis has been reported by some authors, like Cataldo [27], and more recently Tykwinski and coworkers [28], which describes the production of cumulenic wires up to 8

atoms by means of stepwise chemical synthesis. This technique offers the possibility to terminate the chains with different groups, which, as explained at the beginning of this section, appears to be a powerful strategy to control the structure of the carbon wire. Cumulene-like structures have also been observed together with polyynes in a pure sp-sp^2-carbon cluster-assembled system, showing a higher tendency, compared to the polyynic fraction, to undergo the transformation to the sp^2-carbon structure.

1.5. Potential applications of sp-carbon-based novel materials

As described in previous sections, CAWs have attracted the attention as possible materials for future applications in nanotechnology and materials science, due to extended tunability of their structural, mechanical, electronic and optical properties, which have been predicted to outperform those of other nanostructured materials. A noteworthy number of theoretical studies have been conducted with the aim of investigating optical, mechanical and transport properties of these systems, evidencing a dependence on the BLA, the nature of the wire termination, the applied strain, the doping level and the number of carbon atoms in the chain.

Studies based on UV/vis spectroscopy of CAWs showed a nonlinear optical behavior of these structures, which resulted to be mainly related to sp-hybridized carbon structure rather than on the nature of the end groups [4]. Sp-hybridation is also the origin of the extremely high tensile strength of CAWs, which have been predicted to be way higher than that of nanotubes and graphene, as described in section 1.2.1.

Concerning transport properties, a number of theoretical studies can be found in literature, pointing out the outstanding electronic and conductance properties of isolated sp-carbon systems. In works done by Lang and Avouris the oscillatory behavior of the conductance of wires, contacted by gold leads, with the increasing number of carbon atoms was investigated [29]. In particular, odd-numbered CAWs showed a constant conductance with the wire length, close to the theoretical maximum $2G_0$, where G_0=77μS is the quantum of conductance, as described by the Landauer formula. Even-numbered wires, instead, were predicted to display a lower conductance compared to odd-numbered ones, which showed an increasing behavior with the number of carbon atoms. These results derive from different density of states of the two species at the Fermi level, and the mixing with metal states of electrodes. The effects of the strain on transport properties were analyzed by Tongay et al. [30], with studies on infinite cumulenes. They considered electrode-wire-electrode systems, in which electrodes were composed by metallic CAWs. Unstrained wires showed a quantum-ballistic transport with a constant conductance of $2G_0$ in a wide energy window around the Fermi level, while strained wires were predicted to be characterized by an oscillatory behavior of the conductance as a function of the electron energy. Also, Yakobson and coworkers [31] conducted theoretical studies on transport properties of strained CAWs, investigating the modulation of the bandgap with the mechanical strain. They found that unstrained chains showed a

cumulenic configuration, with a consequent metallic character, as previously explained in section 1.2.1. The application of the strain, instead, caused the change to the polyynic form and so to an insulating behavior.

Despite the huge amount of theoretical works, only few studies have reported experimental investigations of CAWs. This is related to the problems and difficulties encountered in the production and in the stabilization of sp-carbon system. For this reason, many experimental works concern the characterization of integrated structures formed by CAWs and sp^2-carbon. Here we discuss few examples of these novel materials of potential interest, starting from disordered sp-sp^2-carbon systems. These were fabricated by supersonic cluster beam deposition and they showed a dependence of electrical conductivity of the whole system on the sp-carbon content [9].

Chain termination by sp^2-conjugated end groups have been proposed for the stabilization and modulation of the properties of CAWs. In this field graphene has been considered as a natural termination for CAWs and the system graphene-wire-graphene has been investigated as a potential structure for applications in all-carbon nanoelectronics (figure 1.21)

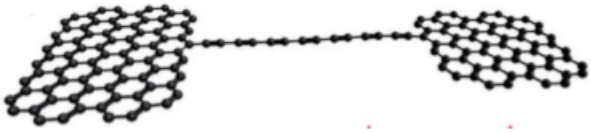

Figure 1.21 CAW suspended between two graphene sheets. [1]

DFT calculations have been performed to investigate the influence of sp^2-conjugated terminations of increasing dimension up to graphene on the structure and electronic properties of the sp-carbon chain [32,33]. As emerged from these DFT models, the chemical connectivity between sp-carbon atom and graphene has a larger effect on the wire compared to the extension of the sp^2-carbon domains, which is almost uninfluencing. In particular, as it has been shown by many authors, a single bond between the sp-carbon and graphene would lead to a polyyne-like structure, while a double bond should induce a more regular cumulene-like configuration.

F. Banhart and coworkers succeeded in the fabrication of this graphene-wire-graphene system, by means of an electron beam in TEM and they observed the changes in the wire conductivity, under different strain conditions, confirming the predicted metal-to-semiconductor transition, as explained above [34].

CAWs have been also observed inside carbon nanotubes (figure 1.22), which act as protecting cage, permitting in this way to achieve very long and stable chains. These systems, in particular CAWs in the core of double-walled CNTs, have shown to be promising for optoelectronic application, since they displayed very good optical absorption maxima, strongly dependent on the wire length.

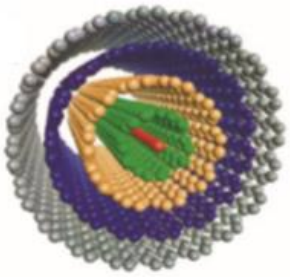

Figure 1.22 CAW in the core of a multi-walled carbon nanotube. [12]

Recently, novel systems related to CAWs, started to attract as possible alternatives for graphene. These are the graphynes (GYs) and graphdiynes (GDYs). The first ones consist of carbon networks formed by acetylenic linkages (-C≡C-). Depending on the nature of the junctions between the linkages, different graphynes have been proposed. For instance, the γ-graphyne presents sp^2-carbon hexagons between -C≡C- bonds, instead the α-graphyne is composed by linear bonds only, as a sp-carbon counterpart of graphene. Graphdiynes are obtained by replacing a single acetylenic linkage with a double one (-C≡C-C≡C-). Theoretical studies have indicated great potential for these systems, predicting appealing mechanical, electronic and optical properties. Compared to graphene, GYs and GDYs should possess lower plane stiffness, due to the presence of linear bonds, but comparable bending stiffness. As in the case of isolated sp-carbon chains, these hybrid systems show a tunable gap when a strain is applied. The electronic properties have been computed for different structures and a high carrier mobility has been predicted, comparable to that of graphene. Furthermore, vibrational properties have been calculated and all the Raman active modes have been predicted to be in-plane.

Despite many theoretical studies have been conducted about such systems, experimental works about the production and characterization are still at an early stage. One of the preliminary studies about the synthesis of GYs and GDYs have been done by the group of Haley [35] and by Diederich et al. [36], where they achieved the fabrication of sub-fragments of the carbon network of different topology and dimension. More recently Xu and coworkers have shown that the homocoupling of halogenated precursors deposited on a gold surface is suitable for the fabrication of GDY-like systems [23]. In figure 1.23a-b it is possible to observe STM images of the 2D-ordered network, composed by sp-carbon linkages between hexagonal carbon rings.

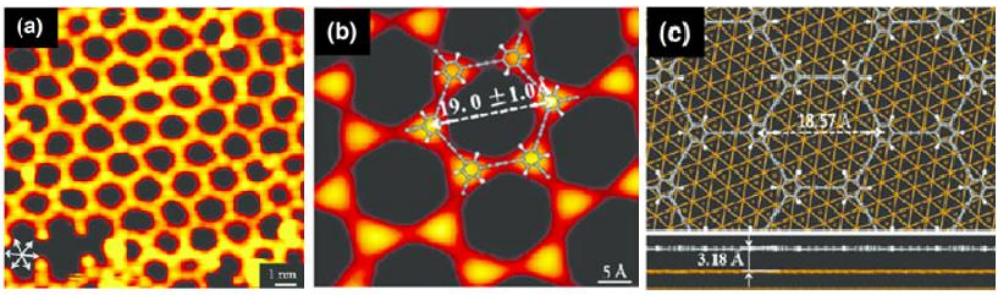

Figure 1.23 STM images (a,b) and simulation (c) of the GDY-like structure produced by the dehalogenative homocoupling of halogenated precursors on Au (111). [23]

Starting from graphyne and graphdiyne, in analogy with graphene, one can imagine forming novel nanostructures such as graphyne nanotubes, nanoribbons and quasi-0D systems, such as fullerene-like systems. Like for conventional sp^2-carbon nanotubes the electronic behavior depends on the chirality of the tube. In nanoribbons, instead, the energy gap increases with decreasing the ribbon width.

Concluding, two hybrid carbon systems are reported, which have been only theoretically considered. The first is a system composed by graphene layers connected each other by perpendicularly-grown sp-carbon wires, a sort of graphite-like structure with intercalating CAWs. The second is the so called yne-diamond, i.e. a 3D network of sp-wires joined by sp^3-carbon atoms, forming a diamond-like structure. Both the nanostructured materials are illustrated in the figure 1.24.

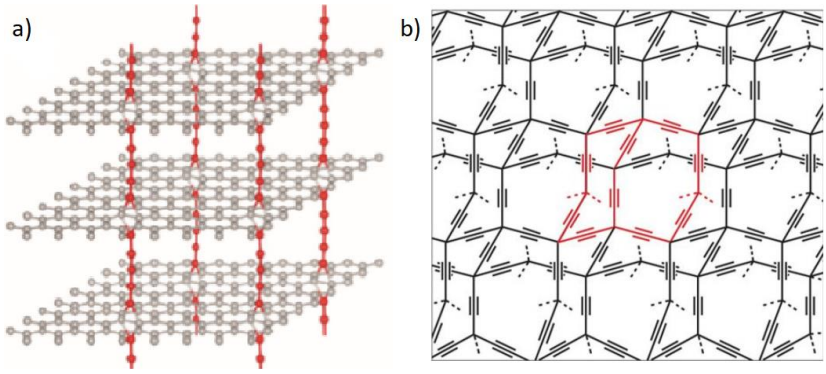

Figure 1.24 (a) Graphite layers connected by vertically-grown sp-carbon chains. [38] (b) Representation of the 3D structure of the yne-diamond. [1]

Chapter 2

Scanning tunneling microscopy and spectroscopy

The invention of the Scanning tunneling microscope (STM) dates back in 1982, with the pioneering work by G. Binning H. Rohrer [39] at the IBM Zurich Research Laboratory, concerning surface analyses of $CaIrSn_4$ by means of the first example in the history of STM. Few years later, in 1986, the two scientists were awarded with the Nobel prize in physics.

STM can be inserted in a wider branch of microscopy: the scanning probe microscopy (SPM). A scanning probe microscope, in general, consists in a tip which moves back and forward on a specimen and it is able to scan the local properties of the surface at the nanometer scale or, in certain cases, even down to atomic level. The extremely high resolution derives from either the small tip apex, which can be reduced ideally to a single atom or the probe actuator which is able to moves with precision and accuracy at the nanometer scale. Depending on the nature of the interaction between the sample and the tip, different scanning probe techniques have been developed during the years. Besides the STM, among the most used in the research field we mention the atomic force microscopy (AFM) and the magnetic force microscopy (MFM). Depending on the type of SPM employed in the investigation of the sample, different properties can be measured at different scales.

In the following, firstly, the general working principles of STM will be presented. In addition, theoretical aspects of the tunneling in solids and in the specific case of STM will be treated. Concluding the chapter, a general overview on the spectroscopy technique implemented in the STM, the scanning tunneling spectroscopy (STS), will be given.

2.1. Working principles of scanning tunneling microscopy

With the STM we are able to image atoms, molecules and, in general, nanostructures, manipulate atoms and measure surface electronic and magnetic properties.

The basic principle of the STM is a quantum mechanical phenomenon called “tunneling effect”. It consists in the flow of electrons between two conductive or semi-conductive electrodes, through a potential barrier, which is identified, in the case of STM, by a vacuum gap. In order to allow the tunneling current to travel across the barrier it is necessary that the electrodes, which in STM are the tip apex and the front atom on the sample surface, are distant less than 1 nm. The tip is usually mounted on a piezoelectric actuator, known usually as a scanner, which is free to move on the sample plane and vertically with respect to it with a picometer precision. The direction of the current flow is determined by the applied voltage (bias) between the tip and the sample. If no bias is applied, an equilibrium situation of zero current occurs. A scheme of the STM components is reported in figure 2.1.

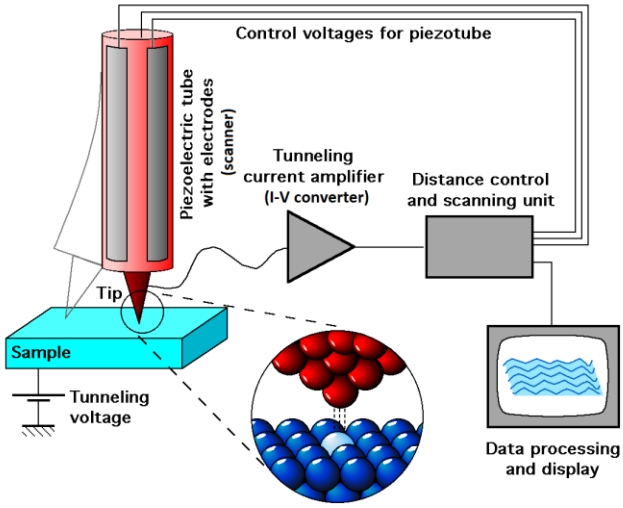

Figure 2.25 Schematic view of an STM unit.

Furthermore, the intensity of the current depends on several parameters, such as the density of states of the two electrodes and the height and width of the potential barrier. The distance between tip and sample, i.e. the width of the barrier, has a large influence on the current, since the transmittance coefficient has a strong exponential dependence on it. As a consequence, the majority of the current is localized on the nearest neighbor atoms and this results in a very high resolution at atomic level. The lateral resolution is of the order of 1 Å, while the vertical one is two order of magnitude higher, around 0.01 Å. In an ideal situation, only the orbitals of the closest facing atoms of the tip and sample should be involved in the tunneling transport, however it is extremely difficult to reach this optimum condition, since most of the times more than one atom contribute to the current. This problem is strictly related to the difficulty to obtain a single atom terminated tip.

In order to perform a topographic scan of the surface, a feedback system is implemented. It receives, as input signals, the tunneling current, measured using a current-voltage (I-V) converter, the applied bias and setpoint current imposed by the operator. As output signal the feedback system makes the piezoelectric actuator move up and down so as to maintain the tunneling current constant at the value of the chosen setpoint current. In this way the tip follows the surface profile and the vertical position of the tip gives us the topographic map of the sample. This is the so called constant current mode (CCM) and is mostly used for surfaces with a disordered structure, such a stepped surfaces or surfaces with adsorbed atoms and molecules. It is also possible to perform the imaging of the surface by switching off the feedback system so as to keep the vertical position of the tip constant. In this case the surface topography is obtained by looking at the tunneling current map. One advantage of this imaging mode (constant height mode, CHM) is that the scan speed can be increased with respect to the constant current mode. There is a reduced risk for the tip to collide against surface protrusions, since this technique is usually applied on flat surfaces, with minimal number of defects and also because the distance from the sample is relatively high. When instead the CCM is adopted, and the

feedback system is active, the operator must be careful to choose the optimal sensitivity of the feedback and scan speed in order to avoid possible tip damaging. The CCM and CHM are illustrated in the figure 2.2.

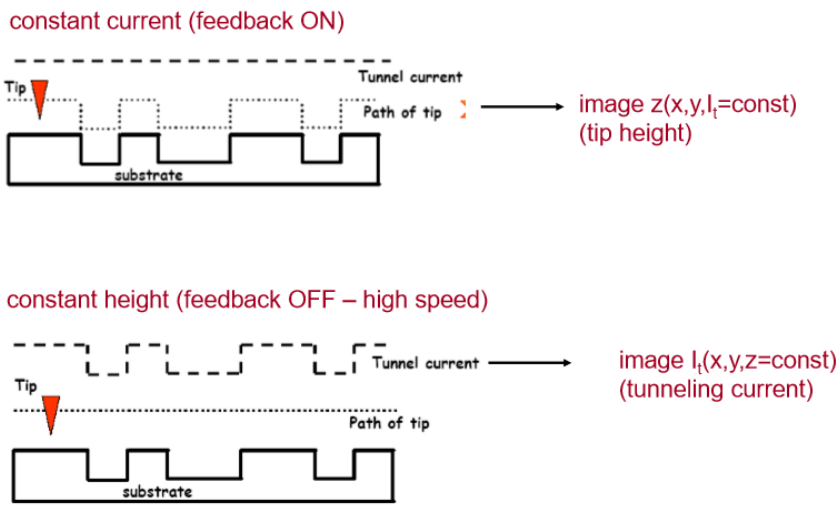

Figure 2.26 The two STM imaging modes: constant current mode (top) and constant height mode (bottom).

Typical operating values for the main parameters are reported in the table 2.1.

Bias	10 mV – 10 V
Tunneling current	pA – nA
Scan rate	1 – 10 Hz

Table 2.2 Typical operating values of applied bias, tunneling current and scan rate.

Furthermore, it is possible to exploit STM to perform spectroscopy. By means of this technique, scanning tunneling spectroscopy (STS), information about the local density of states (LDOS) can be extracted from the tunneling current signal, which is elaborated by a specific apparatus, the Lock-in amplifier. This technique will be analyzed in detail in section 2.1.3.

The high spatial resolution in STM measurements is affected by two limiting factors of different nature: electrical and mechanical. The former is the noise in the tunneling current channel, which can originate both from undesired signals from electric wires in the proximity and from the I-V converter. However, the noise is usually very small, and a proper wiring is enough to stabilize the tunneling current. The latter is due to instabilities in the tip-sample distance. These can be related to mechanical vibrations of the scanner or thermal deformations. In order to limit this problem and achieve a picometer-scale stability of the tip and sample positions, a damping system for the STM chamber is combined with a mechanical and magnetic damping of the scanner, which isolates it from the rest of the chamber. It is possible to further increase the stability of the measurements by cooling the system down. In literature temperatures approaching the absolute zero have been reached [40].

2.2. Theory of scanning tunneling microscopy

There exist different approaches to treat the base theory of STM. In the following we go firstly through the base quantum mechanical theory of elastic tunneling effect and then I show how this theory can be extended by the Bardeen's approach [41] and by the Tersoff and Hamann model [42].

2.2.1. The tunneling effect

In this section we model the tip-sample interaction by using a one-dimensional potential barrier (figure 2.3), that represents the vacuum gap, the classically forbidden region for electrons.

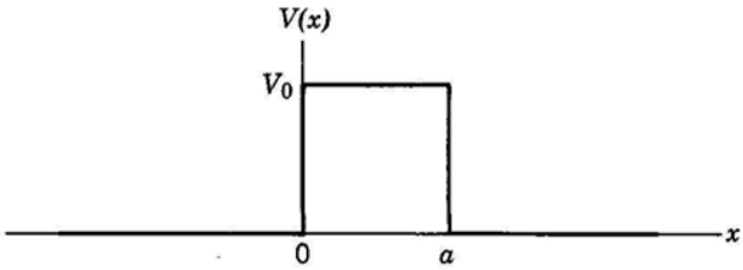

Figure 2.27 A barrier potential.

The potential can thus be written as follows

$$V(x) = \begin{cases} V_0, & 0 < x < a \\ 0, & x < 0 \; or \; x > a \end{cases} \tag{2.1}$$

In quantum mechanics the electron is represented by a wave function $\Psi(x)$ which is solution of the Schrödinger equation. The wavelength of the electron is given by the De Broglie relationship, that connects two parameters, which are separated in the classical treatment, like the mass and the wavelength.

$$\lambda_{DB} = \frac{h}{p} = \frac{h}{mv} \tag{2.2}$$

As a first theoretical approach we consider a stationary system, in which the potential of the barrier $V(x)$ is constant and the Schrödinger equation (SE) is reduced to the time-independent version.

$$\left[-\frac{\hbar^2 \partial^2}{2m\partial x^2} + V(x)\right] \Psi\,(x) = E\Psi(x) \tag{2.3}$$

The solutions of this type of equation are stationary states.

This equation breaks up into three separate equations for the three regions: left of the barrier, right of the barrier and within the barrier. Independently on the energy of the electron, the solutions of the SE on the left and right side of the barrier are given by the function of a free particle, since the potential felt by the electron is zero. Their general expression is

$$\Psi(x) = \begin{cases} Ae^{ik_I x} + Be^{-ik_I x}, & x < 0 \\ Ce^{ik_I x} + De^{-ik_I x}, & x > a \end{cases} \tag{2.4}$$

, where

$$k_I = \frac{\sqrt{2mE}}{\hbar} \tag{2.5}$$

Since we are considering a particle injection from the left side of the barrier, in the region to the right there is only the transmitted wave as there is nothing that can produce a reflection. As a consequence, $D = 0$.

In the region within the barrier, where $0 < x < a$, the form of the solutions depends on whether the energy of electron E is higher or lower than V_0.

If $E < V_0$, the general solution is

$$\Psi(x) = Fe^{-k_{II}x} + Ge^{k_{II}x} \tag{2.6}$$

, where

$$k_{II} = \frac{\sqrt{2m(V_0 - E)}}{\hbar} \tag{2.7}$$

For $E > V_0$ it is

$$\Psi(x) = Fe^{ik_{III}x} + Ge^{-ik_{III}x} \tag{2.8}$$

, where

$$k_{III} = \frac{\sqrt{2m(E - V_0)}}{\hbar} \tag{2.9}$$

We are particularly interested in the set of energy values lower than the potential energy of the barrier V_0, since those represent the states involved in the tunneling transport.

Thus, the total solution of the system for $E < V_0$ is

$$\begin{cases} \Psi_{sample}(x) = Ae^{ik_I x} + Be^{-ik_I x} \\ \Psi_{barrier}(x) = Fe^{-k_{II} x} + Ge^{k_{II} x} \\ \Psi_{tip}(x) = Ce^{ik_I x} \end{cases} \tag{2.10}$$

, considering the sample on the left side of the barrier and the tip on the right side.

The coefficients A, B, C, F and G are evaluated by matching the wave functions and their first derivatives at the edges of the barrier.

The probability current density $\boldsymbol{j}$ is defined as

$$\boldsymbol{j} = \frac{i\hbar}{2m}(\Psi\nabla\Psi^* - \Psi^*\nabla\Psi) \tag{2.11}$$

If $\Psi(x) = Ae^{ikx}$, then $\boldsymbol{j} = \frac{\hbar k}{m}|A|^2 = v|\Psi|^2$.

The ratio between the current density incident to the barrier and the transmitted current density gives the transmission coefficient T

$$T = \frac{|\Psi_{transm}|^2}{|\Psi_{inc}|^2} = \frac{|C|^2}{|A|^2} \tag{2.12}$$

, which in the limit of a strongly attenuating barrier (wide and high) becomes

$$T = \frac{16{k_I}^2{k_{II}}^2}{\left({k_I}^2 + {k_{II}}^2\right)^2} e^{-2k_{II}a} \tag{2.13}$$

The value a defines the distance between the two electrodes.

The obtained transmission coefficient can be interpreted as the probability that a particle of mass m and energy E tunnels through a potential barrier of height $V_0 > E$. It can also be observed the exponential dependence of the transmittance coefficient on the tip-sample distance a, which is the origin of the high vertical resolution of the STM measurements.

This model however presents an important limitation, since it is not suitable to describe transition phenomena between electronic states of the sample and tip. Thus, the resolution of the extended time-dependent SE (TDSE) is required for a more correct interpretation of the STM working principles.

$$i\hbar \frac{\partial \Psi(x,t)}{\partial t} = \left[-\frac{\hbar^2 \partial^2}{2m\partial x^2} + V(x,t) \right] \Psi\,(x,t) \tag{2.14}$$

This approach was firstly followed by Bardeen J. [41] and was extended later by Tersoff and Hamann [42] and Chen [43].

2.2.2. Bardeen's approach

Here below I summarize the main steps of the Bardeen's theory, highlighting the dependence of the tunneling current on the electronic states of the sample and tip. The Bardeen's approach is limited by the two assumptions that he made. He did not consider the mutual interactions between electrons during the transfer between electronic states and studied only the elastic tunneling, in which the electrons involved do not lose energy.

Firstly, the tip and the sample are considered separated. As anticipated, the time-dependent form of the SE equation is adopted.

$$sample: \qquad i\hbar \frac{\partial \Psi(x,t)}{\partial t} = \left[-\frac{\hbar^2 \partial^2}{2m\partial x^2} + U_s \right] \Psi\,(x,t) \tag{2.15}$$

$$tip: \qquad i\hbar \frac{\partial \Psi(x,t)}{\partial t} = \left[-\frac{\hbar^2 \partial^2}{2m\partial x^2} + U_t \right] \Psi\,(x,t) \tag{2.16}$$

U_s and U_t are the potentials felt by the two electrodes: sample (s) and tip (t).

The solutions Ψ of the TDSE are non-stationary states and are written as a product of a stationary space-dependent state and a time-dependent function. So, these wavefunctions depend both on time and space.

$$\Psi(x,t) = \Psi(x) e^{\frac{-iEt}{\hbar}} \tag{2.17}$$

The $\Psi(x)$ are the eigenfunctions of the TISE with eigenvalues E.

When the two electrodes are close enough the eigenfunctions of the two systems overlap and the potential of the whole system is given by the sum of the electrode potentials. The sample and tip states are indicated with μ and v, respectively (figure 2.4).

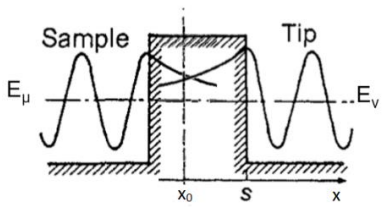

Figure 2.28 Schematic view of the tip-sample system.

$$i\hbar\frac{\partial\Psi(x,t)}{\partial t} = \left[-\frac{\hbar^2\partial^2}{2m\partial x^2} + U_t + U_s\right]\Psi\,(x,t) \tag{2.18}$$

The general solution is expressed as a linear combination of the sample and tip eigenfunctions, calculated for the unperturbed system. These are assumed to form a complete set of orthogonal wavefunctions.

$$\Psi(x,t) = \Psi_\mu(x)e^{\frac{-iE_\mu t}{\hbar}} + \sum_{v=1}^{\infty} c_v(t)\Psi_v(x)e^{\frac{-iE_v t}{\hbar}} \tag{2.19}$$

Since we are considering an electron injected from the sample side of the barrier,

$$c_v(0) = 0 \tag{2.20}$$

The condition for the elastic tunneling is $E_\mu = E_v$.

Then, by integrating the general solution and applying a first order perturbation theory, is possible to obtain the expression for the probability per unit time of the tunneling process, i.e. the electron transition from the sample to the tip state.

$$P_{\mu v}(t) = \frac{2\pi}{\hbar}|M_{\mu v}|^2\delta\left(E_\mu - E_v\right) \tag{2.21}$$

This is the so-called Fermi golden rule and the delta function δ sets the energetic condition for the elastic tunneling. $M_{\mu v}$ is the transfer matrix element and contains information about the unperturbed electronic states Ψ_μ and Ψ_v involved in the transition.

$$M_{\mu v} = \int_{x>x_0} \Psi_\mu U_t \Psi_v{}^* \tag{2.22}$$

or

$$M_{\mu v} =< \Psi_v{}^t|U_t|\Psi_\mu{}^S > \tag{2.23}$$

Finally, to evaluate the current we need to sum up, over all the sample and tip states, the transition probabilities per unit time.

$$I = 2e\sum_{\mu,v}\left(P_{\mu\to v} - P_{v\to\mu}\right) \tag{2.24}$$

Both the sample-tip and tip-sample tunneling process are considered in the summation. Occupation factors of the involved states, given by the Fermi-Dirac distribution function, are also added to the Fermi golden rule formula.

$$P_{\mu\to v}(t) = \frac{2\pi}{\hbar}|M_{\mu v}|^2\delta\left(E^s{}_\mu - E^t{}_v - eV\right)\left\{f(E^s{}_\mu)[1 - f(E^t{}_v)]\right\} \tag{2.25}$$

$$P_{v\to\mu}(t) = \frac{2\pi}{\hbar}|M_{v\mu}|^2\delta\left(E^s{}_\mu - E^t{}_v - eV\right)\left\{f(E^t{}_v)\left[1 - f(E^s{}_\mu)\right]\right\} \tag{2.26}$$

$$|M_{\mu v}|^2 = |M_{v\mu}|^2 \tag{2.27}$$

As previously explained, a bias (eV) between the Fermi energies of the electrodes is required, in order not to have an equilibrium situation of zero current. It can be easily seen that, in case of a negatively biased sample, the probability of transition from tip to sample is lower than the opposite process probability, due to a lower occupation factor.

$$P_{\mu\to v}(t) > P_{v\to\mu}(t) \tag{2.28}$$

Hence, the main contribution to the tunneling current is given by the electrons tunneling from the sample to the tip.

After several calculations and assuming that M is slowly depending on μ and v, we obtain the formula for the tunneling current over all available sample and tip states.

$$I(V, x, s) = \frac{4\pi e}{\hbar}\int_{E_F}^{E_F+eV}\left|M_{\mu v}\right|^2\rho_s(E)\,\rho_t(E - eV)dE \tag{2.29}$$

Where ρ_s and ρ_t are respectively the sample and tip density of states. The current, written in this way, can thus be seen as a convolution of the sample and tip DOS weighted by the transfer matrix M. As expected, the current varies with a negative exponential dependence on the tip-sample distance s, since

$$\left|M_{\mu v}\right|^2 \propto e^{-2k_\mu s} \propto T \tag{2.30}$$

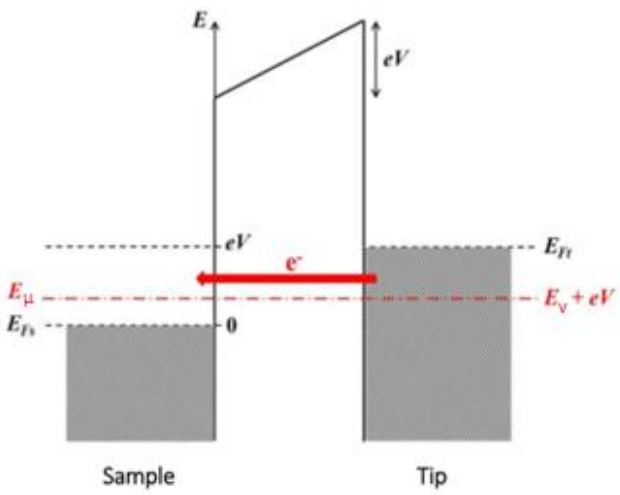

Figure 2.29 Schematic representation of the tunneling effect with a metallic sample.

In figure 2.5 the elastic tunneling in the case of positively biased metallic sample is illustrated. It can be noted that the available electronic states vary from E_F to $E_F + eV$ in the sample, which is also the interval of integration for the current.

In the case of semiconducting samples, the applied bias must be large enough so as to make the Fermi energy of the tip shift out of the energy gap of the semiconductor, both for positive and negative applied voltages. Otherwise, the tunneling process is not permitted, since there are not available states inside the gap.

Both for metallic and semiconducting samples, depending on if the applied bias is negative or positive, occupied or unoccupied sample electron states are probed, respectively, leading in some cases to completely different STM images. This fact is clearly illustrated in figure 2.6, where an example taken from literature of a semiconducting Si (111)7x7 surface, investigated by a STM, is reported [44].

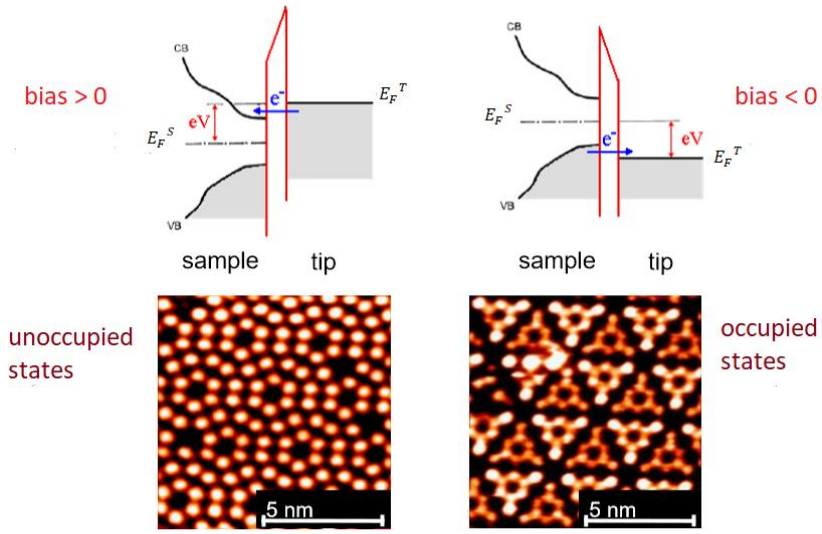

Figure 2.30 Schematic representation of the tunneling effect with a semiconducting sample (silicon surface). Different STM images are obtained if voltages with opposite sign are applied. [44]

It is thus evident that the topographic map, given by the current signal, is not a faithful reproduction of the line profile of the sample surface, since it is influenced by the sample and tip DOSs, as shown in formula (2.29).

2.2.3. Tersoff-Hamann model

In the theory developed by Bardeen an expression for the tunneling current is formulated, which is a convolution of electronic states of the tip to those of the sample. However, to access the tip states can be difficult and an improper approximation of them can lead to a wrong interpretation of STM images. For this purpose, Tersoff and Hamann proposed a model for the tip [42], with the aim of simplifying the tip properties, which can consequently be factorized out of the problem. According to this model, the STM images

measure the properties of the unperturbed sample only, rather than the properties of the joint sample-tip system.

The model considers a tip with localized potential and wave function, i.e. the tip assumes a well-defined geometrical shape. Indeed, the tip is modeled as a locally spherical potential well. As a consequence, the tip states contributing to the tunneling current are characterized by a s-type symmetry, and the contribution of states with other symmetry is neglected. Therefore, the wavefunction of the unperturbed electronic states of the tip considered in the equations (2.22) and (2.23) can be written in this form:

$$\Psi_{\nu}{}^{t}(r) \propto \frac{e^{-k_T|r-r_0|}}{k_T|r-r_0|} \tag{2.31}$$

, where r_0 is the center of the curvature of the tip and k_T is the vacuum-decay constant, which is equal to the decay constant k_S of the sample wavefunction $\Psi_{\mu}{}^{S}$, under the assumption of a small applied bias. For a correct interpretation of the model, we are considering here a three-dimensional system, as underlined by the dependence of the wavefunction on r and not on x, like we did in the previous treatment.

By substituting the new form of $\Psi_{\nu}{}^{t}(r)$ in the formula of the matrix-element $M_{\mu\nu}$ (eq. 2.22 or 2.23), which, in turn, is replaced in the formula (2.29), after several calculations, it is possible to express the tunneling current in this way

$$I \propto \int_{-\infty}^{+\infty} (f(E-eV) - f(E))\, \rho_s(E, r_0)\rho_t(E-eV)dE \tag{2.32}$$

, where $\rho_s(E, r_0)$ is the local density of states of the sample at the position r_0 of the tip apex atom.

In addition, to further simplify the interpretation of STM images, the tip density of states ρ_t is assumed to be constant. Even though the Tersoff and Hamann model is probably the most widely used approach in the interpretation of STM images, it fails in some cases. Most of the problems are related to the restriction to small applied voltages V, since, if high bias voltages are applied, the decay constants of tip and sample are no longer the same, leading to failure in the derivation of the model. Hence, this model can be trusted only for low bias voltages below 1 V.

Furthermore, it turned out that the corrugation amplitude predicted for close packed metal surfaces by the Tersoff and Hamann model was by far too small to explain the observed atomic resolution. Chen [43] attributed the cause of this to the restriction to s-like tip orbitals only, and he extended the Tersoff and Hamann model for other more directed tip-states. He included in the model orbitals pointing towards the sample, like p_z and $d_{z^2-r^2}$, where z is the coordinate perpendicular to the surface, leading in this way to higher values of the corrugation amplitude. In figure 2.7, the difference in the corrugation

amplitude detected by using d_{z^2}-wave tip orbital, rather than s-wave tip orbital for the tip modeling is illustrated by a simple picture.

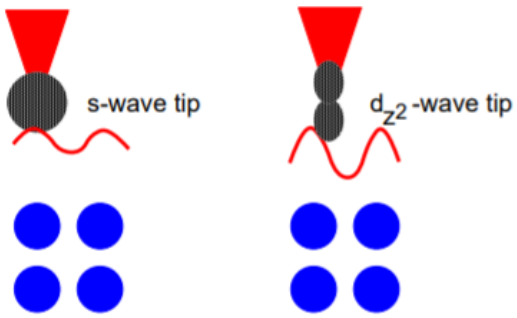

Figure 2.31 Graphical representation of the increase of the corrugation deriving from a sharper d_{z^2}-wave tip orbital as compared to an s-wave tip orbital.

2.3. Scanning tunneling spectroscopy

In the previous section, theoretical approaches for the formulation of a generic form for the tunneling current were presented. Here, starting from these results, two methods are proposed for the extraction of sample LDOS from the differential conductivity (dI/dV) map. The principles of the measurement of dI/dV by means of the Lock-in amplifier are finally explained.

2.3.1. Theory of scanning tunneling spectroscopy

By considering a one-dimensional system and applying the Wentzel-Kramers-Brillouin approximation is possible to express the transmission coefficient as follows

$$T(E,V,s) = \exp\left\{-\frac{2}{\hbar}\int_0^s \sqrt{2m[U(x)-E]}\,dx\right\} \tag{2.33}$$

, where $U(x)$ is the potential function and s is the width of the barrier. This formula can in turn be simplified in the form

$$T(E,V,s) = \exp\left\{-\frac{2s}{\hbar}\sqrt{2m(\Phi+\frac{eV}{2}-E)}\right\} \tag{2.34}$$

, if we consider a constant value of the potential in the barrier region instead of a linear dependence. The value that the potential function assumes in this case is $\Phi + \frac{eV}{2}$, where Φ is the average work function of the tip and sample (figure 2.8).

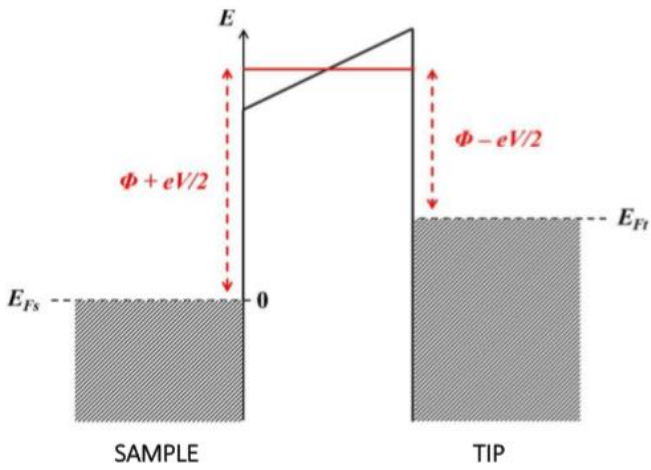

Figure 2.32 Change from a linear dependence of the potential in the barrier region to a constant value.

Now, if the transmission coefficient obtained above substitutes the square of the transfer matrix element in the formula (2.29), a new expression of the tunneling current is obtained

$$I(V,x,s) = \frac{4\pi e}{\hbar}\int_{E_F}^{E_F+eV} T(E,s,V)\rho_s(E,x)\,\rho_t(E-eV,x)dE \tag{2.35}$$

, in which the sample and tip density of states depend not only on the energy, but also on the position x over the surface. These are the so-called local density of states (LDOS).

The differential conductivity (dI/dV) is obtained by deriving the current over the potential.

$$\begin{aligned}\frac{dI(V)}{d(eV)} &= A\rho_t(0,x)\rho_s(eV,x)T(eV,s,V)\\ &\quad + A\int_0^{eV}\rho_s(E,x)\frac{d\rho_t(E-eV,x)T(E,s,V)}{d(eV)}dE\end{aligned} \tag{2.36}$$

This is the most significant quantity of STS measurement, since it is directly connected with the sample LDOS. The term A is a dimensional parameter which considers the numerical constants of the interaction area between sample and tip. The first term contains the desired value of sample LDOS, at the selected energy of the applied bias (eV). The second term instead is an integral which derives from the non-constant DOS of the tip and from the bias dependence of the transmission coefficient. In general, this term can be neglected if the applied bias is lower than ±1. Thus, in this approximation we can write

$$\frac{dI(V)}{d(eV)} \approx A\rho_t(0,x)\rho_s(eV,x)T(eV,s,V) \tag{2.37}$$

With the aim of extracting $\rho_s(eV,x)$ from the experimentally acquired dI/dV, several normalization methods have been developed in literature. Here we focus on two of them.

The first is the one proposed by Stroscio [45]. It uses the total conductivity I/V as a normalization factor. The attempt is that of eliminating the dependence of the differential conductivity on the transmission coefficient.

$$\frac{\frac{dI(V)}{d(eV)}}{\frac{I(V)}{V}} \approx \frac{\rho_t(0,x)\rho_s(eV,x)T(eV,s,V)}{\frac{1}{V}\int_0^{eV}\rho_s(E,x)\rho_t(E-eV,x)T(E,s,V)dE} \tag{2.38}$$

This method does not have a solid theoretical base; however, it has proven to work fairly well in case of semiconducting samples. This can be explained from the fact that, at increasing bias, the exponential dependence of the tunneling coefficient in dI/dV and I/V dominates and hence, dividing the dI/dV function by I/V function, the exponential dependence of the transmission coefficient is cancelled.

A second method was developed by Ukraintsev [46] and it is based on the formulation of the (2.37) in a symmetric form

$$\frac{dI(V)}{d(eV)} = A[T(eV,s,V)\rho_t(0,x)\rho_s(eV,x) + T(0,s,V)\rho_t(-eV,x)\rho_s(0,x)] \tag{2.39}$$

This is then divided by a symmetric transmission coefficient $T_{sym} = A[T(eV,s,V) + T(0,s,V)]$. Depending on the sign of the applied bias it is possible to extract separately the sample and tip LDOS at the energy level of the bias.

$$\begin{cases} for\ V > 0 \quad \frac{dI/dV}{T_{sym}} \propto \rho_s(eV) \\ for\ V < 0 \quad \frac{dI/dV}{T_{sym}} \propto \rho_t(-eV) \end{cases} \tag{2.40}$$

This technique provides information on non-occupied states of sample and tip and is less sensible to the occupied states.

In general, the main limitation in STS measurements stands on the impossibility to know a priori the tip LDOS. In the two methods proposed above it is considered constant. However, it can change during the measurements and significantly affect them. With the aim of overcoming this problem, different works have been done recently, which consider in the treatment a variable tip LDOS [47,48].

2.3.2. Differential conductivity measurement

There exist two different approaches to measure the differential conductivity (dI/dV) of a sample. It is possible to directly derivate the signal coming from the I-V converter in a selected voltage range (figure 2.9). Although this seems to be the easiest method, it is not very accurate since it is altered by the noise in the tunneling current, as explained in section 2.1.

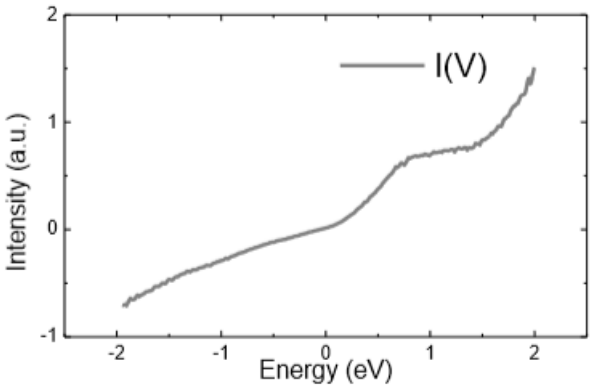

Figure 2.33 Example of a I vs V graphic.

Hence, it is preferred to use the Lock-in amplifier to extract the dI/dV from an alternated current (AC) signal. In this section I explain the base theoretical principles of this technique.

In order to perform an STS measurement, the tip is positioned on a certain point of the sample surface, a setpoint (i.e. applied bias and the current) is fixed and the feedback system is switched off so as to maintain the tip-sample distance, determined by the setpoint, constant. Finally, the dI/dV vs V behavior is plotted. The determination of the dependence of the dI/dV is performed by means of the Lock-in amplifier. This apparatus sends a small-amplitude alternated voltage, which is superimposed to a selected constant bias. The total voltage signal can be thus written in this way

$$V(t) = \tilde{V} + V_m \cos(\omega t) \tag{2.41}$$

, where $\tilde{V}$ is the constant bias, V_m the amplitude of the alternated signal and ω the modulation frequency.

Then, the Lock-in amplifier detects the current signal, with the modulation frequency ω, by means of a low-pass filter.

Now, if we consider the Taylor expansion of the current I around the voltage $\tilde{V}$ up to the first order, one can easily see that dI/dV evaluated at the applied bias $\tilde{V}$ is equal to the ratio between the amplitudes of the alternated voltage and current at the modulation frequency ω

$$I_{tunnel}(V) = I(\tilde{V} + V_m \cos(\omega t)) = I(\tilde{V}) + \frac{dI}{dV}\Big|_{V=\tilde{V}} V_m \cos(\omega t) + \cdots \tag{2.42}$$
$$\approx \tilde{I} + I_m \cos(\omega t)$$

$$\frac{dI}{dV}\Big|_{V=\tilde{V}} \cong \frac{I_m}{V_m} \tag{2.43}$$

In this way the Lock-in amplifier extracts the differential conductivity.

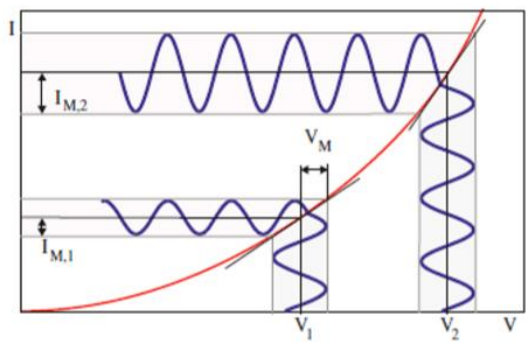

Figure 2.34 Graphical representation of the measurement of the first derivative of a hypothetical I-V curve. The amplitude of the resulting modulated current depends on the slope of the curve at the center value of the applied modulation voltage. The derivative is given by the ratio between amplitudes of the alternated current and voltage.

In figure 2.10, a hypothetical I-V curve, where two different modulated voltage are applied, centered in V_1 and V_2, is reported. The amplitude of the oscillating voltage V_m is fixed, while that of the alternated current (I_m) varies with the slope of the curve. In particular, I_m increases, if the slope of the curve increases. One can also observe that the slope of the curve is averaged around the center constant voltage in the range given by the oscillation amplitude, which is twice as much as V_m. Therefore, the energy resolution of the dI/dV signal in STS measurements is proportional to the selected amplitude V_m of the modulation voltage.

Once the dI/dV is plotted for a selected voltage range (figure 2.11), it can be normalized with a proper method, as explained in the previous section, and compared with the sample LDOS.

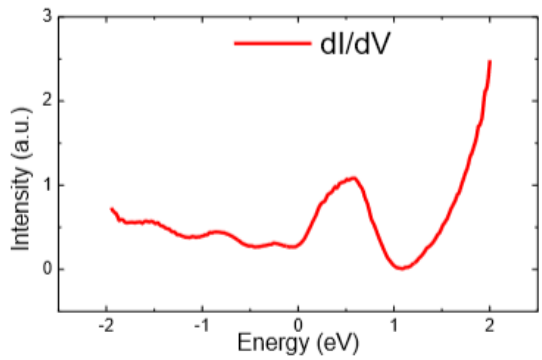

Figure 2.35 Example of a dI/dV vs V graphic.

It can be useful also to see how the differential conductivity changes over the surface. For this purpose, the surface is scanned with a constant current mode (CCM) and a fixed bias. The dI/dV, evaluated at the applied voltage, is extracted for every point of the surface and a conductivity map is obtained.

2.4. Scanning tunneling microscopy of carbon atom wires

In section 1.4, experimental works, concerning the fabrication of CAWs, have been reported and, in particular, synthesis mechanisms have been analyzed in detail. Now that the base theory of STM and STS has been treated, it can be useful to provide some examples from literature of STM images and STS measurements of sp-carbon wires on different substrates. Information on both structural and electronic properties of deposited CAWs will be given by the following analysis.

In the work done by Q. Sun and coworkers [23], they successfully achieved the formation of 1D molecular wires on an Au (111) surface, by means of the dehalogenative homocoupling reaction of terminal alkynyl bromides, as explained in section 1.4. From the interplay of STM imaging and DFT calculations, they were able to characterize the deposited structures after a mild annealing at 320 K, where organometallic C-Au-C intermediates were observed, and after an annealing at 425 K.

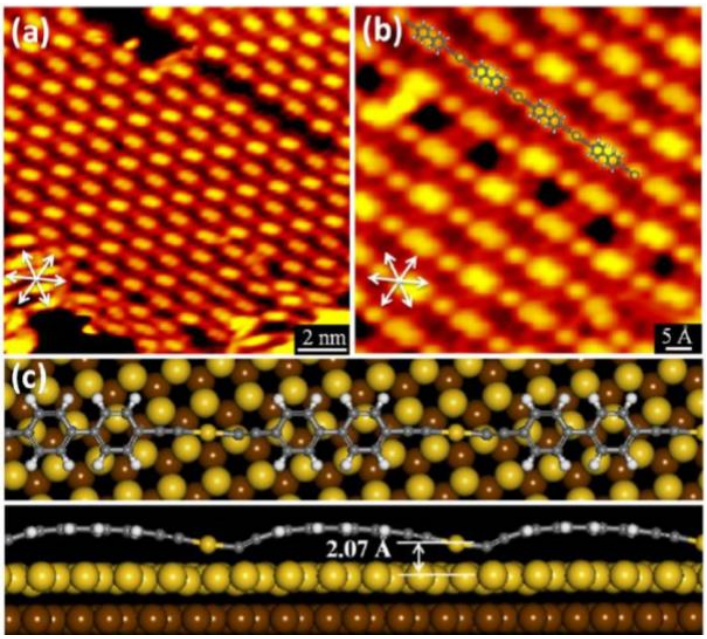

Figure 2.36 (a) Large-scale and (b) close-up STM images of the formed molecular chains after a slight annealing at 320 K. In (b) it is possible to observe the organometallic structure of the chain. (c) DFT optimized model of the C-Au-C chain on Au (111). [23]

In figure 2.12a a STM image of the linear chains after the deposition at room temperature and slight anneal at 320 K is reported. From the close-up STM image (figure 2.12b), the organometallic structure of the chain can be observed, with the protrusions of biphenyl

groups and gold atoms, which are clearly distinguishable. The detached Br atoms during the synthesis are supposed to be aligned between the chains, stabilizing them by forming hydrogen bonds. Furthermore, DFT calculations were performed with the aim of modeling the organometallic chain, as depicted in figure 2.12c. The resulting chain model was properly scaled and overlaid on the STM image (figure 2.12b), confirming a good agreement between experimental results and DFT calculations. The sample was then annealed at 425 K and the formation of acetylenic linkages in the chain resulted, as shown in figures 2.13a-c. From a close-up STM images (figure 2.13b) one can soon notice the disappearance of the dot protrusion between biphenyl groups, which implies the release of gold atoms.

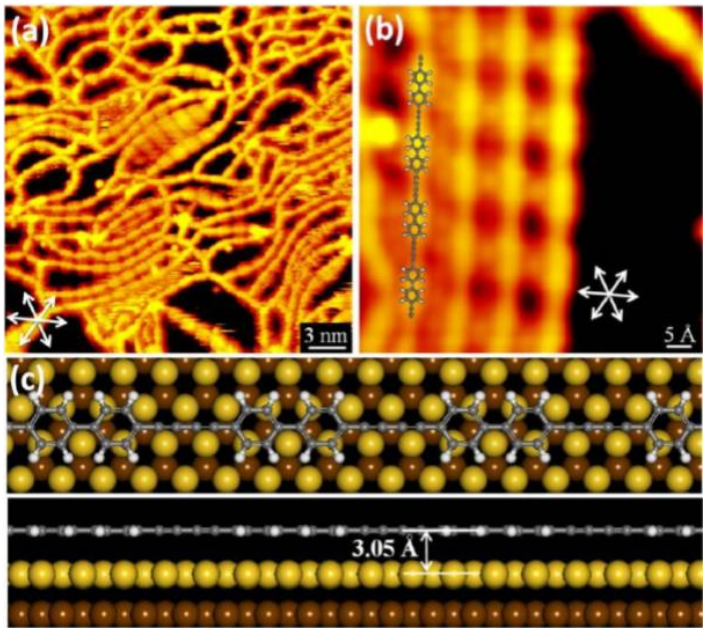

Figure 2.37 (a) Large-scale and (b) close-up STM images of the molecular chains after the an annealing at 425 K. In (b) it is possible to observe the disappearance of the gold atoms from the chain, with consequent formation acetylenic bonds. (c) DFT optimized model of the molecular chain on Au (111). [23]

Further DFT calculations were performed and the model of the linear chain was constructed, as shown in figure 2.13c. As for the organometallic chains, even in this case the overlaying of the molecular model with the STM image (figure 2.13b) confirmed the good agreement in dimensions and topography between experimental results and the theoretical model. By comparing STM images of the molecular wires after deposition (figure 2.12a) and after the annealing at 425 K (figure 2.13a), it is possible to observe a transition from an ordered disposition of the chains to a disordered one.

The same research group, headed by Q. Sun, investigated also the formation metalated carbynes on Cu (110) by dehydrogenative coupling of ethyne molecules and copper atoms [8], as anticipated in section 1.4. They adopted the same approach used in the previous work, which consists in characterizing the products by STM combined with DFT calculations.

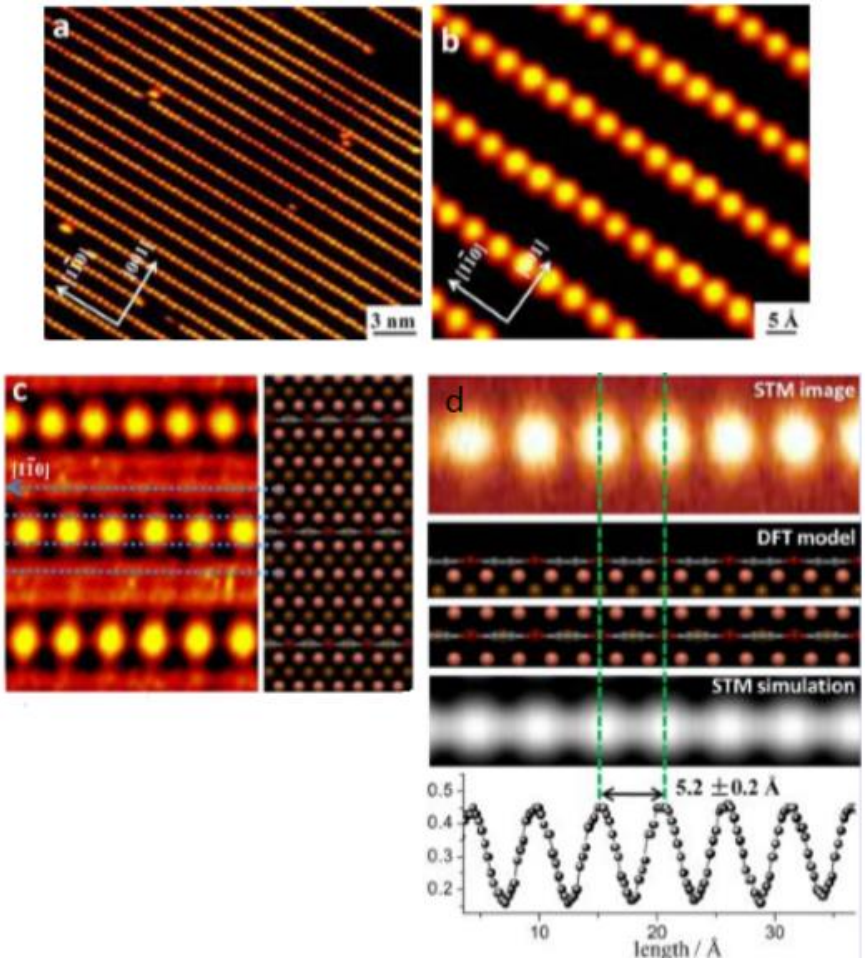

Figure 2.38 (a) Large-scale and (b) close-up STM images showing formed metaated carbynes on the Cu (110) surface. (c) High-resolution STM image compared with the theoretically predicted structure. Cu rows along the $[1\bar{1}0]$ *direction are indicated by blue dashed lines. (d) Equally-scaled STM image, DFT model, and simulated STM image with the line profile of a metalated carbyne on Cu (110). [8]*

In figure 2.14a the STM image of the chains after deposition is reported, where it is possible to observe the alignment of the chains along the close-packed $[1\bar{1}0]$ direction of the copper substrate. By looking at the close-up STM image (figure 2.14b), one can notice that carbynes are characterized by periodic protrusion. X-ray photoelectron spectroscopy revealed the presence of both C-C and Cu-C bonds inside the chains. For this reason, they attributed to metalated carbynes an organometallic chain structure of the type $[\text{-Cu-C-C-}]_n$. By comparing the theoretically predicted structure and the STM image of metalated carbynes (figure 2.14c) they discovered that the chains prefer to be located at bridge sites of copper rows along the $[1\bar{1}0]$ direction. They finally determined that the periodic protrusions correspond to the incorporated copper atoms. This result was achieved by means of a comparison of the equally scaled STM image, DFT-optimized model, and STM simulation a line profile of a metalated carbyne, as reported in figure 2.14d.

Similar experiments were conducted by Chen-Hui Shu et al. [24] about the on-surface synthesis of poly (p-phenylene ethynylene) (PPE) molecular wire via homocoupling of the trichloromethyl groups on Cu (111) surface. The reaction pathway has been already

discussed in section 1.4. Here, instead, we report some relevant analyses on the structure and the electronic state of the molecular wire investigated by STM and STS measurements/DFT calculations, respectively.

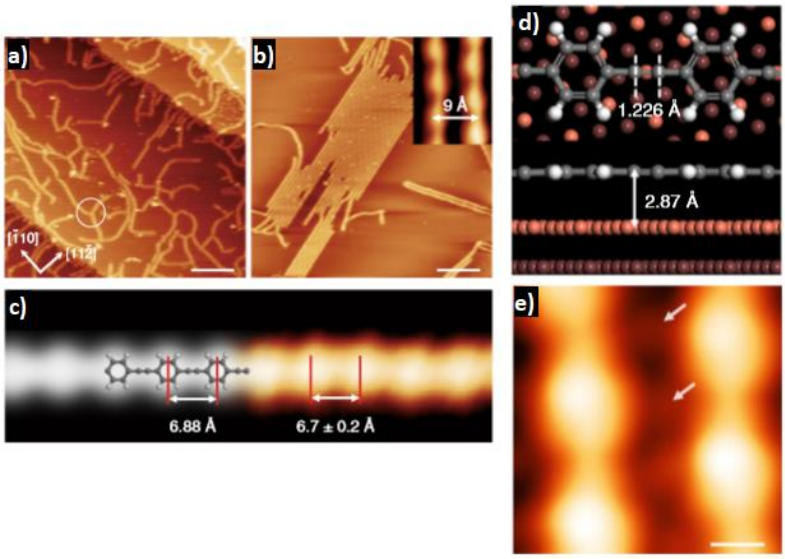

Figure 2.39 STM images of formed nanowires after deposition at 300 K (a) and after the annealing at 358 K (b). Scale bar (a,b): 10 nm. (c) Close-up STM image of an individual nanowire (right) and Simulate STM image (left). (d) DFT-optimized model of a PPE nanowire on Cu (111). (e) Close-up STM image of an ordered domain of nanowire (b), with Cl atoms between the chains. Scale bar: 300 pm. [24]

In figure 2.15a a large-scale STM image shows the nanowires after the deposition. A further cooling to 4.7 K was performed to better characterize the linear structures. As one can see, the wires assume a spaghetti-like conformation on the copper substrate and most of them have one of the ends attached to a Cu step edge. Also, branched structures can be observed, as marked by the white circle, which have been attributed by means of DFT calculation to a coordination structure formed by three nanowires attached to a Cu atom at the joint point. In the STM image in figure 2.15b effects of the annealing at 358 K are clearly visible. The nanowires align each other along two different directions, giving rise to ordered domains. The extended wire length was supposed to be due to the coupling of nanowires with termini attached to step edges or Cu adatoms. From close-up STM images (figure 2.15c, 2.15e and inset in 2.15b) periodic protrusions on nanowires can be observed and their measured periodicity agrees with the simulated STM image (figure 2.15c) of the chain. These measurements also suggested that the protrusions and the linkers in the STM images of nanowires can be assigned to phenylene and ethynylene, respectively. Furthermore, DFT calculations of the molecular wire on the copper substrate (figure 2.15d) were performed, confirming the agreement between theoretical and experimental measurements. Figure 2.15e is the high-resolution STM image of the nanowires. In between the protrusions corresponding to phenylenes groups it is possible to observe an enhanced contrast, which is attributed to the large electron localization in the acetylenic bond. The dot-like protrusions observed in between the chains (indicated by a white arrow in figure 2.15e) were believed to be the Cl atoms detached from the

precursors during the coupling reaction. DFT calculations demonstrated that molecular wires are stabilized by intermolecular Cl-H bonds.

STS spectra were acquired at different positions along the nanowire, as shown in figure 2.16a. Their similarity confirmed the predicted delocalization of the electronic state over the nanowire.

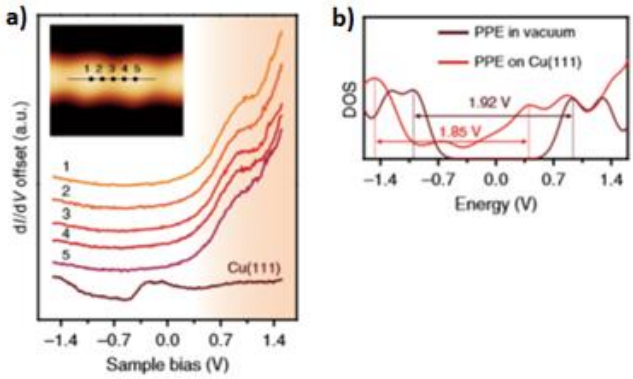

Figure 2.40 (a) dI/dV spectra measured at different sites along the nanowire and on Cu (111). (b) Calculated desity of states of PPE nanowire on Cu (111) and in vacuum. [24]

In figure 2.16b the calculated densities of state of the molecular wire in vacuum and on Cu (111) are reported, indicating a smaller band gap for the structure in vacuum, probably related to the hybridization of the electronic state of the wire with that of the underlying copper substrate.

2.5. Thesis aim and objective

In the light of the experimental and theoretical works illustrated in the previous section and in the first chapter of this thesis, in the following I now define what goals and specific objectives of this work are going to be. The experimental results discussed in this thesis concern the investigation and characterization on sp-carbon-based wires, deposited by on-surface synthesis on an Au (111) substrate. This will be achieved by means of different powerful analysis tools, such as STM and Raman spectroscopy. In particular, I will try to unveil morphological, structural, electronic and vibrational properties of the deposited sample. Finally, some preliminary studies on the chemical characterization by Auger spectroscopy will be reported. In chapter 3 the materials and methods employed in my investigations will be introduced, while in chapter 4 a detailed analysis and discussion of the results will be reported. Here below I outline the main objectives of this thesis work.

- Deposition of sp-carbon precursors on an Au (111) surface by thermal evaporation.
- A detailed investigation on the effects of increasing temperatures on morphological and structural properties of formed CAWs through the analysis of large-scale and close-up STM images.

- Characterization of the evolution of electronic properties along sp-carbon chains and detection of differences in the conductive behavior between chain domains and the substrate by means of STS measurements and differential conductivity maps.
- Study of the vibrational structure of deposited chains annealed at different temperatures by the analysis of ex-situ Raman spectra and the comparison with DFT-simulated spectra.
- Preliminary experiments: complementary information on the chemical composition of the sample can be provided by Auger spectroscopy measurements.

Chapter 3

Materials and methods

In previous chapters, firstly the wide world of the research on carbynes and secondly the huge potentialities of the scientific investigation by means of the scanning tunneling microscopy have been introduced. Now my intent is to present in the following chapter the materials and methods employed in the fabrication of samples and the techniques and procedures used for their characterization. As described in the section 2.5, I investigated by STM and Raman spectroscopy molecular sp-carbon wires, deposited by on-surface synthesis on the Au (111) surface. Techniques to produce nanowires, based on the mechanism of the on-surface synthesis, have been introduced and discussed in chapter 1.4, and the active role played by the substrate has emerged as a common feature in all the cited works. The chemical and physical properties of the substrate and its surface atomic arrangement are fundamental in determining the interactions with the deposited precursor and in orientating the chain growth. Hence, in order to better understand the achieved experimental results, that will be reported in chapter 4, a general overview on both the Au (111) surface and the molecular precursor is given in the following. Furthermore, before introducing the employed materials, in the first section of this chapter I describe the structure and features of the experimental apparatus. Concluding, the procedure for the deposition of molecular precursors is treated in detail.

3.1. Experimental apparatus

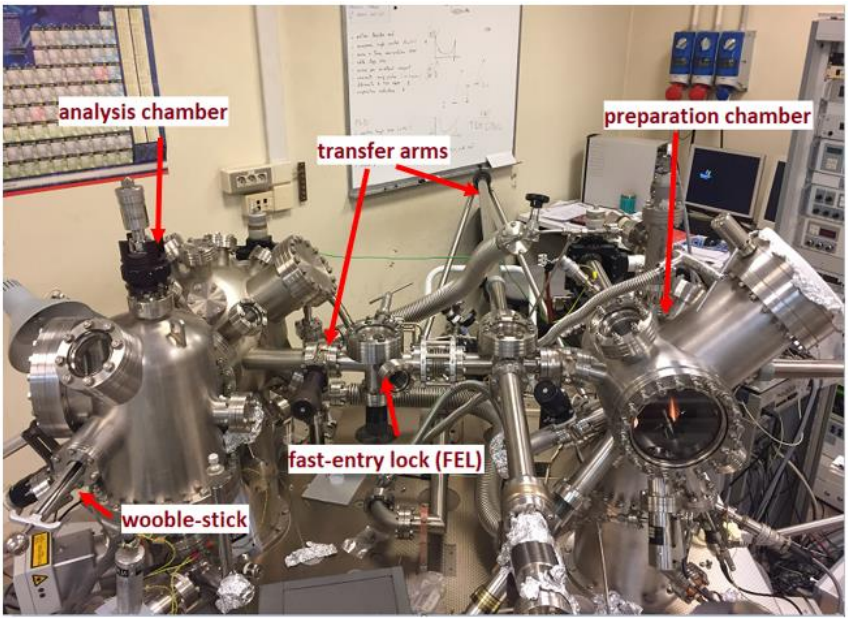

Figure 3.41 Ultra-high vacuum apparatus.

All the analyses and procedures adopted in my experiments were carried out in-situ, inside a system of three interconnected ultra-high vacuum (UHV) chambers: the

preparation chamber, the analysis chamber and one chamber dedicated to the pulsed laser depositions (PLD). A photo of the whole experimental apparatus (excluding the PLD chamber) is shown in figure 3.1.

I did not use the PLD chamber in my experiments, so its structure and components are not going to be treated in the following. I will, instead, analyze separately the preparation and analysis chamber, used for the production and the STM investigation of the samples, respectively.

The pressure inside the system reaches values of the order of $10^{-10} mbar$ thanks to the contribution of two different types of vacuum pumps: turbo molecular pumps and ion pumps. Each chamber is pumped by its own vacuum system. Moreover, titanium sublimation pumps (TSP) inside both the analysis and preparation chamber are periodically activated so as surrounding chamber walls become coated with a film of clean titanium, which reacts with residual gases, forming stable products. TSPs, together with ion pumps, are employed for the maintenance of the ultra-high vacuum regime, once turbo molecular pumps are switched off. The decoupling of chamber vacuum is accomplished by means of gate valves, properly located along the tubes connecting the chambers and it becomes necessary when, for instance, the pressure in the preparation chamber increases considerably, due to the specific sample treatment.

The transfer of samples among and inside the chambers is achieved by the aid of a system of transfer rods and manipulators. A so-called 'wooble-stick' is implemented close to the STM apparatus and allows the operator to insert the sample in the specific holder for the STM analyses.

The procedure for the transfer of a sample from outside to inside the UHV system is based on a mechanism called fast-entry lock (FEL), shown in figure 3.2. The sample is inserted in a small chamber which is pumped by its own vacuum system and can be decoupled from the rest of the apparatus by the closing of a gate valve. Once the pressure in the FEL has decreased enough, the valve is opened, and the small chamber is putted in communication with the rest of the apparatus. For the extraction of the sample from the UHV apparatus one must operate in the reverse order.

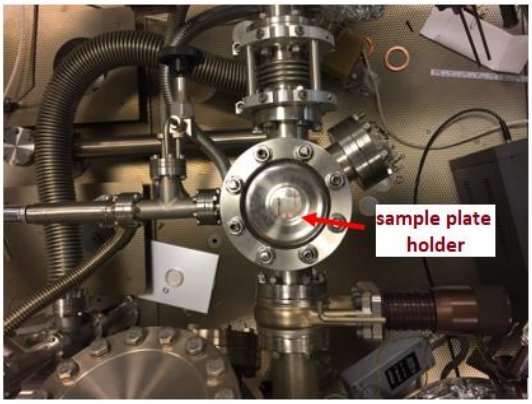

Figure 3.42 The FEL chamber.

The preparation chamber is equipped with all the systems needed for the sample preparation. In figure 3.3a it is possible to observe the various components mounted in the preparation chamber.

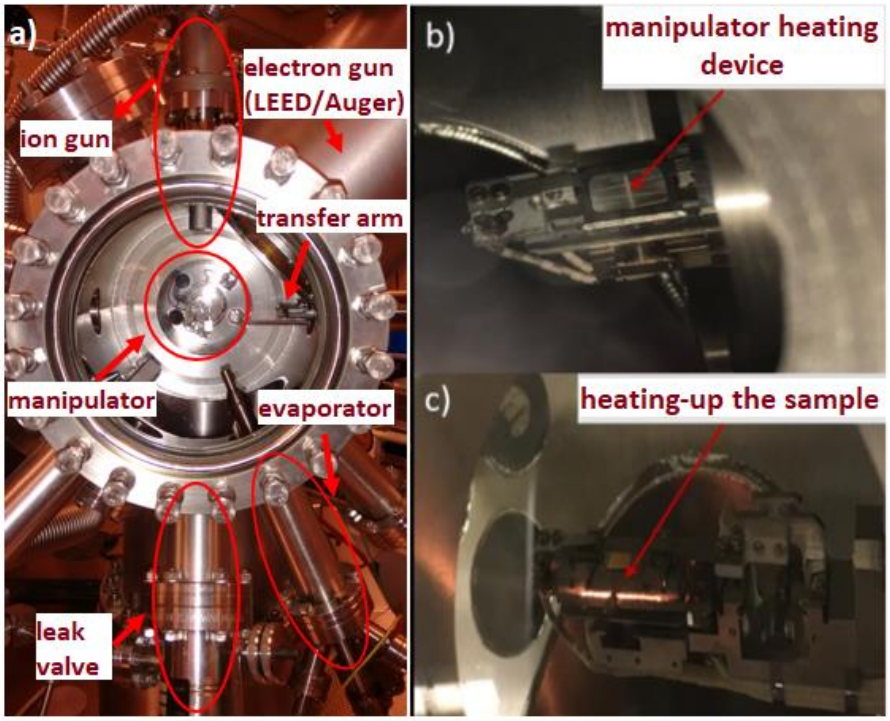

Figure 3.43 (a) Preparation chamber. Main devices and components are indicated. (b) The heating mechanism mounted under the sample holder on the manipulator. (c) An annealing treatment of the sample.

An ion gun (figure 3.3a), located on the top of the chamber, is employed for the cleaning of the sample surface by ion sputtering. For this purpose, Ar atoms are let to enter the chamber with high precision through a leak valve until the pressure in the chamber reaches a value in the range $3-4\ \times 10^{-6} mbar$. The Ar flux is then ionized by electrons emitted by a hot filament and it is subsequently accelerated towards the substrate by an applied voltage. After the sputtering, which usually takes around 5-10 minutes, a further annealing of the sample surface can be required, in order to relax the stresses caused by the Ar^{+} bombardment.

Thermal treatments are accomplished by radiative heating from a hot filament, which is incorporated under the sample holder on the manipulator, as illustrated in figures 3.3b-c. With the aim of reaching higher temperatures, a voltage can be applied to extract electrons from the filament and accelerate them toward the sample (electron-beam heating). Typical operating parameters of current and voltage for the surface annealing by e-beam heating are $I = 1.5 - 2.0\ A$ and $V = -450\ V$, respectively. The temperature measured by the thermocouple in the proximity of the sample reached values over $700K$. Annealing cycles were also performed on the sample with deposited nanowires, in order to evaluate the effects of the temperature on the morphological and structural properties. In that case no external voltage was applied and the current was decreased in the range of $1 - 1.25\ A$, so as to make the temperature go down to values in the range

of $373 - 423\,K$, since temperatures over $500\,K$ could have caused the molecules degradation.

The deposition technique consists in thermal evaporating the precursor which then deposits on the Au (111) surface. The evaporation is achieved by means of a specific crucible called 'resistive heating sample plate', that is shown in figure 3.4.

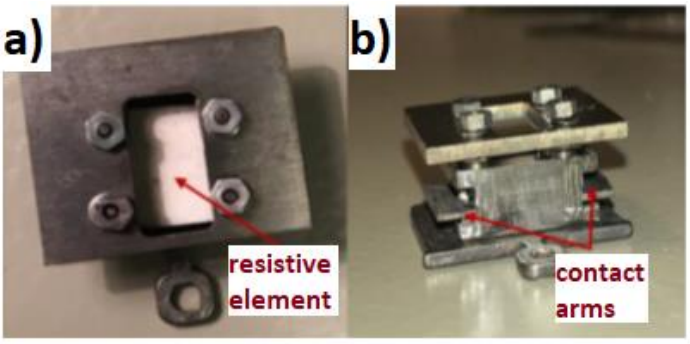

Figure 3.44 The resistive element (a) and the contact arms (b) of the resistive heating sample plate.

The support of the crucible is equipped with two contact pins, which must be put in contact with the metallic arms of the power supply, located on the manipulator. In this way, the current can pass in the resistive element placed under the crucible and heat up the molecular precursor which is thus evaporated. The procedure for the preparation of the samples will be reported in detail in the section 3.4.

The preparation chamber is also equipped with an electron gun, as shown in figure 3.3a, suitable for Auger spectroscopy and low-energy electron diffraction (LEED) measurements. However, I used it only for preliminary experiments of Auger measurements (see appendix). I selected energy of the electron beam in the range $1500 - 3000\,eV$ and a beam current of $10 - 15\,\mu A$.

Once the sample has been prepared and cooled down to room temperature, it is transferred to the analysis chamber for subsequent investigations by means of STM imaging and STS measurements. As previously explained, it is taken out from the manipulator and inserted in the sample holder on the STM stage by using the wooble-stick. In figure 3.5a it is possible to observe the upside-down configuration of the STM apparatus. The tip is indeed mounted on a piezoelectric actuator (the scanner), pointing towards the overlying sample. The stage can be mechanically decoupled from the rest of the chamber by means of an unlock mechanism (figure 3.5b) which leaves the stage suspended by four springs. Also, a magnetic eddy current damping system is implemented, based on electromagnetic forces generated by the movement of a conductor trough a stationary magnetic field.

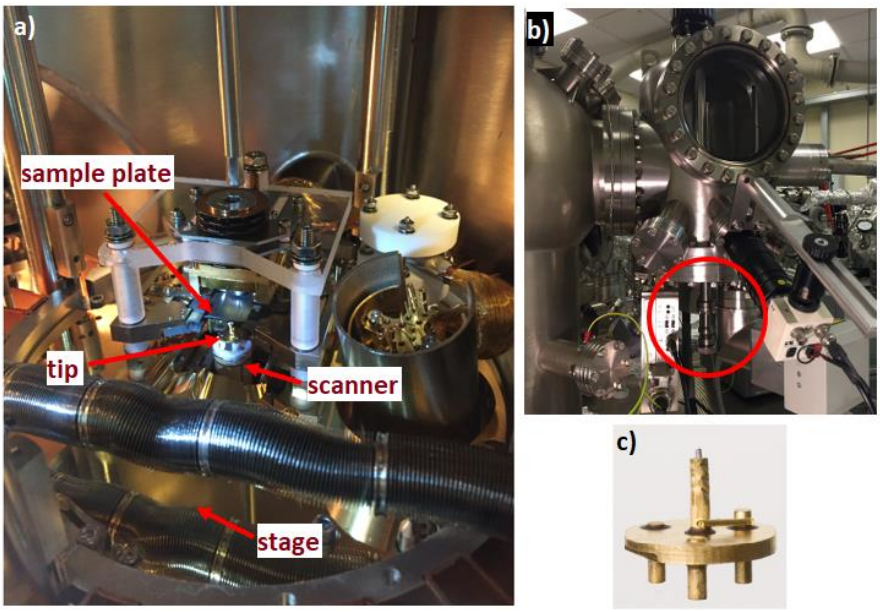

Figure 3.45 (a) STM stage in the analysis chamber. The tip approaches the sample plate from the bottom side. (b) The unlock mechanism of the stage. (c) STM tip.

As explained in section 2.3.2, in order to extract the STS signal, an alternated voltage is superimposed to a constant bias. Then, the dI/dV value is calculated in a range of applied bias, by means of the Lock-in amplifier. For this purpose, the frequency of the modulated signal was set to $6\ kHz$, while its amplitude to $30\ mV$.

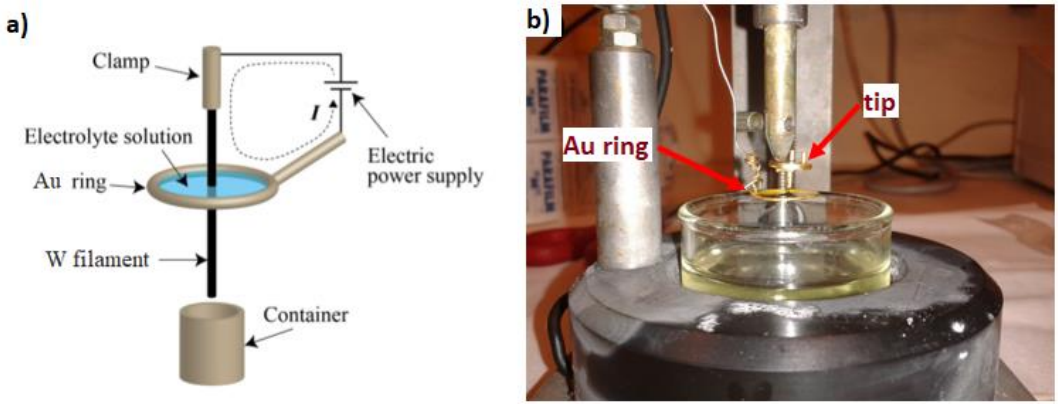

Figure 3.46 Schematic representation (a) and photo (b) of the setup to fabricate STM tips by electrochemical etching.

Concluding the section about ultra-high vacuum technologies, the procedure for the preparation of tungsten STM tips (figure 3.5c) is described. In section 2.1, I discussed the importance of the tip sharpness to achieve high resolution in STM images and I also mentioned that is not so simple to obtain a one atom-terminated tip. For the tip fabrication I adopted an electrochemical method, which consists in the formation of an electrochemical cell, with an Au ring as cathode, the W filament as anode and a solution of NaOH as liquid electrolyte. By applying an external voltage, the W filament, which was previously clamped to an STM tip holder, was electrochemically etched. Once the newly-

prepared tip was inserted in the vacuum apparatus, I annealed it, in order to allow the gas desorption. In figure 3.6 the image of the apparatus for the electrochemical etching and its schematic representation are shown.

Raman measurements were carried out ex-situ. For the spectra acquisition mainly two lines of an Argon laser are employed: the green (λ=514 nm) and the blue one (λ=457 nm). In my experiments I used only the green light. An optics technology focuses the laser on the sample surface. Then, the light scattered from the sample is caught by a detector, which transmits the information directly to a software in the computer, which elaborates the data and plots the spectrum. For the treatment of the Raman spectra data I used the software Origin.

3.2. Substrate for on-surface synthesis: Au (111)

Recently, deposition techniques based on the mechanism of on-surface synthesis have emerged as a powerful method to produce nanostructures on different substrates. Surface properties have turned out to be largely influencing several parameters in the synthesis process, from the nature of the interaction with the deposited molecules to their disposition on the substrate. In this context, the Au (111) surface has been widely used [23,49,50,51], since it is mostly inert and provides an ordered surface pattern for the preferential nucleation of aligned molecules and nanostructures. For this reason, it was decided to employ it as the substrate in my samples. Hence, a thin (200 nm) Au (111) layer, grown on mica, was welded on a Tantalum support, equipped with an eyelet, in order to be able to manage it inside the UHV apparatus by means of transfer arms, manipulators and the wooble stick. The sample is illustrated in the figure 3.7.

Figure 3.47 Gold substrate soldered on the tantalum plate.

The surface reconstruction of Au (111) has been largely investigated in literature by means of STM observations [52,53] and theoretical studies [54].

Gold is a metal with a face-centered cubic (fcc) crystal lattice. Due to anisotropic compressions along the <110> direction, the surface layer undergoes an atomic reconstruction. Displacements from the bulk truncated structure occur both in the (111) plane and along the <111> direction, as shown in figure 3.8, where the $(23 \times \sqrt{3})$

reconstruction is reported. As one can observe, along the <1$\bar{1}$0> direction more atoms then the available bulk lattice sites are accommodated. In particular, 23 Au atoms are arranged over 22 sites. Simultaneously, some Au atoms are displaced from their fcc position to an hcp position, along the <11$\bar{2}$> direction. The two above described in-plane displacements push some atoms to occupy bridge sites between the stacking positions of the underlying atomic layer, which are consequently lifted up. This phenomenon arises in the formation of couples of ridges that align along the <11$\bar{2}$> direction, which represent the transition from the fcc to the hcp symmetry or vice versa, as illustrated in the top part of the figure 3.8.

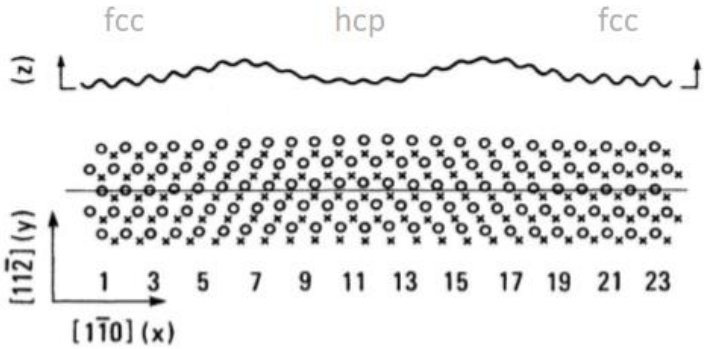

Figure 3.48 Schematic representation of the Au (111) surface. The atoms in the reconstructed top layer and in the second layer are indicated by the circles and crosses, respectively. [53]

As a result of the surface stress relaxation, the parallel corrugation lines of the Au surface create correlated periodic bending, as shown in figure 3.9a, forming the so-called herringbone pattern. The termination of the reconstruction lines can occur both by well-ordered, U-shaped connections of adjacent lines and by a more complicated link between two couples of corrugation lines, as highlighted in figure 3.9b by red circles. Terminations, together with elbows (black circles in figure 3.9b) are considered defects that alter the regular herringbone pattern and may act as preferential adsorption sites for adsorbed atoms or molecules.

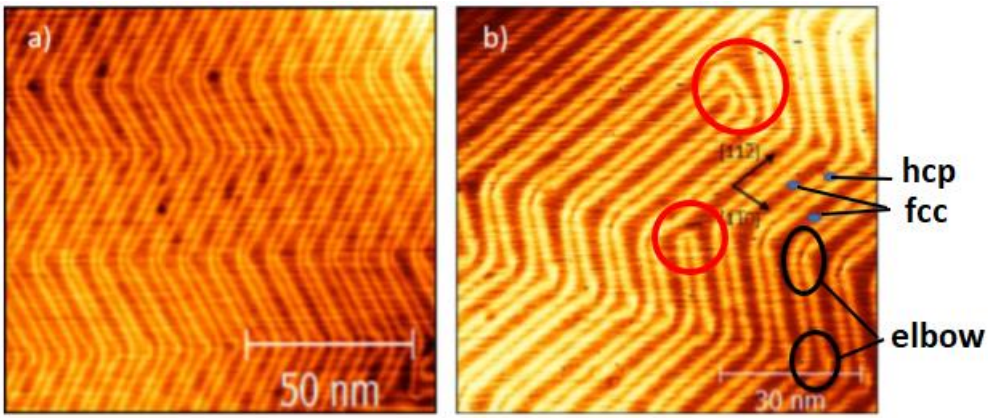

Figure 3.49 STM images of the cleaned Au (111) surface. (a) The typical periodic bending of the herringbone pattern. Acquisition setpoint (0.5 V, 0.5 nA). (b) Terminations (red circles) and elbows (black circles) of the corrugation lines. Fcc and hcp regions are indicated. Acquisition setpoint (-0.4 V, 0.6 nA).

The electronic structure of the Au (111) is characterized by the presence of a surface state, called Shockley state, which is located below the Fermi level. This is populated by electrons confined near the solid/vacuum interface. The origins of the electronic confinement are the surface potential barrier and the projected band gap of the bulk states, which allow electrons to behave like a 2D nearly-free electron gas. In the STS measurement on Au (111) surface, reported in figure 3.10, one can soon notice the presence of the Shockley state, revealed by the peak in the differential conductivity at -0.5 eV with respect to the Fermi energy (Ø eV). [55,56]

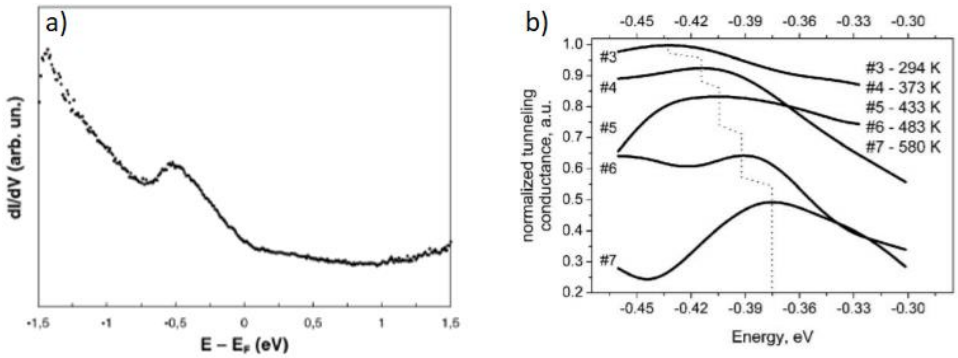

Figure 3.50 (a) The Shockley peak at -0.5 eV in the STS spectrum of the Au (111) surface. [55] (b) Shift of the Shockley peak towards the Fermi level for increasing temperatures. [57]

The influence of temperature on energy position of the Shockley peak has been investigated in literature, reporting a progressive shift towards the Fermi level for increasing temperature [57].

3.3. Molecular precursor for sp-carbon linear chains

As explained in section 1.4, in order to produce by on-surface synthesis sp-carbon-based nanostructures, containing acetylenic linkages, molecular precursors of different nature can be employed. Depending on the mechanism of the homocoupling reaction, terminal groups of precursors are properly tailored. For instance, I discussed the dehalogenative and dehydrogenative homocoupling reactions of terminal alkynyl halides and terminal alkynes, respectively [8,23]. In both the above-mentioned reaction mechanisms, the choice of the precursor is limited to those which contain an acetylenic linkage in the structure. However, a method that overcomes this limitation, has been proposed recently, and consists in the in-situ formation of the C≡C bond via homocoupling of trichloromethyl groups [24].

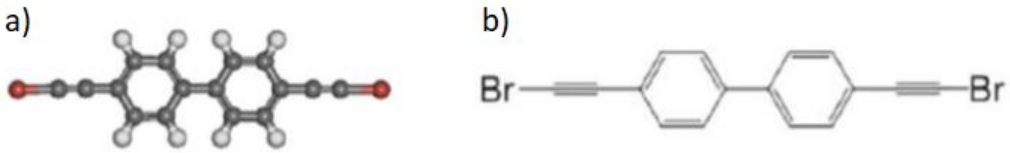

Figure 3.51 The molecular model (a) and the structure formula (b) of the molecular precursor. [23]

The molecular precursor that I used in my experiments is the one designed by Q. Sun and coworkers in ref 23. The molecule is formed by a biphenyl group with two terminal alkynyl bromide groups, which give rise to the on-surface dehalogenative homocoupling reaction with other precursor molecules, through the elimination of bromine as byproduct. The resulting nanostructure is a molecular chain, composed by biphenyl groups connected by acetylenic linkages. As reported in section 1.4, the formation of the C-Au-C organometallic intermediate was observed after the deposition and a mild annealing at 320 K and gold atoms were released from the chains after an annealing at 425 K. The IUPAC name of the precursor is 4,4'-di(bromoethynyl)1,1'-biphenyl, which for simplicity will be abbreviated with the acronym bBEBP. In figure 3.11, both the molecular model and the schematic illustration of the bBEBP are shown.

In section 3.1, I introduced the resistive heating sample plate used for the thermal evaporation of the molecular precursor. It is illustrated in figure 3.12, with the crucible containing bBEBP molecules in the form of a yellow powder.

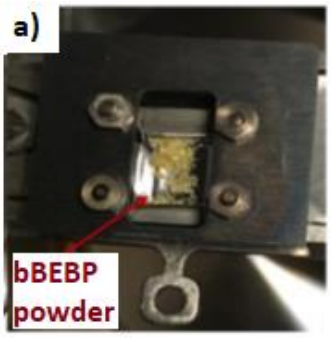

Figure 3.52 The crucible containing the bBEBP powder.

3.4. Procedure for on-surface synthesis in ultra-high vacuum

Once the experimental apparatus and the employed materials have been introduced, it is possible now to discuss in detail the procedure adopted for the deposition of bBEBP molecules on the Au (111) substrate inside the preparation chamber. As a preliminary operation, I cleaned the Au (111) surface by performing several cycles of 1.5 KeV Ar^+ sputtering to get rid of the contaminations, followed by annealing cycles to relax the surface layer and favor the formation of wide atomically flat terraces separated by monoatomic steps. Degassing of the bBEBP powder was then accomplished by cycles of annealing to free the powder from impurities.

Once both the substrate and the precursor had been cleaned, I got ready for the thermal evaporation of bBEBP on Au (111). For this purpose, I put the sample on the transfer arm and the resistive heating sample plate with the bBEBP powder on the manipulator, which is electrically connected to a power supply (figure 3.13).

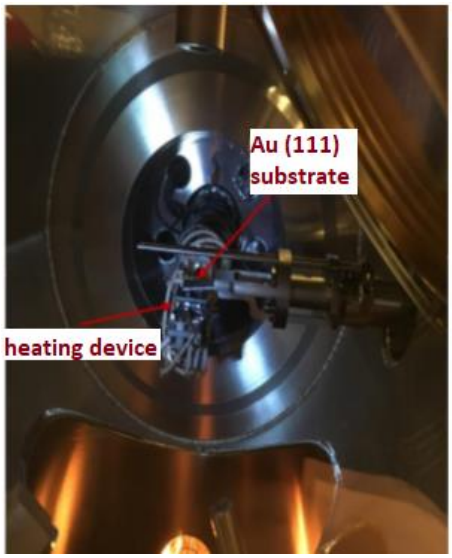

Figure 3.53 Thermal evaporation of bEBP on the Au (111) substrate. The sample is placed over the crucible, facing down.

I then heated up around 328 K, which is the temperature indicated by Q. Sun et al. [23] for the evaporation of the bBEBP precursor, and I imposed the power supply at around 0.6 W. In particular, I set the current $I = 0.2 - 0.3\ A$ and the voltage $V = 2.2 - 2.3\ V$. The power needed to reach a desired temperature in the crucible can be found in experimental temperature reference curves. In the moment that I noticed a slight variation in the chamber pressure, which indicated the occurring evaporation of the molecule, I transferred the sample over the crucible, as shown in figure 3.13, and I held it there for an enough time to allow the deposition. Several attempts were carried out, in order to unveil optimal conditions of pressure, voltage, current and duration for a successful deposition.

After having deposited, the sample was transferred to the analysis chamber for STM characterization of as-deposited structures. In the case I observed the desired nanowires, I proceeded with the analyses. In the other case, I transferred the sample back to the preparation chamber and repeated the entire procedure, starting from the cleaning of the sample surface.

Chapter 4

Experimental results

Finally, after having stated the aim of this thesis work in section 2.5 and having introduced in chapter 3 the materials and the analysis tools employed in my experiments, I dedicate the whole chapter 4 to the presentation and discussion of the achieved results. In the following, firstly, the STM characterization of the deposited sp-carbon linear chains is reported, focusing mainly on their morphological and structural properties at increasing temperature. Secondly, explorative STS measurements and differential conductivity (dI/dV) maps are analyzed to provide valuable information on the electronic properties. Finally, ex-situ Raman spectroscopy measurements are shown and compared with DFT-calculated Raman spectra, provided by A. Milani and his group, in order to reveal the vibrational structure of the deposited nanowires.

4.1. Scanning tunneling microscopy and spectroscopy of carbon atom wires

I successfully synthetized sp-carbon atom wires on an Au (111) surface via the homocoupling reaction of molecular precursors, known as bBEBP, by thermal evaporation under ultra-high vacuum conditions. The deposited linear molecule is composed by a biphenyl group, which is terminated by two alkynyl bromide groups. Its structure was introduced in section 3.3.

After having deposited the sp-carbon structures, I investigated the sample by means of STM and STS measurements. Once the sample had been largely characterized, I transferred it back to the preparation chamber for further annealing cycles, with the purpose of exploring the effects of the increasing temperature on the sample properties. Hence, I analyzed the same sample, immediately after the deposition ('as-deposited') and following annealing cycles at 377 K, 388 K, 400 K and 430 K.

As far as morphology and structural properties of the sp-carbon chains are concerned, I considered the work done by Q. Sun et al. [23] as the main reference, for the comparison of the achieved results. The article has been reported in detail in the section 2.4.

Electronic properties of the deposited sample are finally studied through the analysis of differential conductivity maps (dI/dV) and STS measurements.

4.1.1. Morphological properties

In the work done by Q. Sun and coworkers, CAWs were investigated by STM analyses after the deposition (slightly annealed at 320 K) and an annealing at 425 K. They observed that as-deposited chains were characterized by an organometallic structure, with atoms of the Au (111) surface between biphenyl groups. After the annealing at 425 K, the

disappearance of the Au atoms from the chain structure and the formation of acetylenic bonds connecting biphenyl groups was noted. Furthermore, chains assumed a disordered disposition over the substrate, as the effect of the increased temperature.

My intent was to provide an in-depth understanding of the behavior of the chains, both packed in domains and as isolated species, with the progressive increase of the temperature. In the following I thus illustrate STM images of the deposited CAWs on the Au (111) substrate.

In figure 4.1, it is possible to observe STM images of the as-deposited molecular chains, identified by brighter domains (see labels in figure 4.1a). By analyzing the figure 4.1a, one can soon notice that the deposited linear structures tend to follow the herringbone pattern of the underlying Au (111) surface, forming ordered close-packed domains in which they align each other.

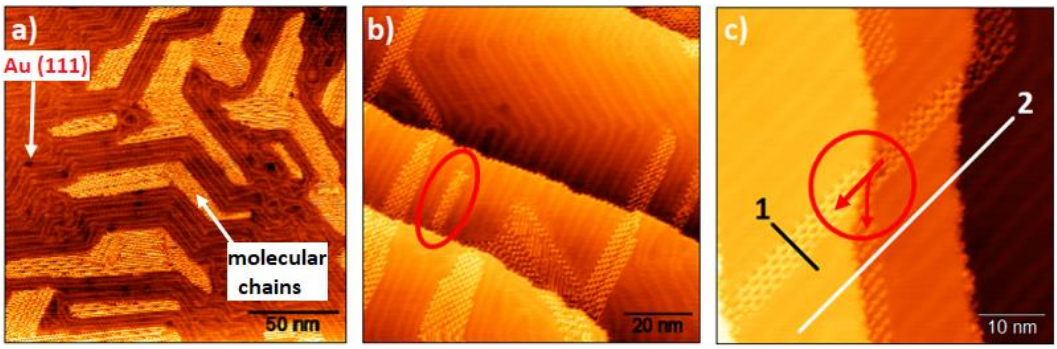

Figure 4.54 STM images of the as-deposited chains. (a) (200x200 nm) Well-oriented domains follow the herringbone pattern of the Au (111) surface. Set point (-1 V, 0.3 nA). (b) (100x100 nm) Well-oriented array of chain attached to an Au (111) step. Set point (-1 V, 0.3 nA). (c) (50x50 nm) Aligned chains cross the step or align along it. Set point (-1 V, 0.3 nA).

In the large-scale and close-up STM images shown in figure 4.1b and 4.1c, respectively, it must be observed that linear chains behave in different ways when they encounter a step of the Au (111) substrate: they are interrupted, they cross the step, or they deviate from their straight path, aligning along the direction of the step. The three cases are highlighted by the red circle in figures 4.1b and two red arrows in figure 4.1c. To be more precise, the steps of the substrate should be considered as nucleation sites for the growing CAWs, rather than a stopping line, since they possess a higher energy compared to atoms in the bulk, which favors the attachment of a chain end or the chain alignment with it. Hence, we can conclude that the chain growth is guided by both the herringbone pattern and the atomic steps of the gold substrate. Measurements over the height profiles of the line 1 and line 2 in figure 4.1c revealed that both the ordered chain domains and the gold flat terraces are one-atom thick, since heights are comparable with the C and Au atomic diameters, respectively. In particular, the height of chain arrays is 1.36 Å, while that of Au (111) steps is 2.7 Å on average. In Figure 4.2, profiles of the line 1 and 2 are reported.

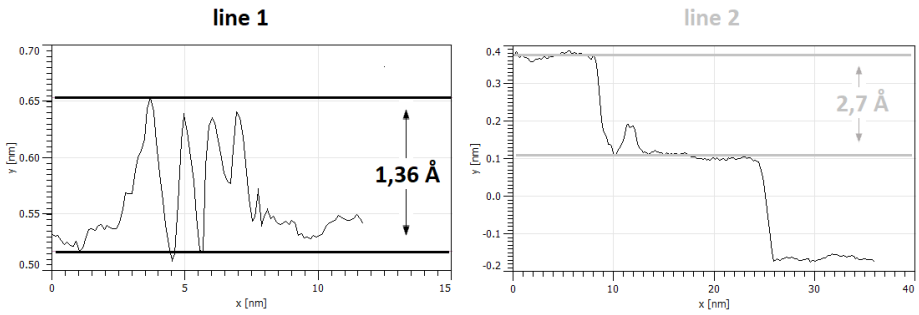

Figure 4.55 Line profiles of the ordered chain domain (line 1) and Au (111) steps (line 2) showed in figure 4.1c.

It must be remarked that measurements of the line profiles in STM images give us only apparent values, since, as discussed in section 2.2.2, the tunneling current, is influenced by both the electronic properties of the sample and tip, besides the topographic features of the sample. Due to the low resolution in STM images in figure 4.1, it is difficult to distinguish the organometallic structure of the chains.

By looking at the STM image of the sample annealed at 377 K in figure 4.3a, the formation of disordered domains after the increase in temperature is evidenced by the red circle. In addition, the close-up STM image (figure 4.3b) shows the presence of Au atoms among adjacent biphenyl groups, i.e. the organometallic structure, which is illustrated in figure 4.3d. Dot protrusions correspond to Au atoms, while dashes are the biphenyl groups.

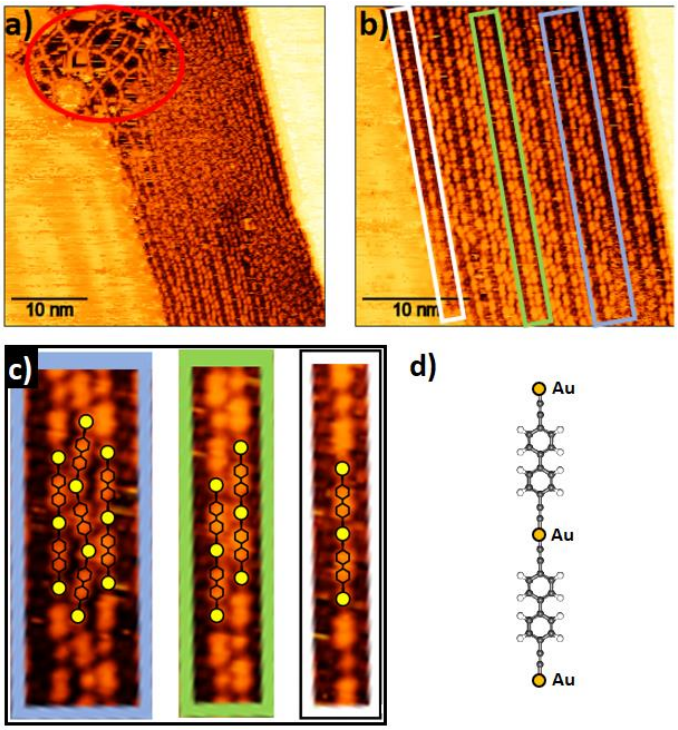

Figure 4.56 STM images of the chains annealed at 377 K. (a) (42.75x42.75 nm) Disordered domains appear after the increase in temperature. Set point (-0.548 V, 0.3 nA). (b) (29x29 nm) Three different dispositions of the chains: single (white), double (green) and triple (blue). Set point (-0.548 V, 0.3 nA). (c) Magnification of

the three dispositions. A schematic representation of the organometallic chain is overlapped. (d) Molecular model of the organometallic chain.

I identified in the STM image in figure 4.3b three different dispositions of the well-oriented chains. They were observed as isolated system (white rectangle), in pairs (green rectangle) or in groups of three (blue rectangle). It is interesting to notice that they tend to pack together in the most efficient way, avoiding the biphenyl bulky groups to stay close each other. Moreover, central chains in the 'triple configuration', showed an atypical 'zig-zag' disposition. To better visualize the three different dispositions, relative magnifications are reported in figure 4.3c, where schematic representations of the organometallic structure are overlapped to the STM image.

After a second annealing at 388 K, a slight increase in the amount and dimension of disordered domains was noticed, as shown in figure 4.4a. In the close-up STM image in figure 4.4b, chains appeared in both the isolated and triple disposition. Furthermore, unprecedented wavy lines were observed between the chains. One of those is indicated by the green rectangle in figure 4.4b, and, as one can notice, it is characterized by a sequence of dot protrusions. My hypothesis on their nature is that they are probably formed by Br atoms, which detached from the precursors during the chain formation via homocoupling reaction. This agrees with the observation and hypothesis made in the ref. 23 and ref. 24, as discussed in section 2.4.

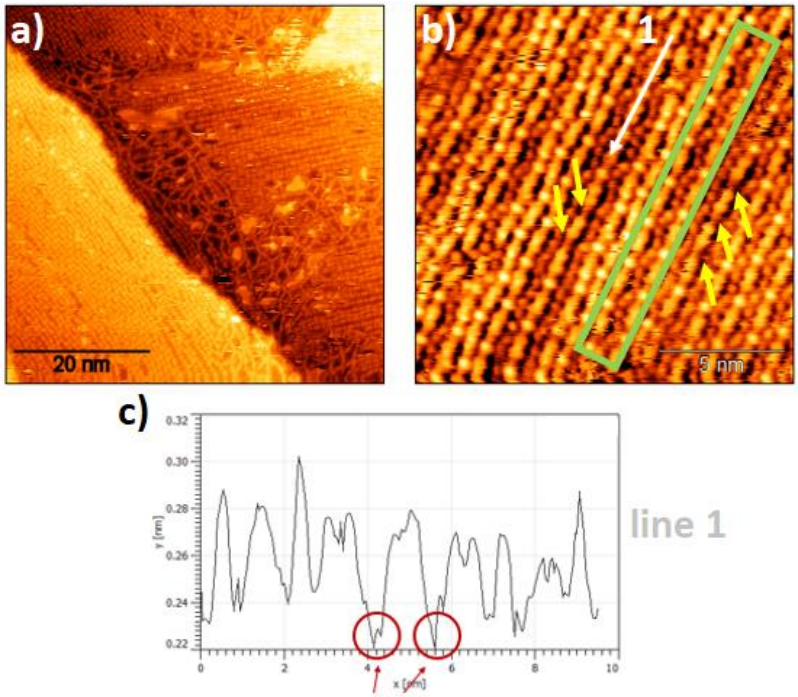

Figure 4.57 Sample annealed at 388 K. (a) (56x56 nm) Large-scale STM image of disordered and ordered domains. Set point (+0.98 V, 0.5 nA). (b) (15x15) Close-up STM image of organometallic chains and bromine chains (green rectangle). Gold atoms start to be released from the chains (yellow arrows). Set point (+1 V, 0.5 nA). (c) Line profile of the chain in figure 4.4b, where the missing gold atoms are encircled in red.

It also must be noted the disappearance of dot protrusions in some chains, which implies the release of gold atoms after a heat treatment at 388 K. The formed acetylenic linkages are indicated by yellow arrows in the figure 4.4b. The line profile reported in figure 4.4c clearly shows that two gold atoms are missing in the organometallic chain, as marked by red circles. This newly formed chain structure will be analyzed in detail, by means of line profiles, in the next section (4.1.2), dedicated to structural properties. Just for comparison, I remind that in the work done by Q. Sun et al. [23] the release of gold atoms was noted after an annealing cycle at 425 K. However, in that case the phenomenon concerned the totality of the investigated sample, not only few chains, like in my observations.

STM image of the sample annealed at 400 K, reported in figure 4.5a, confirmed the expected trend of the increase in the extension of disordered domains with the temperature. However, some well-oriented chain arrays were still present, as can be observed in figure 4.5b. It is interesting to notice that, even after thermal treatments and subsequent transition to a more disordered configuration, domain edges still followed the herringbone pattern of the gold substrate, as illustrated in figure 4.5a.

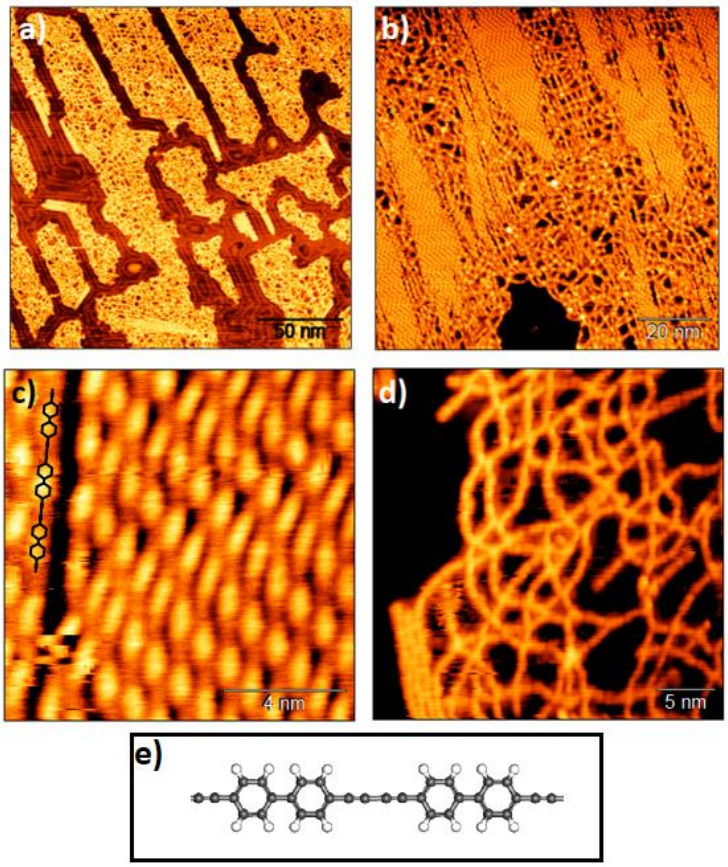

Figure 4.58 STM images of chains annealed at 400 K. (a) (200x200 nm) Almost completely disordered domains follow the herringbone pattern of the Au (111) surface. Set point (+1 V, 0.5 nA). (b) (100x100 nm) Some well-oriented domains are still present. Set point (+1 V, 0.5 nA). (c) (11x11 nm) Close-up STM image of ordered domain, where no gold atoms appear in the chain structure. Schematic representation of the C-C coupled structure is overlapped. Set point (-1 V, 0.2 nA). (d) (30x30) Close-up STM image of disordered chains. Set point (+1 V, 0.3 nA). e) Molecular model of the C-C coupled chain.

I then tried to take some close-up STM images of ordered and disordered domains to investigate the features of individual chains. However, the chain structure was hardly distinguishable in the disordered chain disposition (figure 4.5d). In figure 4.5c, instead, where close packed chains are imaged, it can be noted that dot protrusions of the gold atoms are missing, as clearly indicated by the overlapped schematic representation of the chain. This observation confirms the progressive transition from organometallic to pure-carbon systems, as consequence of the increase in temperature. The molecular model of the C-C coupled chain is shown in figure 4.5e.

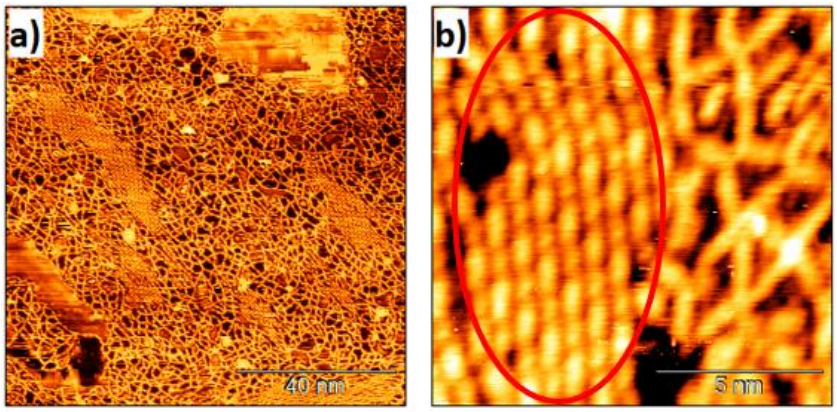

Figure 4.59 STM images of chains annealed at 430 K. (a) (100x100 nm) Large-scale STM image of disoredered chains with few ordered domains. Set point (+0.8 V, o.6 nA). (b) (12x12 nm) Close-up STM image of a well-oriented domain, where the organometallic structure can be observed. Set point (+0.8 V, 0.3 nA).

I finally performed an annealing at 430 K, and what I observed was in part unexpected. Indeed, large-scale STM images, as the one in figure 4.6a, showed an almost completely disordered chain disposition, with few ordered domains, similar to what observed after the annealing at 400 K. However, close-up STM images, as the one reported in figure 4.6b, occasionally revealed still present regions of organometallic chains in well-oriented domains. After this observation it has been not possible for me to draw some concrete conclusions about the dependence on temperature of the release of gold atoms from the chain structure, which I initially expected to be linear. Hence, dynamics of this phenomenon have still to be fully understood and future experiments could be addressed to the specific investigation of them.

Summarizing what observed, concerning the morphology of the deposited molecular chains, I can conclude that, bBEBP molecules interacted with the Au (111) surface, binding with gold atoms and giving rise to long molecular chains, which packed together in well-oriented domains. The growth of these nanostructures was guided on the one hand by the herringbone pattern and on the other hand by the monoatomic steps of the Au (111) surface layer. Inside ordered domains, chains were observed both in groups, composed by two or three of them, and as isolated systems, with Br atoms, detached from the precursors, aligned in between. Then, annealing cycles caused the unpacking of the chains and the formation of disordered domains, which showed an increase in the extension by

raising the annealing temperature. After the annealing at 388 K, the release of the gold atom from the chain structure was observed for the first time.

4.1.2. Structural properties

Once the disposition of the deposited nanowires on the gold substrate and the effects of the temperature on the sample morphological properties have been discussed in section 4.1.1, it can be useful to provide now some valuable information on the periodicity, i.e. the molecular chain building block length, and, in general, on the measures of the close-packed chain domains. This will be accomplished with the aid of line profiles on high resolution STM images.

As previously discussed, chains in the sample annealed at 377 K, are characterized by an organometallic structure. The protrusion of the gold atoms can be observed in the line profile in figure 4.7, in correspondence of the blue arrows. Peaks of the biphenyl groups are broader than those of the gold atoms and, in some cases, the two peaks of the single phenyl groups can be distinguished, as those encircled in red.

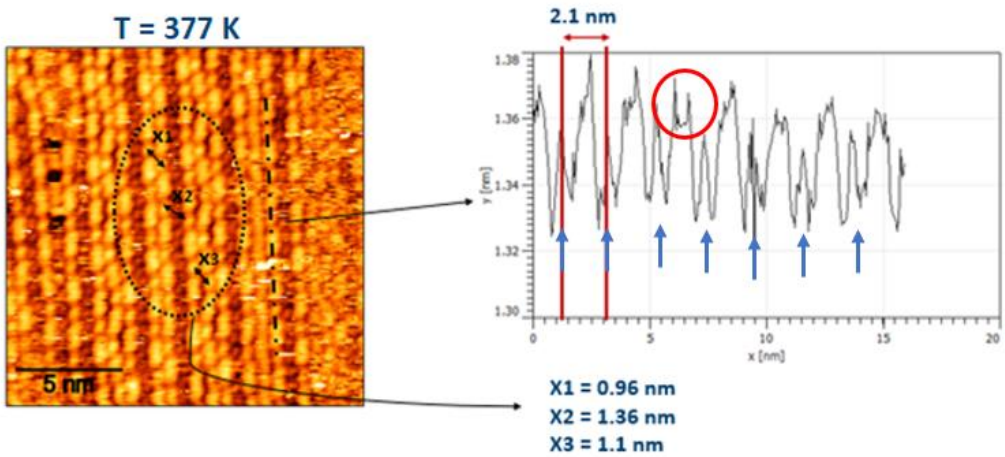

Figure 4.60 (left) (42.75x42.75 nm) STM image of the sample annealed at 377 K, where measures X1, X2 and X3 are indicated. Set point (-0.548 V, 0.3 nA). (right) Line profile of the organometallic chain. Gold atoms are indicated by blue arrows. A biphenyl group, where the two peaks of single phenyl rings are visible, is encircled in red. The measured periodicity of the chain is 2.1 nm.

The periodicity of the structure was measured by taking an average value of the distances between consecutive Au atoms, and resulted to be 2.1 nm, which is in accordance with what reported by Q. Sun group [23]. Preliminary measurements, aimed at characterizing the repeating unit of the aligned chains were done and values are reported in figure 4.7, as parameters X1, X2 and X3. They correspond to the distances between adjacent Au atoms inside the double and triple chain dispositions, previously introduced in section 4.1.1, and between them. The reported measurements are average values mediated over several points.

Similar measurements were carried out on the sample annealed at 388 K and revealed an analogous value as far as the periodicity (2.06 nm) is concerned, as shown in figure 4.8.

However, the sharp gold peaks in the line profile are less marked compared to those of the sample annealed at 377 K. This may indicate that gold atoms were removed from the chain during the annealing cycle at 388 K, yet observed in figure 4.4, and acetylenic linkages formed between biphenyl groups. According to this hypothesis, low peaks among biphenyl groups in the line profile in figure 4.8, should be the electronic cloud of the acetylenic bonds. This is plausible since, as explained in the chapter 2, the STM tip does not map the real topography of the sample, but rather a convolution of the electronic properties of the sample and tip with the real profile of the scanned surface. In this case, interchain distances (parameters X1, X2, X3) were taken between neighbor biphenyl groups, since they are brighter and thus more easily detected in line profile measurements. It also must be noted that they do not correspond to the same features measured by parameters in figure 4.7, since chains are disposed in a different way over the gold substrate. For instance, the 'double disposition' of chains, imaged in figure 4.7, was not observed in figure 4.8.

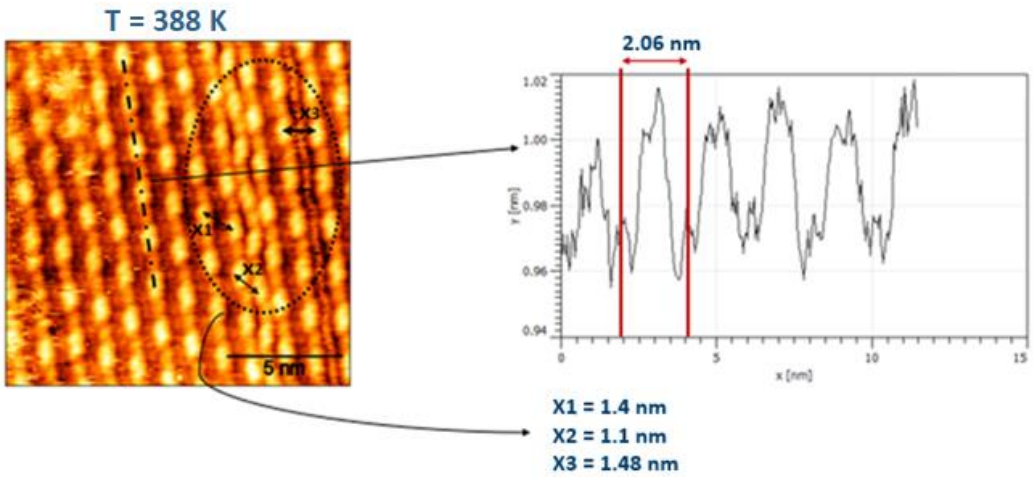

Figure 4.61 (left) (15x15 nm) STM image of the sample annealed at 388 K, where measures X1, X2 and X3 are indicated. Set point (-0.957 V, 0.5 nA). (right) Line profile of the organic chain. Peaks among biphenyl groups correspond to acetylenic linkages. The measured periodicity of the chain is 2.06 nm.

I then proceeded similarly with investigations on samples annealed at 400 K and 430 K. Results for both the annealing temperatures are reported in figure 4.9. The high-resolution STM image of the sample annealed at 400 K (figure 4.9a) shows an array of wavy chains, which do not present gold atoms between phenyl groups, as confirmed by the line profile. The periodicity of 2.04 nm is lower than in the organometallic structure shown in figure 4.7 (periodicity 2.1 nm), as we should expect due to release of gold atoms. Q. Sun and his groups predicted, by means of DFT calculations, a decrease of about 0.2 nm in the periodicity with the removal of gold atoms from the chain structure. In our case, instead, the decrease in the periodicity is 0.06 nm. However, it should be noted that STM measurements could be affected by thermal drift or, more in general, artifacts, and thus could slightly deviate from theoretically predicted values. As discussed in section 4.1.1, I observed an unexpected organometallic chain structure in the sample annealed at 430 K (figure 4.9b). In line profile measurements, peaks of gold atoms are clearly

distinguishable, and the periodicity of the structure is 2.13 nm, in agreement with the value measured on organometallic chains in the sample annealed at 377 K (figure 4.7). Furthermore, it should be stressed that at higher temperatures (figures 4.9a-b) molecular chains in well-oriented domains are tighter packed, compared to lower temperatures (figure 4.7 and figure 4.8). This phenomenon may have led to the release of Br atoms, which are no longer observed in interstitial sites among chains in samples annealed at 400 K and 430 K (figure 4.9a-b). In STM investigations of the sample annealed at 430 K, large bright spots, which I hypothesized formed by aggregation of Br atoms released from interstitial sites, were observed. STM images illustrating the bright spots and the chemical characterization of the sample by Auger spectroscopy are reported in the appendix.

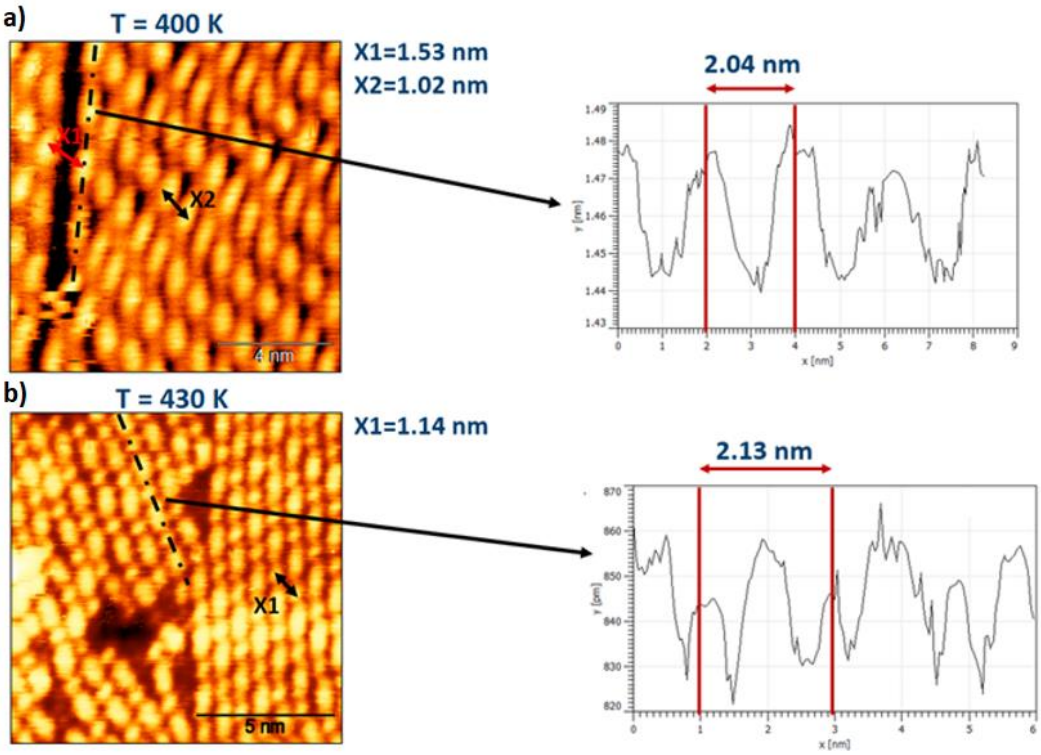

Figure 4.62 (a) (left) (11x11 nm) STM image of chains annealed at 400 K, where measures X1 and X2 are indicated. Set point (-1 V, 0.2 nA). (rigt) Line profile of the organic chain, where only peaks of biphenyl groups are visible. The measured periodicity is 2.04 nm. (b) (left) (12x12 nm) STM image of chains annealed at 430 K, where an unexpected organometallic structure of the chain is observed. Measure X1 is indicated. Set point (+0.7 V, 0.6 nA). (right) Line profile of the organometallic chain, where peaks of gold atoms among biphenyl groups can be noted.

I conclude this section, showing an interesting feature, observed in a high-resolution STM image of the sample annealed at 388 K, which is reported in figure 4.10. After a careful observation of the image, one can recognize the organometallic structure, which characterizes the chains annealed at 388 K. However, between biphenyl groups, the presence of three dot protrusions was occasionally observed, as those encircled in red in the figure 4.10. By analyzing the line profile of this triple-dot structure, one can notice that the central peak is higher than lateral ones. For this reason, I excluded the idea of a structure formed by three Au atoms and I accredited the hypothesis that associates the

central peak to the Au atom and the lateral peaks to the electronic clouds of the acetylenic linkages between the Au atom and biphenyl groups, similarly to what observed in figure 4.8. The origins of the elevated resolution of the acetylenic linkages may be related to temporary modified conditions of the tip, which caused changes in the STM imaging.

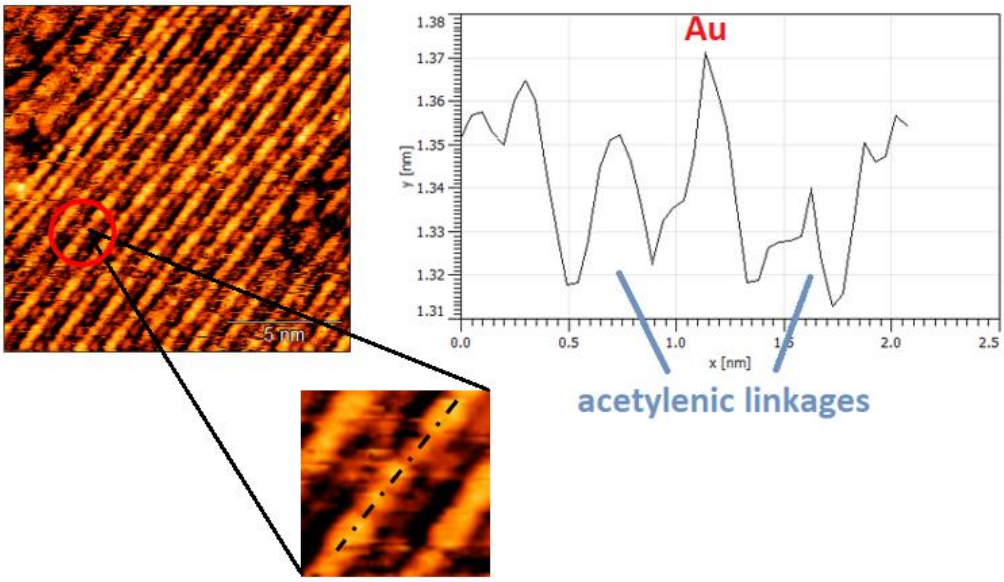

Figure 4.63 (left) (15x15 nm) High-resolution STM image of chains annealed at 388 K, where the triple-dot sequence is highlighted by the red circle and magnified. Set point (-0.35 V, 0.5 nA). (right) Line profile of the organometallic chain shows three peaks between the two biphenyl groups. The high central peak corresponds to the Au atom, while lower lateral peaks are the acetylenic linkages.

4.1.3. Electronic properties

STM investigations can also provide us information on surface local electronic properties of the deposited molecular chains. This is achieved by the study of differential conductivity (dI/dV) maps and STS measurements. The former are acquired by scanning the surface in constant current mode (CCM), and illustrate the evolution of the differential conductivity as a function of the lateral coordinates for a selected applied voltage, as discussed in section 2.1. Marked contrast in these maps indicates a local variation of the differential conductivity and thus of the electronic properties along the sample surface in the investigated area. The latter, instead, are measurements of the variation of the differential conductivity in a selected range of applied bias, acquired on a certain point over the scanned surface. By analyzing STS spectra, some important conclusions about the density of states (DOS) of the investigated sample can be drawn. In addition, by observing changes in the STM imaging at different applied bias, it is possible to detect some relevant differences in the electronic properties of the sample components, such as, for example, molecular chains and the gold substrate. This derives from the fact that STM imaging is influenced by local electronic properties of the investigated sample.

In figure 4.11 close-up STM images of the same disordered domain in the sample annealed at 400 K are shown. These were acquired at the same current and at voltages ranging from +0.7 V to -0.7 V. On the domain border, a well-oriented array of chain can be observed, as indicated by the red circle in figure 4.11a. In the previous section I showed a high resolution STM image (figure 4.9) of linear chains after the annealing at 400 K and the absence of dot protrusions between biphenyl groups indicated that gold atoms got released from the structure. Bearing this in mind, some important observations can be done over the STM images reported in figure 4.11. As one can notice, for applied voltages +0.7 V and -0.7 V, uniform linear structures are observed, while when it gets closer to the Fermi level, i.e. for ±0.5 V and ±0.3 V, bright spots with a higher apparent height with respect to the rest of the chains structure start to appear. In the light of what previously observed about the chain structure after the annealing at 400 K, I hypothesized that dot protrusions correspond to biphenyl groups rather than gold atoms. Hence, the change in the contrast by varying the bias would indicate that the electronic properties difference along the chain is more marked for states near the Fermi level.

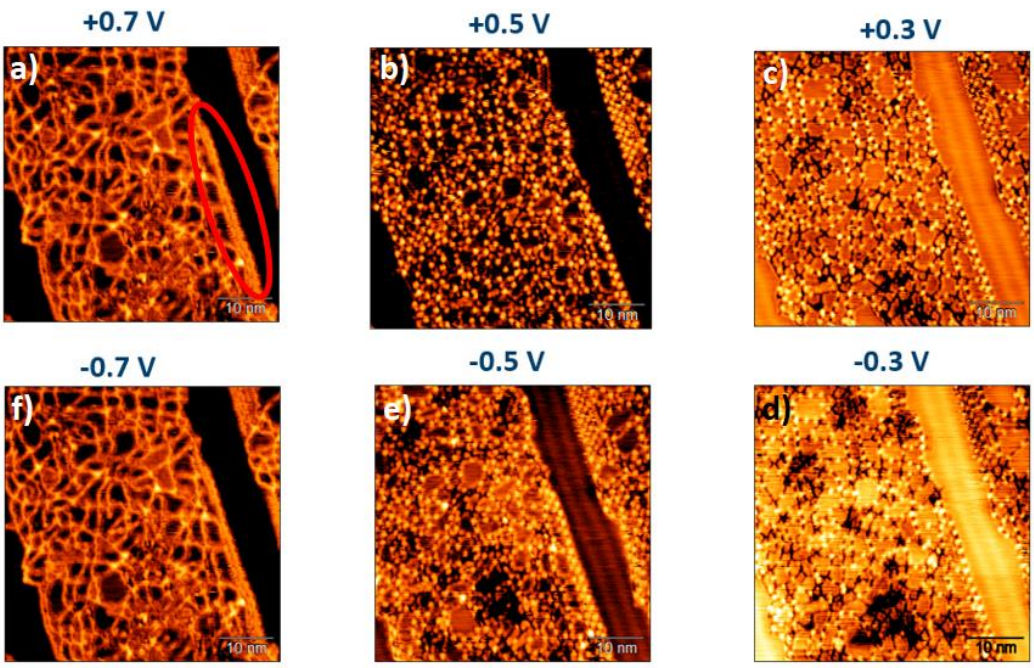

Figure 4.64 (50x50 nm) STM images of the disordered domain in the sample annealed at 400 K, taken at different bias. Tunneling current was set to 0.5 nA. In (a) the well-oriented domain is encirceld in red. In (b), (c), (d) and (e) the bright spots corresponding to biphenyl groups can be noticed.

If one wanted to have further information on the electronic properties of a single chain, it could be useful to perform STS measurements on different points along the chain, as was successfully achieved in the work done by Chen-Hui Shu [24], discussed in section 2.4. However, I was not able to do this, since when I observed the linear structures at atomic scale, the tunneling current was not enough stable to allow me the acquisition of STS spectra.

In figure 4.12, it is possible to observe differential conductivity (dI/dV) maps acquired on the same sample area shown in figure 4.11. These were acquired at applied bias ±1 V, ±0.7 V, ±0.3 V. The first thing to notice is the increase in the contrast at low bias, compared to high bias, between the disordered domain and the region of gold without deposited chains. This feature may indicate that the region with deposited chains and that without chains have similar electronic properties for energies far from the Fermi level, while, approaching the Fermi level, their electronic properties start to differ from each other. Furthermore, at ±0.3 V the surface of the disordered domain in figures 4.12c and 4.12d appears more corrugated with respect to the case of other voltages and dot-like protrusions, like those observed in figures 4.11b-d, can be noticed. This feature suggests that, as previously discussed in the analyses of figure 4.11, at low bias the electronic properties vary more markedly along the chain structure. In addition, at -0.7 V and -1 V (figures 4.12e and 4.12f), some structures in the region with the deposited chains are much brighter than the rest of the sample, which indicates the high electronic contribution of those structures in that energy range. Due to their irregular shape, I made the hypothesis that they consist of a different form of hybridized-carbon structures, rather than biphenyl groups, which were hypothesized to correspond to dot protrusions in figures 4.11b-e. They may be originated, for instance, from the crosslinking reactions between molecular chains.

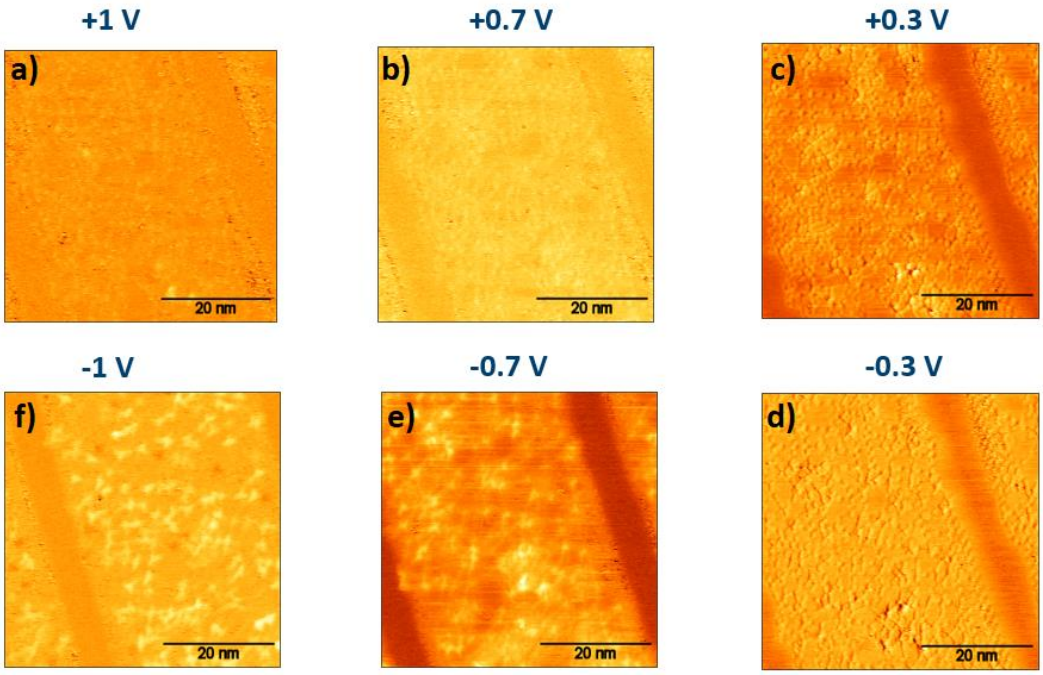

Figure 4.65 (50x50 nm) dI/dV maps of STM images shown in figure 4.11. The tunneling current was set to 0.5 nA. At low bias the contrast between the disordered domain and the gold substrate is more marked. In (c) and (d) dot-like protrusions are displayed. In (e) and (f) irregularly-shaped bright spots appear in the disordered domain.

A higher electronic contribution was observed for well-oriented arrays of chains compared to disordered regions at bias +1 V, as shown in the figure 4.13, where both the STM image and the dI/dV map of the sample annealed at 400 K are reported. In fact, as

one can notice in figure 4.13b, ordered domains appear much brighter than disordered ones and the gold substrate.

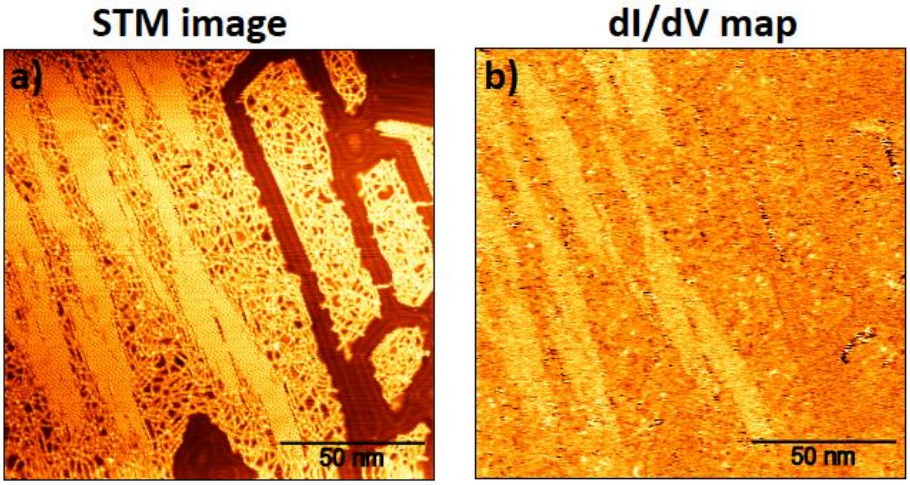

Figure 4.66 (150x150 nm) Large-scale STM image (a) and dI/dV map (b) of the ordered and disordered domains in the sample annealed at 400 K. In (b) well-oriented domains appear brighter than the rest of the image. Set point (+1 V, 0.5 nA)

As last example of differential conductivity map, I illustrate in figure 4.14 the STM image and dI/dV map of aligned chains in the sample annealed at 388 K. In the STM image the single and the triple chain dispositions are observed. In section 4.1.1, in the analysis of the figure 4.4b I discussed the nature of the wavy chains between the organometallic molecular chains and I hypothesized that they are probably formed by Br atoms, in agreement with what found in literature. This idea is supported by the analysis of the differential conductivity map reported in figure 4.14b, which shows a color contrast between well-oriented arrays of chains and interstitial spaces among them (indicated by yellow arrows in figure 4.14a and 4.14b), where the hypothetical bromine chains are located.

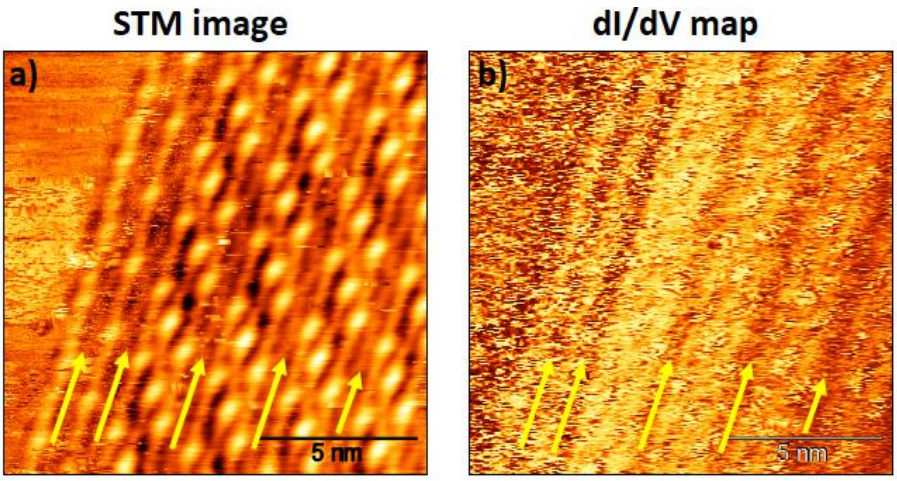

Figure 4.67 (15x15 nm) Close-up STM image (a) and dI/dV map (b) of well-oriented domains with bromine chains in between in the sample annealed at 388 K. In (b) the color contrast between bromine chains and ordered domains of molecular chains can be observed. Set point (+0.95 V, 0.5 nA).

Moreover, to further investigate the surface local electronic properties of the deposited structures, STS measurements were performed on both the gold substrate and the region covered with linear structures. STS spectra were acquired on different sites of the same region and the resulting average curves have been plotted in figure 4.15. Due to the instability in the current signal I was able to perform measurements only in a reduced voltage range, which is from -1 V to +1 V. At higher applied bias the STS curved diverged too much and showed a too high instability to be considered as a reliable datum.

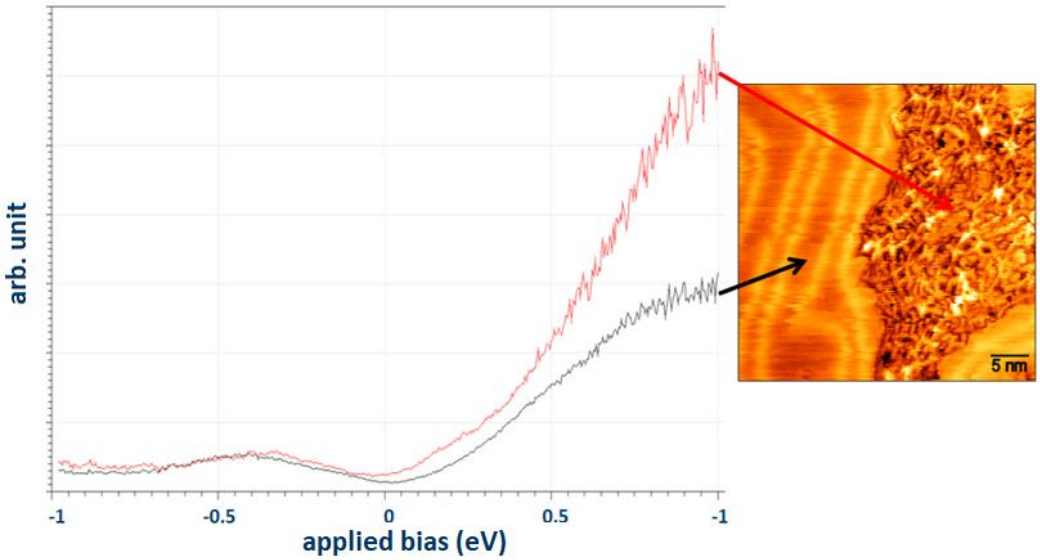

Figure 4.68 STS spectra acquired on regions with (red curve) and without (black curve) deposited chains. The (40x40 nm) STM image shows a disordered domain in the sample annealed at 400K. Set point (-1 V, 0.3 nA)

I tried also to acquire some STS spectra on well-oriented domains, but the signal was too noisy. By looking at the dI/dV behavior in figure 4.15, it is possible to notice that STS curves for the regions with and without the linear structures are almost completely overlapped at negative bias. From 0 V to upper voltage values, instead, the dI/dV curve of the region covered with chains starts to assume higher values with respect to curve corresponding to the uncovered region. A possible interpretation of this phenomenon could be the appearance of a new electronic band at energies just above the Fermi level, i.e. unoccupied states, in the density of states of the molecular chains. Furthermore, the localized band at -0.5 V could be related to surface electronic state of Au (Shockley state), introduced in section 3.2, which exerts a certain influence also on electronic states of the chains.

The above reported measurements were thus just a preliminary investigation, which anyway revealed us some features of the surface local electronic structure of the sample. To get more information about the electronic structure of the chain, the acquisition range should be increased and local STS measurements on different positions along the chain structure should be performed. However, as already mentioned, this is a hard work to do, since both the atomic scale resolution and a good stability in the tunneling current must be achieved to allow the acquisition of reliable STS spectra. In this sense, it could be very

convenient to work at lower temperatures. In addition, as discussed in the section 2.3.1, concerning the theory of STS, the extracted dI/dV signal should be properly normalized in order to unveil the local density of states of the investigated structure.

4.2. Raman spectroscopy of carbon atom wires

Once the morphological, structural and electronic properties of the annealed sample had been largely characterized by means of large-scale and close-up STM images, line profiles, differential conductivity maps and STS spectra, I extracted the sample from the ultra-high vacuum apparatus to perform further analyses on vibrational properties. These measurements were conducted ex-situ by means of a Raman spectroscopy apparatus. The investigated sample had been previously annealed at 430 K in the vacuum chamber. My intent is that of comparing the Raman spectra of samples annealed at different temperature, trying to identify possible relations between the increasing temperature and the peaks shape and position. For this purpose, the acquired Raman spectrum of the sample annealed at 430 K has been compared with spectra previously acquired on samples annealed at 373 K and 406 K. In addition, I performed Raman measurement on the precursor bBEBP, in order to study also the variations in the vibrational structure caused by the homocoupling of the bBEBP molecules with the consequent formation of the linear sp-carbon chains. I used green light (λ=514 nm) for the acquisition of spectra.

Due to problems related to the instability of the deposited molecular chains when exposed in air, I had to perform Raman measurements suddenly after the sample was extracted from the vacuum chamber, in order to avoid the degradation of the linear structures and the transition from the sp- to the sp^2-hybridized state of carbon atoms.

With the aim of better characterizing the features of the Raman peaks I fitted the experimental Raman peaks with one or more Lorentzian curves. In this way I was able to detect with a certain accuracy the values of the Raman shift and the heights of both the main peaks and possible shoulders.

Finally, my experimental Raman spectra have been compared with DFT-calculated Raman spectra of computational models of the single precursor and the dimer, formed via the coupling of two precursors. In addition, to investigate the effects of the gold substrate on the vibrational properties of the chains, Raman spectra of the dimer both interacting with an Au_4 complex and with a gold atom incorporated in the structure were simulated. DFT calculations were performed by A. Milani, who collaborated with me at the Nanolab.

In figure 4.16, Raman spectra of the precursor ("powder"), the sample annealed at 373 K, 406 K and 430 K are reported, in order to be compared to each other. One can soon notice the presence in all the spectra of four main peaks.

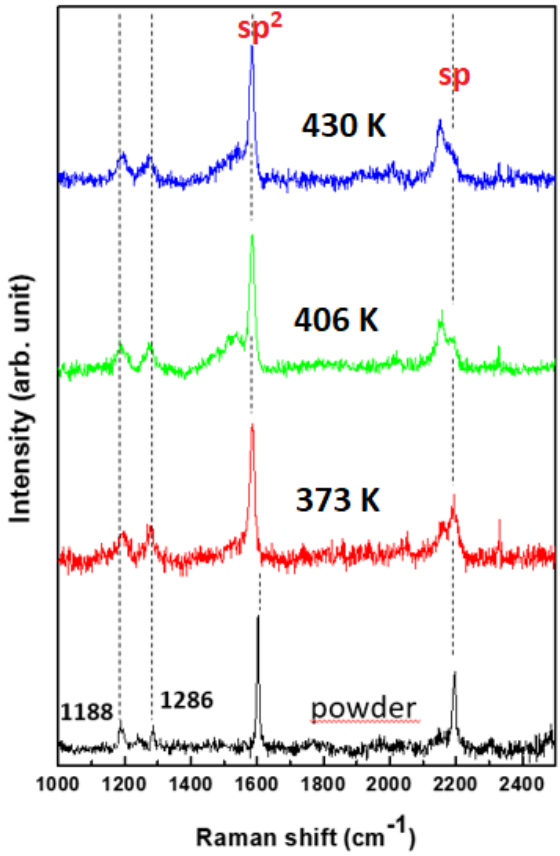

Figure 4.69 Raman spectra of the precursor ('powder') and samples annealed at 373 K, 406 K and 430 K. sp-C and sp^2-C peaks are indicated. At lower wave numbers peaks of the vibrational modes of phenyl rings are displayed too.

As indicated in the figure, the peak at Raman shift around 2200 cm^{-1} is characteristic of the sp-carbon, that around 1600 cm^{-1} corresponds to in-plane stretching mode of the sp^2-carbon rings, while the two peaks at lower Raman shift are associated to other vibrational modes of the phenyl rings. It also must be observed the appearance of a shoulder on both the sp and sp^2 peaks following the formation of the chain. In the case of the sp^2 peak, the shoulder does not display significant changes at increasing annealing temperature, while, in the case of the sp peak, the intensity of the shoulder increases with the annealing temperature and in sample annealed at 406 K and 430 K is even higher than the sp peak. The intensity of the sp-C peak, instead, shows a decrease with the temperature. This trend can be better appreciated in the close-up images of the sp peak shown in figure 4.17b. In the light of what observed in STM images of the chains, we may suppose that this phenomenon is related to the gradual release of gold atoms from the organometallic chains with the increase in temperature. In fact, we can make the hypothesis that the sp-C peak at higher wave numbers and the one at lower values correspond to the sp-carbon vibrational modes of the organometallic chains and pure-carbon chains, respectively.

Hence, by assuming this, one can note that the trend in the intensities of the two peaks agrees with what in part observed by STM investigations: the rise in the amount of chains without gold atoms in the structure, following the increase in the annealing temperature. In addition, a slight broadening of both the sp and sp^2 peaks can be observed in figure 4.17, by comparing the spectrum of the precursor with those of the annealed sample. This phenomenon may be related to the confinement effects arisen after the chain formation and subsequent thermal treatments. As indicated in figure 4.17a, following the chain formation, the sp^2 peak is shifted towards a lower wave number (~1584 cm^{-1}), compared to the peak of the precursor (~1602 cm^{-1}), and no further Raman shifts occur with the increasing temperature. As far as the position of the sp peak is concerned, instead, wave numbers of the main peak (~2190 cm^{-1}) and the shoulder (~2155 cm^{-1}) remain almost constant either after the coupling of the precursors or following further annealing cycles, as illustrated in figure 4.17b. Also, the wave number of the two peaks corresponding to vibrational modes of the phenyl rings (~1188 cm^{-1} and ~1286 cm^{-1}) do not shown any appreciable change in the four Raman spectra.

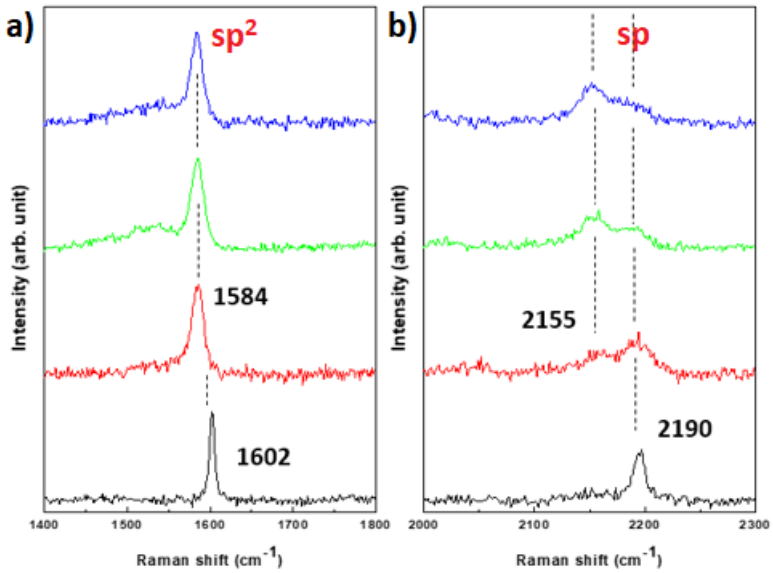

Figure 4.70 Close-up view of sp-C and sp^2-C peaks in the spectrum of the precursor and annealed samples.

In order to characterize the sp and sp^2 peaks more in detail, I fitted them with Lorentzian curves and I extrapolated some relevant parameters, such as the height and area ratios between the main peak and its shoulder.

The fitting of the sp-carbon peak is shown in figure 4.18, where peaks corresponding to the three different annealing temperatures are reported and main information are summarized in the table below.

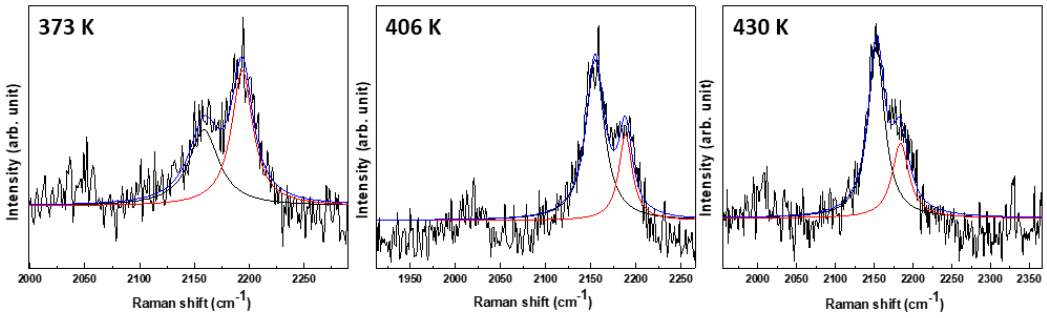

	373 K	406 K	430 K
sp-C peak	2193 cm^{-1}	2188 cm^{-1}	2183 cm^{-1}
shoulder	2158 cm^{-1}	2154 cm^{-1}	2152 cm^{-1}
Area ratio (**sp-C/shoulder**)	1.27	0.4	0.45
Height ratio (**sp-C/shoulder**)	1.7	0.53	0.43

Figure 4.71 (top) Fitting of the sp-C peak at different annealing temperatures by means of Lorentzian curves. The sp-C peak and its shoulder are colored in red and black, respectively, while their sum is given by the blue curve. (bottom) The table summarizes the main parameters, such as the position of the peaks and the heigth and area ratios.

The curve fitting the sp-carbon peak has been colored in red, that fitting the shoulder in black, while their sum is represented by the blue curve. A very little Raman shift towards lower wave numbers has been observed for both the sp-C peak and its shoulder with increasing temperature. This may suggest a light softening of the acetylenic bonds along the linear chain, caused by the rise in temperatures. Values of the height ratio reported in the table confirmed what noticed also with the naked eye, that is a significant increase of the intensity of the shoulder and decrease of the intensity of the sp-carbon peak by increasing the annealing temperature.

I then proceeded with the same type of analysis on the sp^2-carbon peak, as reported in figure 4.19. As one can observe sp^2-carbon peak and its shoulder are fitted by the red and black curve, respectively, while their sum is represented by the blue curve. As written in the table, wave numbers of the sp^2-C peak and the shoulder are almost the same for all the annealing temperatures. It must be pointed out that fitting the shoulder of the sp^2-C peak has not been so simple, since, as one can notice in experimental Raman spectra in figures 4.16 and 4.17a, it cannot be easily distinguished, like that of the sp-carbon peak. Finally, by looking at the height ratios, which has been taken between the intensity of the sp^2-C peak and that of the shoulder, one can observe variations in the intensity of the shoulder with the rise in temperature. The intensity of the sp^2-C peak, instead, stays unchanged for all the different annealing temperatures.

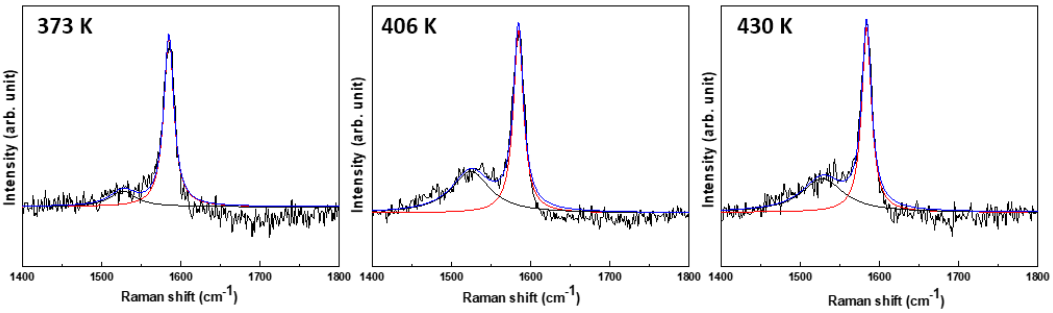

	373 K	406 K	430 K
sp^2-peak	1584 cm^{-1}	1584 cm^{-1}	1582 cm^{-1}
shoulder	1528 cm^{-1}	1525 cm^{-1}	1529 cm^{-1}
Area ratio (**sp^2-C/shoulder**)	15.8	4.65	7.38
Height ratio (**sp^2-C/shoulder**)	10	1.66	3.53

Figure 4.72 (top) Fitting of the sp^2-C peak at different annealing temperatures by means of Lorentzian curves. The sp^2-C peak and its shoulder are colored in red and black, respectively, while their sum is given by the blue curve. (bottom) The table summarizes the main parameters, such as the position of the peaks and the heigth and area ratios.

To conclude this section on Raman measurements, I report now the DFT-calculated Raman spectra, which are illustrated together with the above discussed experimental Raman spectra in figure 4.20. DFT calculations were performed by A. Milani and coworkers.

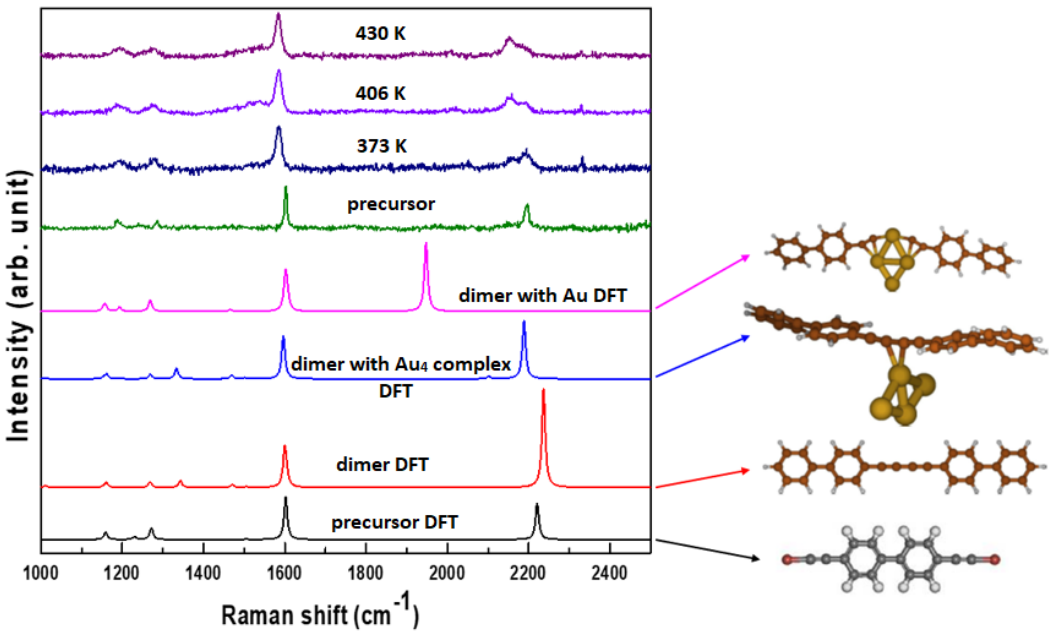

Figure 4.73 DFT-simulated Raman spectra compared with experimental spectra. DFT calculations were performed for different molecular models: the bBEBP precursor (black curve), the dimer (red curve), the dimer interacting with an Au_4 complex (blue curve) and the dimer with a gold atom in between (pink curve).

Spectra obtained by DFT calculations have been properly scaled, in a way that the sp^2 peaks are centered at ~1600 cm^{-1}, which is the calculated wave number for the sp^2 peak of the precursor. First thing to notice is that this value coincides with the experimental datum, which was reported to be ~1602 cm^{-1}, as indicated in figure 4.17. Initially, Raman spectra for both the precursor bBEBP and the dimer molecule have been simulated, which correspond respectively to the black and red lines in figure 4.20. It must be noted that the DFT-calculated spectrum of the precursor shows a sp-carbon peak which is slightly shifted towards higher wave numbers with respect to the experimental value. The same has been observed in the DFT-calculated spectrum of the dimer, which also display an increased intensity of the sp-carbon peak. Then, Raman spectra of the dimer interacting with gold atoms have been simulated, in order to investigate the influence of the gold substrate in Raman measurements. Two different situations were considered. In the first the dimer interacts with an Au_4 complex, while in the second one a gold atom is incorporated in the middle of the dimer structure. In figure 4.20 the two Raman spectra with the related model, described above, are represented by the blue and pink lines, respectively. One can soon notice that the Raman spectrum of the dimer interacting with the Au_4 complex displays a sp-carbon peak shifted towards lower wave numbers and with a decreased intensity, compared to that of the isolated dimer. Moreover, the sp-C peak is centered on a wavenumber which is comparable with the value of the sp-C peak found in experimental spectra. The DFT-simulated spectrum of the dimer with the gold atom in the structure, instead, shows a sp-C peak centered at a wavenumber significantly lower than the experimental datum. Hence, the model that fits better the experimental Raman spectra is that of the dimer interacting with the Au_4 complex.

After having compared our results with the DFT-simulated spectra, I can thus conclude that the gold substrate exerts a certain influence also on the vibrational properties of the deposited molecular chains.

Chapter 5

Conclusions and outlook

This thesis work has been entirely devoted to the characterization, by means of scanning tunneling microscopy, scanning tunneling spectroscopy and Raman spectroscopy, of sp-carbon chains deposited on an Au (111) surface. The state-of-art of the research on carbyne has been widely discussed in chapter 1, where, on the one hand the enormous potentialities of sp-carbon systems and, on the other hand, the problems encountered in the synthesis and stabilization of these structures have been introduced. Then, theories at the base of the working principles of the STM and STS have been treated in the first part of the chapter 2, whereas in the second part few works concerning STM/STS investigations of sp-carbon wires have been reported from literature. Concluding, goals and objectives of my experiments have been stated. In chapter 3, the experimental apparatus, the materials and methods employed in the preparation and analyses of the sample have been described in detail. Finally, the characterization of the morphological, structural, electronic and vibrational properties of the deposited carbon atom wires have been discussed in chapter 4.

The deposition of the linear chains was successfully accomplished, after few attempts, by the thermal evaporation of the molecular precursor on the Au (111) substrate in ultra-high vacuum. This technique resulted, however, to be not very accurate and I had a hard time trying to find suitable parameters of voltage, current and time, to achieve the desired coverage of the sample. In future experiments this procedure will be significantly simplified, since a high-precision molecular evaporator has been recently mounted on the preparation chamber, which is currently under maintenance.

Deposited samples were further investigated by in-situ STM measurements. As-deposited structures appeared to form well-oriented domains, by aligning each other along the herringbone pattern or following the monoatomic steps of the Au (111) surface, which also acted as nucleation sites, favoring the attachment of chain ends. Series of annealing cycles at increasing temperature (377 K, 388 K, 400 K and 430 K) were then carried out by radiative heating of the sample, in order to characterize the evolution of properties of observed ordered domains with the rise in temperature. At first, a progressive disordering of molecular chains with the temperature was noticed. However, some well-oriented domains were still present after the annealing at 430 K. A special effort has been then dedicated to the study of the chain structure, through the analysis of line profiles, acquired on samples annealed at different temperatures. The C-Au-C organometallic structure was noted after the annealing at 377 K, in agreement with what found in literature [23]. Close-up STM images of individual chains after annealing cycles at higher temperatures revealed the disappearance of the gold atoms from the linear structure and the consequent homocoupling of adjacent C atoms. By investigating the chain structure of an ordered domain after the annealing at 430 K, however, the dot-dash sequence

typical of the organometallic chains was observed. To better understand the role of the temperature in the release of gold atoms from the chains, further targeted investigations should be carried out. Morphological and structural analyses thus highlighted the active role played by the Au (111) surface, which not only guided the nucleation and growth of the linear chains, but also contributed with single atoms to the formation of an organometallic structure at low temperatures. It is worth mentioning also that high-resolution STM images of the sample annealed at 388 K showed the presence of wavy chains aligned along the deposited structures. These were hypothesized to be formed by bromine atoms detached from the precursors during the chain formation. After annealing cycles at 400 K and 430K, well-oriented domains appeared tighter packed, suggesting that Br atoms were released from interstitial sites among chains.

Furthermore, electronic properties of the molecular chains were investigated at first through the comparison between STM images (after annealing at 400 K) taken at different bias and constant current, and then by means of differential conductivity (dI/dV) maps and STS spectra. STM imaging at lower bias displayed a marked contrast along the linear structures compared to high-bias imaging, unveiling changes in the electronic properties at different energy levels. In particular, bright dot protrusions were assumed to correspond to biphenyl groups, since gold atoms were supposed to be no longer present in the molecular chains. dI/dV maps, instead, showed a change in the color contrast between the chain domain and the gold substrate by varying the bias, indicating variations of the local surface conductivity. Preliminary measurements by STS were conducted on both the gold substrate and a disordered domain. The acquired spectra displayed a comparable behavior for negative bias, while for positive bias the curve of the chain domain showed a significant increase with respect to the curve of the gold substrate, suggesting a higher density of states for those energy values.

Finally, ex-situ Raman spectroscopy measurements were performed, with the aim of unveiling the vibrational structure of the sample annealed at 430 K. The spectrum was compared with previously-acquired spectra of the precursor and molecular chain samples annealed at 373 K and 406 K. A detailed analysis was carried out with the help of curve fittings by Lorentzian curve. A curious trend was noticed in the intensity of the sp-C peak and its shoulder. Indeed, by increasing the annealing temperature the shoulder decreased and the sp-C peak increased in the intensity. A possible interpretation of this phenomenon could be that the sp-peak at higher wave numbers corresponds to the vibrational mode of the organometallic chains, which depleted with temperature, leading to an increase in the amount of pure-carbon chains, whose Raman peak is the one at lower wave numbers. Sp^2-C peak, instead, did not show any appreciable variation with the increasing annealing temperature. In conclusion, experimental spectra were compared with DFT-calculated spectra of the precursor, the isolated dimer and the dimer either interacting with an Au_4 complex or incorporating an Au atom in the middle. The model of the dimer interacting with the gold complex showed a simulated Raman spectrum, which could be almost overlapped with the experimental curve. Hence, it can be concluded that the gold

substrate exerts a certain influence also on the vibrational structure of the deposited chains.

Despite important results, concerning the deposition and characterization of bBEBP on Au (111) surface, have been achieved so far, there is still a lot of work to do to provide a deeper knowledge of these sp-carbon systems. For example, simulated STM images could be realized and employed as reference for experimental observations and an aid for the correct interpretation of the observed features. Furthermore, the acquisition of STS spectra on different sites along the individual chain could be a powerful method to better understand the evolution of the linear electronic structure. In order to successfully accomplish these measurements, an increased stability in the tunneling current must be reached and lower temperatures could be very helpful in this sense. In addition, once acquired, the STS spectra could be normalized using numerical methods, with the aim of giving an insight into the LDOS of the deposited nanostructure.

As far as Raman spectroscopy is concerned, an in-situ apparatus in the ultra-high vacuum chamber would help to avoid all the problems related to the instability of molecular chains when exposed in air. DFT simulations of Raman spectra have been demonstrated to be an effective support for the experimental data. In this field, however, a molecular model which faithfully simulates the interaction of the linear chain with the underlying gold substrate is still under investigation. At the moment researchers at the Nanolab are working on a model where the dimer interacts with a complex formed by 8 Au atoms, instead of only 4, like reported in my analyses.

Finally, in future experiments, other substrates, different from Au (111), which may form new kind of interactions with deposited molecules, could be considered. Moreover, different precursors could be employed, like the tBEBP, which is currently under investigation at the Nanolab. This molecule is the tri-functional counterpart of the molecular precursor (bBEBP) used in my experiments. Its deposition should lead to the formation of a 2D network, via the same homocoupling reaction analyzed in this thesis work. In addition, once the nanostructures formed by the deposition of the above-mentioned precursors have been fully characterized, other reaction mechanisms, which would require end groups different from Br, could be explored.

Appendix

Auger spectroscopy of carbon-based systems

In this section, preliminary experiments on the chemical characterization by means of the Auger spectroscopy are reported. I first investigated the sample of molecular chains annealed at 430 K, which was largely analyzed in the chapter 4, and then I performed some measurements also on an Au (111) surface on which I deposited the molecule 1,3,5-tris(bromoethynyl)benzene, which for simplicity will be called with the abbreviation tBEBP. The molecular model and structure formula of tBEBP are shown in figure A.1.

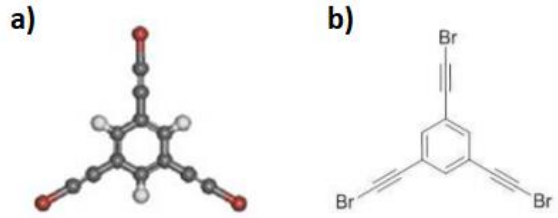

Figure A.74 The molecular model (a) and the structure formula (b) of tBEBP. [23]

This molecule was deposited on the Au (111) surface by using the same procedure employed for the deposition of bBEBP, that was explained in detail in section 3.4. Once deposited on the gold substrate, it would have formed a 2D network via the homocoupling reaction of terminal groups. My intent was that of starting a new series of analogous analyses of those performed on the sample of the deposited bBEBP molecules, using as main reference for the results the work done in ref 23. However, the single attempt of deposition resulted in a complete coverage of the Au (111) surface, as shown in figure A.2, and I was thus not able to individuate the structure of the carbon network. Hence, I proceeded with Auger spectroscopy measurements as preliminary experiments for future investigations.

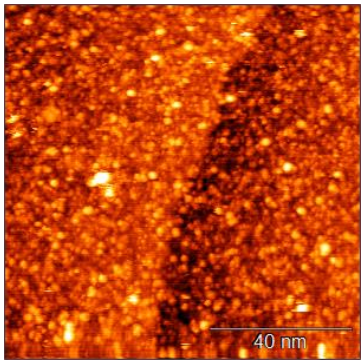

Figure A.75 (100x100 nm) STM image showing the complete coverage of the Au (111) surface by deposited tBEBP molecules. Set point (+1 V, 0.5 nA).

The idea to perform a chemical investigation on the sample of deposited chains was born in the moment that I observed for the first time the presence of large bright spots in the

large-scale STM image of the sample annealed at 430 K, which is shown in figure A.3a. It occurred as well that some of them were dragged by the STM tip, as in the case of the cut spot encircled in red in figure A.3b.

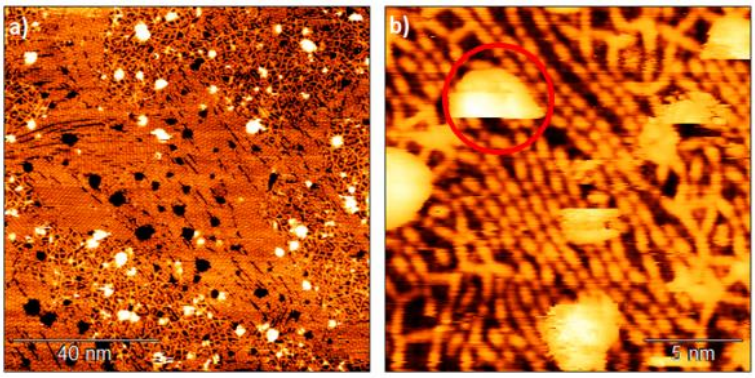

Figure A.76 STM images of the sample annealed at 430 K. (a) (100x100 nm) Large-sacle STM image where bright spots can be noted. Set point (+0.7 V, 0.6 nA). (b) (18.7x18.7 nm) Close-up STM image of an almost completely disordered domain. A cut bright spot is encircled in red. Set point (+0.8 V, 0.6 nA).

Since measurements were conducted in ultra-high vacuum, I excluded the hypothesis of a possible contamination by external gases. I thus supposed that these clusters may have formed by the agglomeration of Br atoms, which were observed to be aligned among linear chains in well-oriented domains at lower temperatures, as previously discussed in section 4.1.1. For this purpose, I carried out Auger spectroscopy measurements on the sample, with the aim of unveiling the nature of these spots. Due to the not negligible coverage of bright spots, I believed that the element by which they were formed had a certain probability to be detected by the Auger measurements.

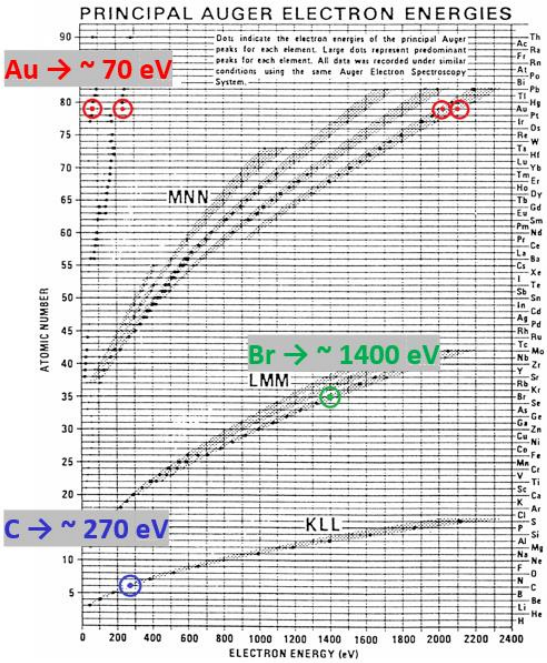

Figure A.77 Chart reporting principal Auger electron energies. Energies of gold (red circle), carbon (blue circle) and bromine (green circle) peaks are indicated.

As reference for the results I employed a table found in literature reporting the principal Auger electron energies for several elements, which is illustrated in figure A.4. According to the energy values indicated in the table I should have observed in the acquired Auger spectrum the peak of Au at ~70 eV, that of carbon at ~270 eV and, assuming that my hypothesis on Br clusters was correct, also the peak of bromine at ~1400 eV.

For the acquisition of Auger spectra, I selected the energy of the electron beam in the range $1500 - 3000\ eV$ and a beam current of $10 - 15\ \mu A$. I then set the imaging mode in a way that the first derivative of the signal, rather the direct signal would have been visualized in the acquired spectrum.

Initial measurements were conducted on a cleaned Au (111) surface, aimed to calibrate the Auger apparatus for further investigation of deposited sample. The spectrum was acquired in the range $0 - 200\ eV$ and is reported in figure A.5. The Au peak is clearly visible at energy values around 70 eV. The Auger signal at low energy values shows a non-regular behavior. I supposed this problem was related to the inaccurate calibration of the working parameters.

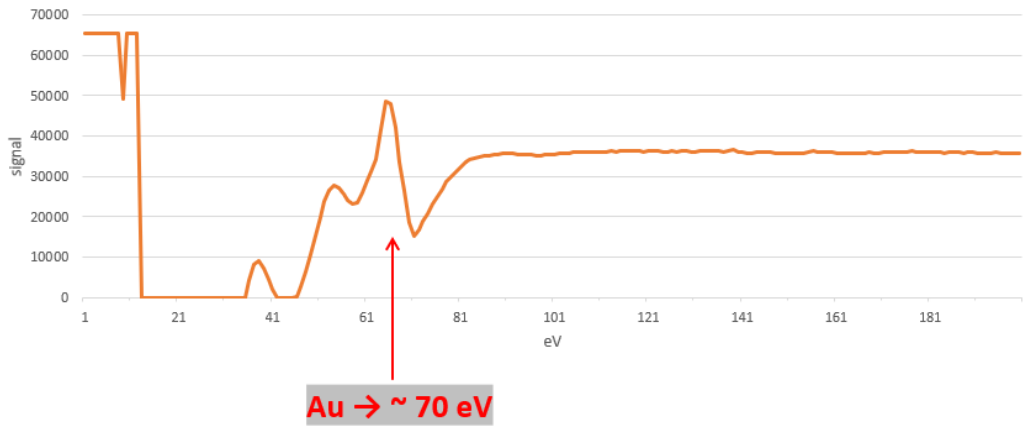

Figure A.78 Auger spectrum of the Au (111) surface. The Au peak appears at around 70 eV. Acquisition range 0-200 eV.

I then investigated the sample of deposited molecular chains annealed at 430 K. I firstly selected the range $0 - 500\ eV$ to detect the Au and C peaks. However, only the gold peak appears in the spectrum, as shown in figure A.6. Then, I selected the acquisition range $1000 - 1500\ eV$, but even the Br peak was not detected.

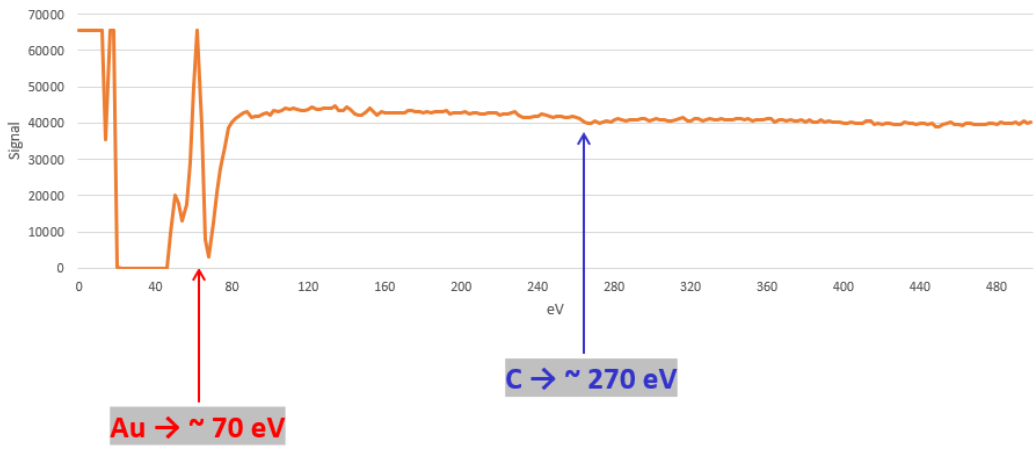

Figure A.79 Auger spectrum of the sample with deposited chains annealed at 430 K. The Au peak appears at around 70 eV. The C peak is not present. Acquisition range 0-500 eV.

Finally, Auger spectroscopy measurements were carried out on the Au (111) surface on which tBEBP molecules were deposited. The spectrum in the range $30 - 350\ eV$ (figure A.7) displays both the gold and the carbon peak, which has, however, a very low intensity. Inspections at higher energies did not reveal the presence of the Br peak.

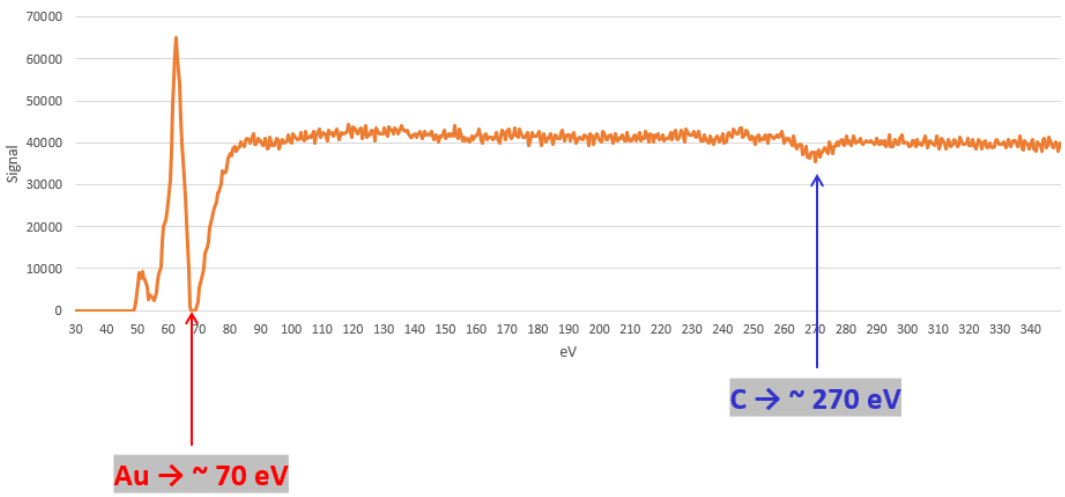

Figure A.80 Auger spectrum of the sample with deposited tBEBP molecules. The Au and C peaks appear at around 70 eV and 270 eV, respectively. Acquisition range 30-350 eV, step 0.5 eV.

The appearance of the carbon peak in the last sample could be related to the fact that in that case the amount of carbon was higher compared to the sample of deposited chains and so its presence was more easily detected by Auger investigations. The absence of the bromine peak, indeed, in my opinion, was probably due to the low amount of bromine in the sample.

In conclusion, Auger measurements did not help me to understand the nature of the bright spots observed in the figure A.3. However, these results can be useful as a reference for future chemical characterizations by Auger spectroscopy.

Bibliography

[1] C.S. Casari, M. Tommasini, R.R. Tykwinski and A. Milani. Carbon-atom wires: 1-D systems with tunable properties. Nanoscale 8, 4414 (2016).

[2] A. Hirsch. Nat. Mater., 9, 868−871 (2010).

[3] C.S. Casari and A. Milani. Carbyne: From the elusive allotrope to stable carbon atom wires. MRS Communications, 8(2), 207-219 (2018).

[4] A. Van Orden and R.J. Saykally. Small carbon clusters: spectroscopy, structure, and energetics. Chem. Rev. 98, 2313 (1998).

[5] R.O. Jones and G. Seifert. Structure and bonding in carbon clusters C14 to C24: chains, rings, bowls, plates, and cages. Phys. Rev. Lett. 79, 443 (1997).

[6] W.A. Chalifoux and R.R. Tykwinski. Synthesis of polyynes to model the sp-carbon allotrope carbyne. Nat. Chem. 2, 967 (2010).

[7] A. Milani, M. Tommasini, V. Russo, A. Li Bassi, A. Lucotti, F. Cataldo and C. S. Casari, Beilstein J. Nanotechnol., 6, 480–491 (2015).

[8] Q. Sun, L. Cai, S. Wang, R. Widmer, H. Ju, J. Zhu, L. Li, Y. He, P. Ruffieux, R. Fasel, W. Xu. Bottom-up synthesis of Metalated Carbyne. J. Am. Chem. Soc., 138, 1106−1109 (2016).

[9] L. Ravagnan, P. Piseri, M. Bruzzi, S. Miglio, G. Bongiorno, A. Baserga, C. S. Casari, A. Li Bassi, C. Lenardi, Y. Yamaguchi, T. Wakabayashi, C. E. Bottani and P. Milani. Phys. Rev. Lett., 98, 216103 (2007).

[10] L. Ravagnan, G. Bongiorno, D. Bandiera, E. Salis, P. Piseri, P. Milani, C. Lenardi, M. Coreno, M. de Simone and K. C. Prince. Carbon, 44, 1518 (2006).

[11] C. Jin, H. Lan, L. Peng, K. Suenaga and S. Iijima. Phys. Rev. Lett., 102, 205501 (2009).

[12] X. Zhao, Y. Ando, Y. Liu, M. Jinno and T. Suzuki. Phys. Rev. Lett., 90, 187401 (2003).

[13] R. H. Baughman, H. Eckhardt and M. Kertesz. J. Chem. Phys., 87, 6687 (1987).

[14] S. Yang and M. Kertesz. Linear Cn clusters: are they acetylenic or cumulenic? J. Phys. Chem. A 112, 146 (2008).

[15] A. Milani, M. Tommasini, M. Del Zoppo, C. Castiglioni and G. Zerbi. Phys. Rev. B: Condens. Matter, 74, 153418 (2006).

[16] M. Wang and S. Lin. Ballistic: thermal transport in carbyne and cumulene with micron-scale spectral acoustic phonon mean free path. Sci. Rep. 5, 18122 (2015).

[17] F. Innocenti, A. Milani and C. Castiglioni. Can Raman spectroscopy detect cumulenic structures of linear carbon chains? J. Raman Spectrosc. 41, 226 (2010).

[18] C. S. Casari, V. Russo, A. Li Bassi, C. E. Bottani, F. Cataldo, A. Lucotti, M. Tommasini, M. Del Zoppo, C. Castiglioni and G. Zerbi. Appl. Phys. Lett., 90, 013111 (2007).

[19] F. Cataldo. Tetrahedron, 60, 4265 (2004).

[20] C. S. Casari, C.S. Giannuzzi, V. Russo. Carbon, 104, 190-195 (2016).

[21] Y. P. Kudryavtsev, S. E. Evsyukov, M. B. Guseva, V. G. Babaev and V. V. Khvostov. Russ. Chem. Bull., 42, 399 (1993).

[22] P. Siemsen, R. C. Livingston and F. Diederich. Angew. Chem., Int. Ed., 39, 2633 (2000).
[23] Q. Sun, L. Cai, H. Ma, C. Yuan, and W. Xu. Dehalogenative Homocoupling of Terminal Alkynyl Bromides on Au(111): Incorporation of Acetylenic Scaffolding into Surface Nanostructures. ACS Nano, 10(7), 7023-7030 (2016).
[24] C. Shu, M. Liu, Z. Zha, J. Pan, S. Zhang, and Y. Xie et al.. On-surface synthesis of poly (p-phenylene ethynylene) molecular wires via in situ formation of carbon-carbon triple bond. Nature Communications, 9(1) (2018).
[25] L. Colazzo, F. Sedona, A. Moretto, M. Casarin, M. Sambi. Metal-Free on-Surface Photochemical Homocoupling of Terminal Alkynes J. Am, Chem, Soc., 138, 10151-10156 (2016).
[26] N. Pavliček, P. Gawel, D. Kohn, Z. Majzik, Y. Xiong, and G. Meyer et al.. Polyyne formation via skeletal rearrangement induced by atomic manipulation. Nature Chemistry, 10(8), 853-858 (2018).
[27] F. Cataldo. J. Inorg. Organomet. Polym. Mater., 16, 15 (2006).
[28] J. A. Januszewski and R. R. Tykwinski. Chem. Soc. Rev., 43, 3184 (2014).
[29] N. D. Lang and Ph. Avouris. Phys. Rev. Lett., 84, 358 (2000).
[30] S. Tongay, R. T. Senger, S. Dag and S. Ciraci. Phys. Rev. Lett., 93, 136404 (2004).
[31] V. I. Artyukhov, M. Liu and B. I. Yakobson, Nano Lett., 14(8), 4224–4229 (2014).
[32] A. Milani, M. Tommasini, V. Barbieri, A. Lucotti, V. Russo, F. Cataldo and C.S. Casari. Semiconductor-to-metal transition in carbon-atom wires driven by sp2 conjugated end groups. J. Phys. Chem. C 121, 10562 (2017).
[33] R. Rivelino, R.B. dos Santos, F. de Brito Mot, and G.K. Gueorguiev. Conformational effects on structure, electron states, and Raman scattering properties of linear carbon chains terminated by graphene-like pieces. J. Phys. Chem. C 114, 16367 (2010).
[34] A. La Torre, A. Botello-Mendez, W. Baaziz, J.-C. Charlier and F. Banhart. Nat. Commun., 6, 6636 (2015).
[35] M.M. Haley. Synthesis and properties of annulenic subunits of graphyne and graphdiyne nanoarchitectures. Pure Appl. Chem. 80, 519 (2008).
[36] F. Diederich and M. Kivala. Adv. Mater., 22, 803– 812 (2010).
[37] A. Lucotti et al. Chem. Phys. Lett., 417, 78 (2006).
[38] C. Ataca and S. Ciraci. Perpendicular growth of carbon chains on graphene from first-principles. Phys. Rev. B 83, 235417 (2011).
[39] G. Binnig, H. Rohrer, C. Gerber and E. Weibel. Surface Studies by Scanning Tunneling Microscopy. Physical Review Letters, 49(1), 57-61 (1982).
[40] T. Matsui. Construction of an ultra-low temperature STM with a bottom loading mechanism. Physical B: Condensed Matter, 329-333, 1653-1655 (2003).
[41] J. Bardeen. Phys. Rev. Lett. 6, 57 (1961).
[42] J. Tersoff and D.R. Hamann. Phys. Rev. Lett. 50, 1998 (1983).
[43] C. J. Chen. Phys. Rev. Lett. 65, 448 (1990).
[44] A. Li bassi et al.. Appl. Phys. Lett. 91, 173120 (2007).

[45] J. A. Stroscio, R. M. Feenstra, and A. P. Fein. Phys. Rev. Lett. 58, 1668 (1987).
[46] V. A. Ukraintsev. Phys. Rev. B 53, 11176 (1996).
[47] B. Koslowski, C. Dietrich, A. Tschetschetkin and P. Ziemann. Phys. Rev. B 75, 035421 (2007).
[48] M. Passoni, F. Donati, A. Li Bassi, C. S. Casari, and C. E. Bottani. Phys. Rev. B 79 045404 (2009).
[49] O. Endo, M. Nakamura, K. Amemiya, H. Ozak. Compression-Induced Conformation and Orientation Changes in an n-Alkane Monolayer on a Au (111) Surface. Langmuir, 33, 3934-3940 (2017).
[50] D. A. Kislitsyn, B.N. Taber, C. F. Gervasi, S. C.B. Mannsfeld, L. Zhang, A. L. Briseno, G.V. Nazin. Coverage-Dependent Self-Assembly Regimes of Alkyl-Substituted Thiophene Oligomers on Au (111): Scanning Tunneling Microscopy and Spectroscopy. J. Phys. Chem. C, 119, 26959-269676 (2015).
[51] Q. Sun, B. Tran, L. Cai, H. Ma, X. Yu and C. Yuan et al. On-Surface Formation of Cumulene by Dehalogenative Homocoupling of Alkenyl gem-Dibromides. Angewandte Chemie, 129(40), 12333-12337 (2017).
[52] J.V. Barth, H. Brune, G. Ertl, and R.J. Behm. Scanning tunneling microscopy observations on the reconstructed Au (111) surface: Atomic structure, long-range superstructure, rotational domains, and surface defects. Physical Review B, 42(15):9307 (1990).
[53] Ch. Wöll, S. Chiang, R. J. Wilson, and P. H. Lippel. Determination of atom positions at stackingfault dislocations on Au (111) by scanning tunneling microscopy. Physical Review B, 39:7988–7991 (1989).
[54] Noboru Takeuchi, C.T. Chan and K.M. Ho. Au (111): A theoretical study of the surface reconstruction and the surface electronic structure. Physical Review B, 43(17):13899 (1991).
[55] F. Donati, G. Fratesi, L. Ning, A. Brambilla, M.I. Trioni, A. Li Bassi, C.S. Casari and M. Passoni. Electronic and magnetic properties of bulk Cr tips for scanning tunneling spectroscopy. Physical Review B, 87(23):235431 (2013).
[56] F. Donati, S. Piccoli, C.E. Bottani and M. Passoni. Three-dimensional approach to scanning tunneling spectroscopy and application to Shockley states. New Journal of Physics, 13(5):053058 (2011).
[57] P. Kowalczyk, W. Kozlowski, W. Olejniczak and P. Datta. STS investigations of temperature dependence of Au (111) surface state energy position. Surface Science, 600(8), 1604-1607 (2006).